

ULRR

Mathematical modelling of nanofluid-based direct absorption solar collectors

Item Type	Thesis
Authors	O'Keeffe, Gary J.
Download date	2026-04-15 12:51:34
Item License	https://creativecommons.org/licenses/by-nc-sa/1.0/
Link to Item	https://hdl.handle.net/10344/7058

Mathematical modelling of nanofluid-based direct absorption solar collectors



Gary O’Keeffe

Department of Mathematics and Statistics

University of Limerick

A thesis submitted for the degree of

Doctor of Philosophy (PhD)

Supervised by: Dr. Sarah L. Mitchell and Prof. Tim G. Myers

Submitted to the University of Limerick, May 2018

Abstract

Solar-thermal collectors capture solar energy and convert it into heat energy. Several types of solar-thermal collectors have been used to harness solar radiation in both residential, electricity generation, and industrial settings; one class of solar-thermal collector design is the direct-absorption solar collector (DASC). An ongoing technological challenge in this area of science is to develop a truly widespread, cost-effective system which efficiently converts solar energy and can compete with fossil fuel power generation. Nanofluids are a relatively new class of fluid that offer great promise as an alternative to conventional fluids in a DASC due to their unique optical properties.

This thesis develops and analyses novel mathematical models to describe and better understand the complicated interactions between solar radiation absorption, fluid flow and heat transfer within nanofluid-based DASCs (NDASCs) in a multiphysics continuum mechanics approach involving the use of coupled partial differential equations. Overall, we discuss and model six different NDASCs: Collector 1 is an NDASC consisting of a nanofluid flowing through parallel-plates on an inclined plane, Collector 2 is similar to Collector 1, but with a reflective base-panel, Collector 3 is an NDASC consisting of a nanofluid flowing through cylindrical pipes on an inclined plane, Collector 4 is a nanofluid-based direct absorbing parabolic trough solar collector (NDAPSC) under laminar flow, Collector 5 is an NDAPSC under turbulent flow, and Collector 6 is an NDAPSC under turbulent flow with a time-dependent source term.



Declaration

I hereby declare that this thesis is my own work and that it has not been submitted for any other academic award.

The work in this thesis was conducted from October 2014 to May 2018 under the supervision of Dr. Sarah L. Mitchell and Prof. Tim G. Myers in the department of Mathematics and Statistics in the University of Limerick.

Gary J. O'Keeffe

Limerick, 2018

To my parents and grandparents.

Acknowledgements

There are many people whose help I wish to acknowledge here some of whom I will mention by name:

- My family for their constant and unwavering support.
- My supervisors Dr. Sarah Mitchell and Prof. Tim Myers for their help and advice throughout my PhD.
- Everyone from UL's Department of Maths and Stats throughout my time here, especially: Vinnie, James, Peg, Giannis, Sinéad, Adam, Seamus, Dave, and the gentlemen from A2016i.
- My friends, team-mates, teachers, and class-mates from: Lisnagry N.S., Castletroy College, the University of Limerick, Slippery Rock University, and further afield.
- Financial support from the Irish Research Council (Grant Number: GOIPG/2014/887), and the Mathematics for industry network (Grant number: ECOST/STSM/TD1409/290216/071429).

Publications

- O’Keeffe, G. J., Mitchell, S. L., Myers, T. G., and Cregan, V. The effect of depth dependent velocity on the performance of a nanofluid-based direct absorption solar collector. *Progress in Industrial Mathematics at ECMI 2016*. [Awaiting publication].
- O’Keeffe, G. J., Mitchell, S. L., Myers, T. G., and Cregan, V. Modelling the efficiency of a nanofluid-based direct absorption parabolic trough solar collector. *Solar Energy*. 159, 44-54. 2018.
- O’Keeffe, G. J., Mitchell, S. L., Myers, T. G., and Cregan, V. Modelling the efficiency of a low-profile nanofluid-based direct absorption parabolic trough solar collector. [In review]
- O’Keeffe, G. J., Mitchell, S. L., Myers, T. G., and Cregan, V. Time-dependent modelling of nanofluid-based direct absorption parabolic trough solar collectors. [In review]
- O’Keeffe, G. J., Mitchell, S. L., Myers, T. G., and Cregan, V. (2019). Nanofluid-based direct absorption solar collectors. In *Nanofluids and their engineering applications*. CRC Press/Taylor and Francis Group, USA. [Invited contribution, currently at the pre-draft stage]

Talks and conferences

- O’Keeffe, G. J., Mitchell, S. L., Myers, T. G., and Cregan, V. Modelling the efficiency of Nanofluid based Solar Collectors. 2nd Annual NUI Galway SIAM student chapter conference, National University of Ireland Galway, December 2015.
- O’Keeffe, G. J., Mitchell, S. L., Myers, T. G., and Cregan, V. Modelling the efficiency of Nanofluid based Solar Collectors. Centre de Recerca Matemàtica, Barcelona, Spain, March 2016.
- O’Keeffe, G. J., Mitchell, S. L., Myers, T. G., and Cregan, V. Modelling the efficiency of Nanofluid based Solar Collectors. British Applied Mathematics Colloquium. Oxford, UK, April 2016.

-
- O’Keeffe, G. J., Mitchell, S. L., Myers, T. G., and Cregan, V. Modelling the efficiency of Nanofluid based Solar Collectors. 19th European Conference on Maths for Industry, Santiago de Compostela, Spain, June 2016.
 - O’Keeffe, G.J. The Mathematics behind Solar Collectors. MACSI 10, University of Limerick, December 2016.
 - O’Keeffe, G. J., Mitchell, S. L., Myers, T. G., and Cregan, V. Modelling nanofluid-based solar collectors. SIAM AN17, Pittsburgh, PA, USA, July 2017.
 - O’Keeffe, G. J., Mitchell, S. L., Myers, T. G., and Cregan, V. Modelling the efficiency of Nanofluid based Solar Collectors. 4th Annual Irish SIAM student chapter conference, National University of Ireland Galway, December 2017.

CONTENTS

1	Introduction	1
1.1	The global energy landscape	1
1.2	Solar-thermal collectors	4
1.3	Thesis objectives	11
2	Collector 1: A parallel-plate NDASC	13
2.1	Introduction	13
2.2	Model	16
2.2.1	Introduction	16
2.2.2	Conservation of energy	17
2.2.3	Nanofluid properties	17
2.2.4	Conservation of momentum	20
2.2.5	Heat source	21
2.2.6	Dimensional analysis	27
2.2.7	Case study	29
2.2.8	Solution method	30
2.2.9	Efficiency	32
2.2.10	Results	34
2.3	Summary and discussion	38
3	Collector 2: A Parallel-plate NDASC with reflective base panel	41
3.1	Introduction	41
3.2	Model	43

3.2.1	Introduction	43
3.2.2	Conservation of Energy	44
3.2.3	Conservation of momentum	44
3.2.4	Heat source	44
3.2.5	Dimensional analysis	47
3.2.6	Case study	48
3.2.7	Solution method	49
3.2.8	Results	50
3.3	Summary and discussion	56
4	Collector 3: A Non-concentrating cylindrical NDASC	59
4.1	Introduction	59
4.2	Model	61
4.2.1	Introduction	61
4.2.2	Conservation of energy	62
4.2.3	Conservation of momentum	62
4.2.4	Heat source	63
4.2.5	Dimensional analysis	64
4.2.6	Case study	66
4.2.7	Solution method	67
4.2.8	Results	69
4.3	Summary and discussion	71
5	Collector 4: A low-profile parabolic trough NDASC	75
5.1	Introduction	75
5.2	Design considerations	77
5.2.1	Heat-mirrors	77
5.2.2	Collector design	80
5.3	Model	81
5.3.1	Introduction	81
5.3.2	Conservation of energy	82
5.3.3	Conservation of momentum	82
5.3.4	Heat source term	83
5.3.5	Case Study	91
5.3.6	Solution method	92
5.3.7	Results	93

5.4	Summary and discussion	100
6	Collector 5: A large concentrating NDAPSC	103
6.1	Introduction	103
6.2	Model	106
6.2.1	Introduction	106
6.2.2	Conservation of energy	106
6.2.3	Heat source	107
6.2.4	Solution method	107
6.2.5	Dimensional analysis	108
6.2.6	Case study	109
6.2.7	Solution method	110
6.2.8	Efficiency	111
6.2.9	Results	112
6.3	Summary and discussion	118
7	Collector 6: Time-dependence in a large concentrating NDAPSC	121
7.1	Introduction	121
7.2	Model	123
7.2.1	Introduction	123
7.2.2	Conservation of energy	123
7.2.3	Heat source terms	125
7.2.4	Dimensional analysis	126
7.2.5	Case study	127
7.2.6	Solution method	127
7.2.7	Efficiency	129
7.2.8	Results	130
7.3	Summary and discussion	137
8	Further discussion	139
8.1	Summary of work	139
8.2	Objective review	147
Appendices		151
A	Alternative expression of hyper-geometric function	153

CONTENTS

B	Ideal heat-mirrors	157
C	Improved numerical scheme for modelling Collector 4	165
D	Alternative analytic expression for time-dependent temperature in Scenario 2	171
	Bibliography	173

CHAPTER 1

INTRODUCTION

This chapter outlines our motivation for pursuing the research in this thesis. Section 1.1 discusses the overall global energy landscape on a fuel-by-fuel basis. We examine renewable energy trends in close detail and identify a clear demand for better solar-thermal energy production solutions. Therefore, we discuss solar-thermal energy further in Section 1.2 before establishing and justifying, explicit and assessable research objectives for this thesis in Section 1.3.

1.1 The global energy landscape

Energy consumption is a significant driver of economic growth, especially in rapidly developing economies such as India and China [65]. Technological improvements, political pressure, and global gross domestic product (GDP) growth are all affecting the amount of global energy consumption [45]. While long-term energy trends are notoriously difficult to predict [11], in this section, we explore current trends in the global energy landscape in light of: recent breakthroughs in hydraulic fracturing, China moving away from coal, and the renewable energy boom [5, 65]. The United States Energy Information Administration's (EIA's) International Energy Outlook 2017 [65] offers a comprehensive forecast on the global energy landscape in the context of: oil, coal, natural gas, nuclear, and renewables. Figure 1.1 illustrates the estimated trajectories of the consumption

of these energy sources as predicted by the EIAs International Energy Outlook 2017 [65].

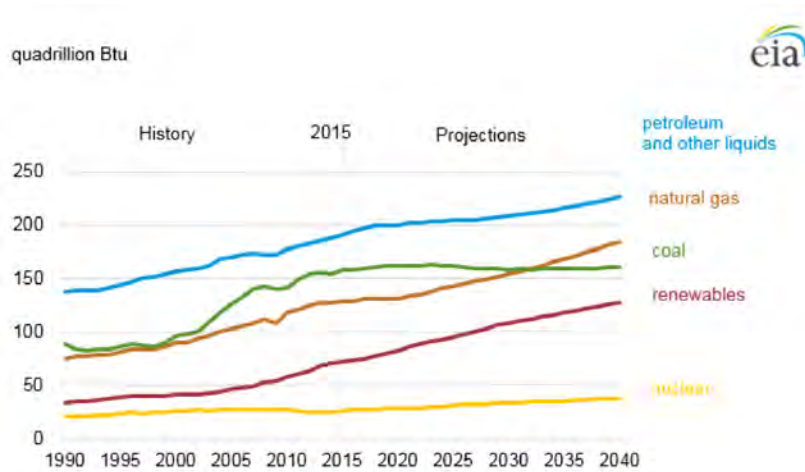


Figure 1.1: World energy consumption by energy source [Source: Figure 2 from EIA International Energy Outlook 2017 [65]].

Currently, oil-based fuels are the world’s leading source of energy [5, 65]. Global oil consumption is rising each year and is anticipated to continue growing over the coming decades. Most of this growth is in the transportation and industrial sectors [65]. The global fleet of cars is expected to double in the next twenty years with increasing car ownership rates in emerging markets driving this growth [5]. However, oil production is expected to decline further into the future due to reduced demand stemming from: emission reduction policies, cost reductions in renewable energy generation, and other alternative technologies [27].

Global coal consumption is broadly plateauing, however, coal is still the world’s second most consumed energy source [11, 65]. The top three coal-consuming countries are China, the United States, and India (which together account for more than 70% of world’s coal use). China currently accounts for almost half of the world’s total coal consumption; however, China is moving away from coal towards cleaner (lower-carbon) fuels as its economy shifts towards a more sustainable pattern of growth [65]. China’s coal consumption is projected to broadly plateau over the next decade before decreasing into 2040. Coal consumption in the United States has already plateaued, and is expected to remain constant over the coming decades [65]. Meanwhile, India has the world’s fastest-growing economy, and this growth should increase India’s demand for coal. India’s economy is expected to

grow at a rate of 5.5% per year from 2012 to 2040 [65], and this demand should see India overtake the United States as the world's second biggest consumer of coal by around 2030 [65].

Since the United States' Shale Boom (circa 2008) natural gas has experienced phenomenal growth and going forward, natural gas production is predicted to grow at an even faster rate due to advancements in liquefied natural gas (LNG) [5, 65]. For example, in Europe natural gas production is slowing down but consumption is still expected to rise over the next decade because Europe's increasing natural gas demands will be met by LNG imports from the United States [5].

On the global scale, we should still see some growth in the nuclear sector driven by rapid expansion in China as they move away from coal [65]. However, ageing nuclear plants are being decommissioned in Europe and will continue to do so going forward with little reinvestment in new plants. For example, in the United Kingdom there are currently eight nuclear power stations in operation, of which, only four will remain in operation in 2027.

Over the next twenty years renewable energy is projected to be the fastest-growing fuel source (7.6% p.a.), more than quadrupling. This anticipated growth will be driven by solar and wind (both of which are becoming increasingly competitive). British Petroleum's [5] analysis, suggests that onshore wind power will remain cheaper than solar energy in both the United States' and China's power sectors, also, gas and coal are expected to provide the primary source of competition to renewable energies in the United States and China respectively. The solar energy industry has experienced phenomenal growth in recent years due to both technological improvements resulting in cost reductions and government policies supportive of renewable energy development and utilisation [61]. Global solar energy production is predicted to rise at a rate of 8.9% annually between 2012 to 2040, making it the fastest growing form of energy generation in the coming decades [65]. Currently, solar-thermal technologies produce more energy than solar voltaic technologies [38]. Solar thermal technologies provide hot water to heat and cool space, and to generate high-temperature heat for industrial processes [52]. The research in this thesis is motivated by recent theoretical advances in solar thermal energy production. While the global capacity of solar thermal technology continues to rise, recently the rate of capacity increase has seen a decline, falling 14% in 2015 [52]. More innovation is needed if solar thermal technologies are to see this recent trend reversed.

1.2 Solar-thermal collectors

The potential benefit of solar energy is demonstrated by the fact that more solar energy strikes the Earth in one hour than the total energy consumption by humans in one year [44]. The ongoing technological challenge is to develop a truly widespread, cost-effective system which efficiently converts solar energy and can compete with fossil fuel power generation. Several types of solar-thermal collectors have been used to harness solar energy in both residential, electricity generation, and industrial settings. Taylor et al. [59] outline the three ideal characteristics of a solar thermal collector. (1) An ideal collector should efficiently absorb solar radiation. (2) An ideal collector must minimise heat loss due to convection and radiation. (3) An ideal collector should have minimal pumping and maintenance costs. In the following paragraphs we discuss the most common types of solar-thermal collectors.

We classify solar collectors based on whether or not the incoming radiation is concentrated. In the non-concentrating type of solar collector, the aperture area is the same as the area of the surface that is absorbing the radiation—this type of solar collector is typically used in a residential setting to heat water or buildings. The most common residential solar collectors are flat-plate black-surface absorbers and evacuated tubes [26].

Flat-plate collectors consist of a dark flat-plate absorber, and a working-fluid which circulates through the system while extracting heat from the absorber plates. Figure 1.2 depicts the cross-section of this particular solar collector design; in this figure the collector is surrounded on the upper side by a transparent cover, allowing light to hit the absorber creating a greenhouse effect, and on the underside by insulation to prevent heat loss. Flat plate collectors can be cheap relative to other collectors due to the simplicity of their design—they can also be integrated into roofs or façades; however, they don't perform well in wet/cold environments [34]. Average annual flat plate collector efficiency in Dublin, Ireland, was found to be 46.1% [3].

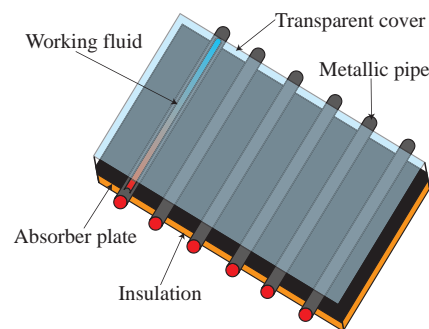


Figure 1.2: Flat plate solar collector design.

Evacuated tube collectors come in various design layouts; one of the most common forms is composed of multiple evacuated glass tubes, each containing an absorber plate fused to a heat pipe [39]. The working-fluid extracts heat from the top of these heat pipes as it flows through a manifold. Insulation covers this manifold, and a vacuum surrounds the glass tubes, reducing the convective and conductive heat losses—this process is illustrated more clearly in Figure 1.3.

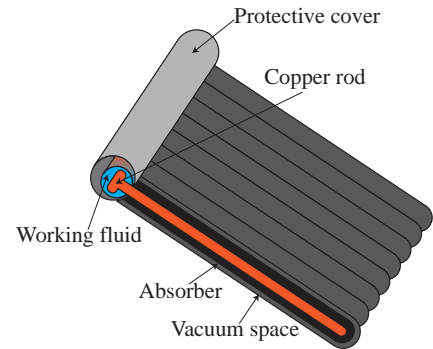


Figure 1.3: Evacuated tube solar collector design.

Vacuum space surrounding the absorber eliminates Newton cooling as a mechanism for heat loss and this affect makes evacuated tube collectors ideal for solar-thermal conversion in cold, windy and humid conditions. Average annual vacuum tube collector efficiency in Dublin, Ireland, was found to be 60.7% [3], which is significantly higher than the flat-plate collector efficiency. In fact, vacuum tube collectors can perform up to 30% better than flat plate collectors; however, they are more expensive to manufacture [9].

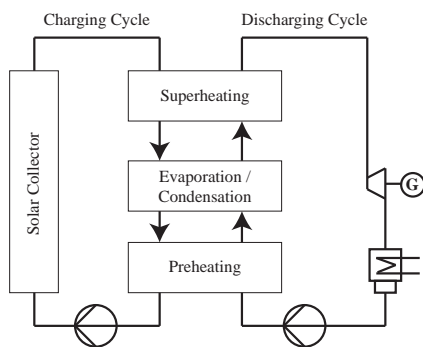


Figure 1.4: A simplified solar collector power plant with direct steam generation [55].

Concentrating collectors have a larger aperture area than absorber area—they can be used in many industrial processes including; sterilising, pasteurising, drying, hydrolysing, distillation, cleaning, and polymerisation [25]. A more exhaustive list of industrial processes and their associated operating temperatures is outlined in Table 1.1—which is from Kalogirou [25]. In an industrial heat process, the operating temperature needs to be consistent and predictable; therefore, models for accurately predicting the temperature at the outlet of a collector are of vital importance to the viability of this solar-thermal application. Concentrating solar collectors are also used to power turbines and generate electricity. The Rankine cycle, shown in Figure 1.4, describes the process by which steam operated heat engines commonly found in power towers/parabolic trough thermal power generation plants

[20, 32, 55, 56, 67]. In some solar collector driven Rankine cycles the solar collector and the Rankine cycle operate in the same closed loop and so they share the same working-fluid [67], but Figure 1.4 depicts a solar Rankine cycle, consisting of two closed loops. In the first loop, (the charging cycle) a working-fluid is pumped through the solar collector before it enters a heat exchanger. The heat exchanger consists of three stages: superheating, evaporation/condensation, and preheating. The working-fluid in the charging cycle is hottest after exiting the solar collector and before entering the superheating stage; it then becomes progressively cooler as it transfers its thermal energy into the working-fluid/gas in the second loop (the discharging cycle). In the discharging cycle, gas is condensed into a liquid phase after exiting the steam turbine and this liquid is then pumped into a heat exchanger, where it heats up past the point of evaporation and its phase changes back to gas. This gas then flows back into the steam turbine where it is used to generate electricity. We note that in some solar Rankine cycles, the working-fluid in the charging cycle does not have enough thermal energy to sufficiently heat the liquid/gas in the discharging cycle, and so an additional source of heat can be applied, i.e., natural gas; however, this process is not illustrated in Figure 1.4.

Industry	Process	Temperature (K)
Dairy	Pressurisation	333.15-353.15
	Sterilisation	373.15-393.15
	Drying	393.15-453.15
	Concentrates	333.15-353.15
	Boiler feed water	333.15-363.15
Tinned food	Sterilisation	383.15-393.15
	Pasteurisation	333.15-353.15
	Cooking	333.15-363.15
	Bleaching	333.15-363.15
Textile	Bleaching or dyeing	333.15-363.15
	Drying or degreasing	373.15-403.15
	Dyeing	343.15-363.15
	Fixing	433.15-453.15
	Pressing	353.15-373.15
Paper	Cooking or drying	333.15-353.15
	Boiler feed water	333.15-363.15
	Bleaching	403.15-423.15
Chemical	Soaps	473.15-533.15
	Synthetic rubber	423.15-473.15
	Processing heat	393.15-453.15
	Pre-heating water	333.15-363.15
Meat	Washing or sterilisation	333.15-363.15
	Cooking	363.15-373.15
Beverages	Washing or sterilisation	333.15-353.15
	Pasteurisation	333.15-343.15
Flours and by-products	Sterilization	333.15-353.15
Timber by-products	Thermodiffusion beams	353.15-373.15
	Drying	333.15-373.15
	Pre-heating water	333.15-363.15
	Preparation pulp	393.15-443.15
Bricks and blocks	Curing	333.15-413.15
Plastics	Preparation	393.15-413.15
	Distillation	413.15-423.15
	Separation	473.15-493.15
	Extension	413.15-433.15
	Drying	453.15-473.15
	Blending	393.15-413.15

Table 1.1: Temperatures needed in various industrial processes [25].

The first type of concentrating solar thermal system we discuss is the power tower. Figure 1.5 shows a typical power tower layout; this design consists of a large tower which is surrounded by sun-tracking mirrors called ‘heliostats’. The heliostats concentrate incoming solar radiation onto the receiver at the top of the power tower. A working-fluid then flows through the receiver, collecting heat and transporting it to a power station below where the thermal energy is converted into electricity [21].

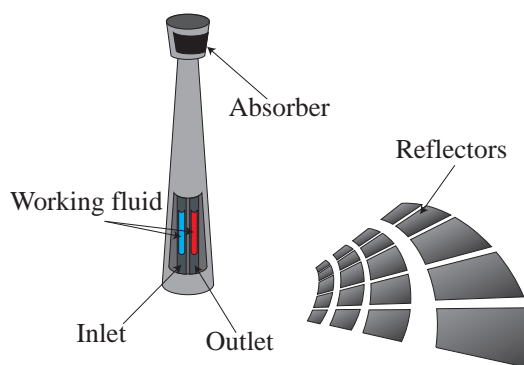


Figure 1.5: Solar tower solar collector design.

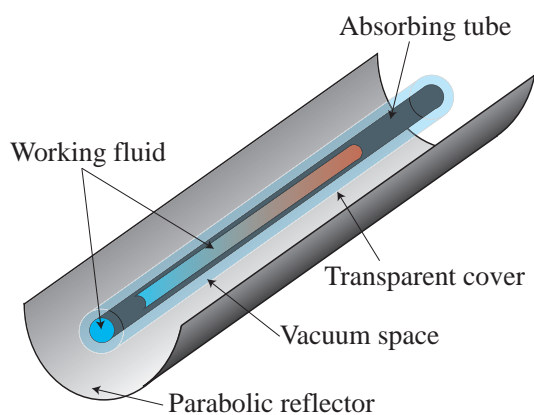


Figure 1.6: Parabolic trough solar collector design.

A parabolic trough solar collector, as shown in Figure 1.6, can be used to generate electricity or heat for an industrial process. In this design, a parabolic mirror reflects incoming sunlight onto a receiver located on its focal line. A working-fluid flows through the receiver and as the receiver heats up, so does the working-fluid. The parabolic mirror tracks the sun, similarly to the heliostats in the power tower.

A solar dish system, pictured in Figure 1.7, includes a parabolic dish reflector that concentrates incoming sunlight onto a receiver located at the parabolic dish’s focal point. This dish tracks the Sun as it moves across the sky. The working-fluid in the receiver is heated up to 250-700 °C and this heat energy is used by a Stirling engine to generate power [40]. The heat engine is directly attached to the receiver in this collector, and so there is a different thermal-electric energy conversion process than is in the Rankine cycle heat engine. A Stirling engine is a closed-cycle regenerative heat engine that operates by cyclic compression and expansion of the working-fluid at different temperatures. Solar-dish systems can provide between 31% and 32% solar-to-electric ef

efficiency [6].

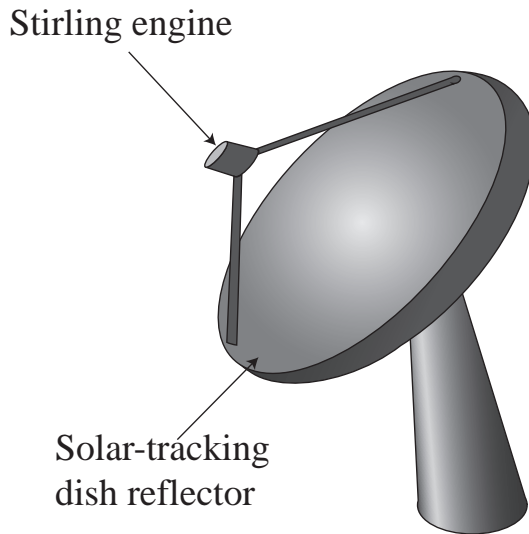


Figure 1.7: Solar dish solar collector design.

thus pushing the power piston to the farthest limit of the power stroke. In position (c), the displacer piston displaces the working-gas so that most of it is now adjacent to the heat sink. In position (d), the working-gas is compressed as it cools down and is also compressed by the flywheel momentum; and thus the cycle begins again.

All of the concentrating and non-concentrating solar collectors mentioned above are ‘surface-based’ collectors; that is, in each of these designs, the receiver’s surface absorbs the incoming sunlight. For example, parabolic trough collectors incorporate an opaque metal surface coated with a selective thin film to efficiently convert solar radiation into thermal energy [38]. Then, a working-fluid flows through the receiver and absorbs thermal energy from this heated surface. Heat loss occurs via convection and radiation at the surface of the absorber. Unsurprisingly, the surface is the hottest part of a ‘surface-based’

Figure 1.8 illustrates the operation of a Stirling engine. This design consists of a power piston, a displacer piston, a heat source (in this case concentrated solar energy), a heat sink (perhaps cooling fins), and a working-gas. In position (a), the power piston compresses the working-gas, moving it away from the heat sink; meanwhile, the displacer piston displaces the working-gas so that most of it is now adjacent to the heat source. In position (b), gas expands as it is heated, and this increases the pressure in the system,

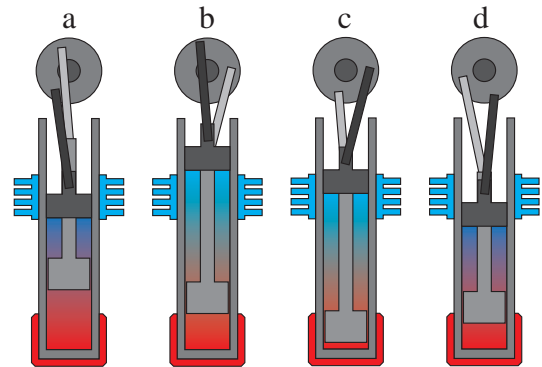


Figure 1.8: Stirling engine mechanism.

absorber. Surface-based absorption is not the only way to capture and convert electromagnetic radiation into usable thermal energy. Direct absorption solar collectors (DASCs) offer a different solution [59]; DASCs were first proposed in the mid-1970s as an alternative to surface absorbers. A DASC does not contain an absorbing surface; instead, the working-fluid absorbs incoming solar energy directly. This leads to lower temperatures at the surface of the receiver, and potentially less energy lost to the surrounding environment. Standard fluids are inefficient at absorbing sunlight due to their low absorptive properties; for example, Otanicar et al. [47] show that water only absorbs 13% of the available solar energy in a DASC of depth 1 cm. Therefore, DASCs initially failed to take off as they were not a commercially viable solar collector design [49]. In the past, people have added particles/dyes to liquids in an attempt to enhance the thermophysical and/or optical properties of the working-fluid in a DASC [13]. Large particles can settle and clog systems, and this escalates the cost of maintenance [13]; however, nanoparticle-laden fluids can serve as the absorbing medium in DASCs to overcome the poor absorption properties of conventional fluids [59].

Unlike traditional DASCs, nanofluid-based direct absorption solar collectors (NDASCs) use nanofluids to absorb and scatter incident sunlight. A nanofluid is a colloidal suspension of nanoparticles in a liquid medium. Nanoparticles do not settle as quickly as larger particles; however, incorrect nanofluid preparation can lead to nanoparticle agglomeration, and pockets of slow-moving or stationary flow in the system can lead to nanoparticle sedimentation [8]. Also, high particle volume fractions in a nanofluid can change the viscosity and overall fluid dynamics in the system, potentially increasing the pump's workload, and so usually nanofluids appear in NDASCs at very low particle volume fractions ($< 0.01\%$). Nanofluids with low nanoparticle volume fractions have similar thermophysical properties to their base fluid; however, they exhibit enhanced optical properties. Figure

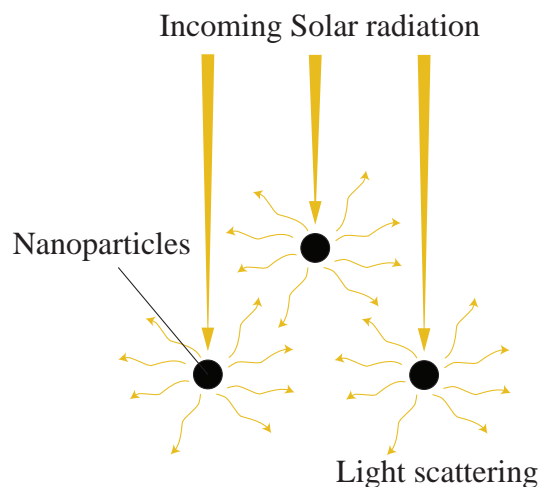


Figure 1.9: Incoming radiation absorbed and scattered by nanoparticles.

1.9 depicts the incoming radiation being absorbed and scattered by nanoparticles suspended in a liquid medium; solar radiation is attenuated much faster due to the nanoparticles absorbing and scattering radiation propagating through the nanofluid. These optical enhancements show a potential for volumetric absorption to be a more efficient solar collector design than surface-based absorption [37, 48]; therefore, NDASCs are the focus of this thesis.

1.3 Thesis objectives

The aim of this thesis is to make a scientific contribution towards the modelling of NDASCs. Before starting this project, we define the following research objectives:

1. Complete a literature review of nanofluids and NDASCs,
2. Identify opportunities for future research in this field,
3. Formulate useful mathematical models for NDASCs.

Objective 1 aims to understand previous scientific contributions, Objective 2 looks towards future research opportunities, and Objective 3 focuses on making significant novel scientific contributions. Since the study of NDASCs is such a promising field, there are many people working in this area and the literature is constantly evolving. In order to make a meaningful scientific contribution towards modelling NDASCs, we must know and understand the scope of its surrounding literature, i.e., we must fulfil Objective 1. Looking towards the future, Objective 2 provides additional context for our research; together with Objective 1, Objective 2 will inform our decision-making process. We will continuously ask ourselves ‘will this work be useful for future scientists?’ while deciding on which avenues of research to pursue. Meanwhile, we will fulfil Objective 3 through successful pursuit of the opportunities identified in Objective 2. In Section 8.2 we critically reflect on the scope this thesis through the lens of these three objectives.

CHAPTER 2

COLLECTOR 1: A PARALLEL-PLATE NDASC

2.1 Introduction

In this chapter we model a nanofluid-based direct absorption solar collector consisting of nanofluid flow between parallel plates on an inclined plane. Since this is the first collector we discuss, it will be referred to as ‘Collector 1’. We choose to model this type of collector first as it is a well-studied and somewhat simple problem. While the model proposed in this chapter has some novel elements, it is by no means ground-breaking, that notwithstanding, this is perhaps the most important chapter in the thesis. In the following chapters, we will build upon the fundamental concepts introduced in this chapter as we model ever more complex systems.

Figure 2.1 illustrates the general layout of Collector 1. In this design, nanofluid flow is laminar and is driven by gravity where the parallel plates are modelled on an inclined plane. Incoming solar radiation passes through the upper glass panel and decays as it propagates through the collector and is absorbed and scattered by the nanofluid. The nanofluid heats up as it absorbs incoming radiation, also, the base panel of the collector is insulated and non-reflective. The industrial process heat market is under-served with viable solar-thermal options [38]. A suitable solar collector needs to be efficient, cheap, and easily integrated into

architectural designs [50]. Li et al. [38] define a low-profile collector as a collector that is less than 15 cm in height; such collectors can be placed on rooftops and are easier to integrate into building designs as they can avoid potential wind loading issues [38]. Collector 1 meets this criteria and so it is considered a low-profile design.

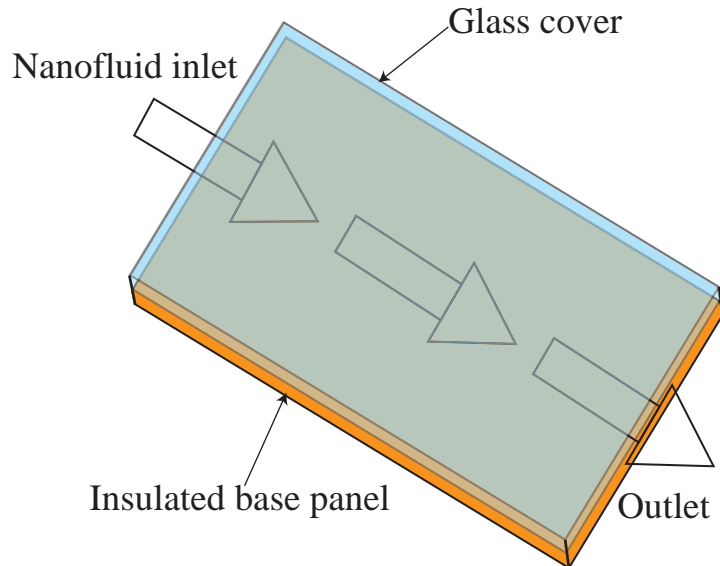


Figure 2.1: General design of Collector 1.

Recent research has modelled NDASCs analytically in order to get a better qualitative understanding of solar collector performance [10, 36, 66]. Tyagi et al. [63] present the first theoretical model of an NDASC. Their model consists of a system of two differential equations; a radiative transport equation (RTE), describing the propagation of solar radiation through the nanofluid, and a conservation of energy equation. The model neglects thermal re-emission effects by assuming low operating temperatures. They simulate the model numerically and demonstrate up to a 10% efficiency enhancement over conventional flat-plate collectors by using water-based Al nanofluids. The collector efficiency increased rapidly with volume fraction and reached a maximum value of $\sim 80\%$ at a volume fraction of $\sim 2\%$. Gorji and Ranjbar [19] offer an extensive review of the literature surrounding the use of nanofluids in DASCs. Table 4 from Gorji and Ranjbar [19] presents a chronological summary of the literature around on low-flux NDASCs, includes 18 previous studies. Since the aim of this chapter is to develop an analytic expression for the temperature (and efficiency) of an NDASC, we focus this

discussion on the analytic studies presented by Gorji and Ranjbar. Of the articles mentioned in that paper, only three provide a fully analytical solution for the temperature of the nanofluid as it flows through the receiver: Cregan and Myers [10], Lee and Jang [36], and Turkyilmazoglu [62]. Cregan and Myers present the first fully analytic solution for the temperature of a low-flux NDASC; in their proposed model, they assume a laminar and plug flow through the receiver and apply a zero-flux boundary condition at the bottom of the receiver. Lee and Jang [36] investigate the efficiency of an NDASC, treating flow in the receiver as steady, laminar, and depth-dependent. They obtain an analytic solution for the temperature in the system after applying a zero-flux boundary condition at the bottom of the receiver. This study shows that previous methods overestimate efficiency by modelling the collector subject to plug-flow. Meanwhile, Turkyilmazoglu applies an isothermal boundary condition rather than a zero-flux boundary condition at the bottom of the collector, while assuming laminar and plug flow and reports collector efficiencies of up to 100% (a careful reader may look sceptically on such high efficiency values, we discuss this further in Section 2.2.9).

We begin modelling Collector 1 as a two-dimensional channel on an inclined plane. In Section 2.2.2 we model the conservation of energy in the collector as a partial differential equation (PDE). In order to solve this PDE we must first obtain the thermophysical properties of the nanofluid in the collector, the velocity profile of the nanofluid as it flows through the collector, and a term describing the heat source. We use the steady state Navier-Stokes equations for laminar, incompressible fluid flow down an inclined plane under the action of gravity to find the velocity profile of the nanofluid as it flows through the collector in Section 2.2.4. We approximate the heat source term via two fitting parameters, this method was first proposed by Cregan and Myers [10]. In Section 2.2.5 we reproduce Cregan and Myers' fitting parameters for a water-based nanofluid and we also apply this approximation method to a Therminol[®] VP-1 based nanofluid; in doing so we are able to compare how the dimensionless fitting parameters vary across different types of nanofluid. In Section 2.2.6 we rescale and non-dimensionalise the conservation of energy PDE before solving it analytically. We discuss three alternative forms of the analytic solution for temperature; two of which include hyper-geometric functions, and the other includes a series solution. These analytic solutions provide us with a framework to discuss the performance

of an NDASC in Section 2.2.10 after we apply realistic parameter values from a case study in Section 2.2.7.

2.2 Model

2.2.1 Introduction

We model Collector 1 as a two-dimensional channel on a plane which is inclined at an angle of θ to the horizontal. As shown in Figure 2.2, x^* is the coordinate in the downstream direction, and z^* is the perpendicular distance downwards from the upper surface (* denotes a dimensional variable). Thermal diffusion in the metallic nanoparticles is significantly faster than in the fluid. Hence, the particle temperature matches that of the fluid and the nanofluid may be modelled as a single-phase isotropic fluid [37]. Note that $H \ll L$ ($H \sim O(10^{-3}\text{m})$, $L \sim O(1\text{m})$), and the nanofluid flow is laminar and in the x^* direction. The underside of the collector ($z^* = H$) is completely insulated, heat is lost due to Newton cooling at the upper panel ($z^* = 0$), and the temperature of the surrounding air, T_A^* , remains constant. Also, the nanofluid enters the collector with initial temperature T_I^* , and absorbs solar radiation volumetrically.

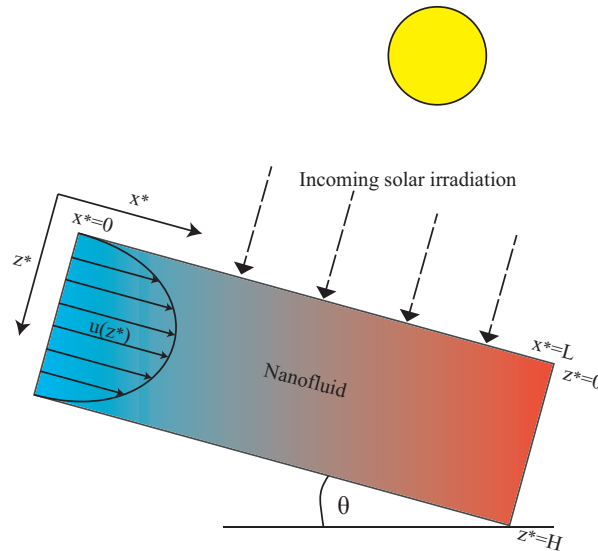


Figure 2.2: Schematic of nanofluid based solar collector as modelled in this chapter.

2.2.2 Conservation of energy

Conservation of heat energy in the system is governed by the continuity equation:

$$\rho_{nf} c_{p,nf} T_{t^*}^* + \nabla \cdot \mathbf{j} = q, \quad (2.2.1)$$

where $c_{p,nf}$ is the nanofluid heat capacity, ρ_{nf} is the nanofluid density, $T^*(x^*, z^*)$ is the nanofluid temperature, \mathbf{j} is the total flux, and q is the volumetric source. In this chapter we only consider the steady-state case where the fluid is incompressible, and \mathbf{j} is the sum of the advective and diffusive fluxes. Therefore the conservation of energy equation in this system is

$$\rho_{nf} c_{p,nf} \mathbf{u} \cdot \nabla T^* = k_{nf} \nabla^2 T^* + q, \quad (2.2.2)$$

where k_{nf} is the nanofluid thermal conductivity. Also, there is a zero flux boundary condition at $z^* = H$ due to the underside of the collector being insulated, and a newton cooling (or heating) boundary condition at $z^* = 0$, the top of the collector. More explicitly these boundary conditions are

$$\left. \frac{\partial T^*}{\partial z^*} \right|_{z^*=H} = 0, \quad k_{nf} \left. \frac{\partial T^*}{\partial z^*} \right|_{z^*=0} = h_s \left(T^* \Big|_{z^*=0} - T_{Amb}^* \right), \quad (2.2.3)$$

and the inlet and outlet conditions are

$$T^* \Big|_{x^*=0} = T_I^* \quad \left. \frac{\partial T^*}{\partial x^*} \right|_{x^*=L} = 0. \quad (2.2.4)$$

2.2.3 Nanofluid properties

The nanofluid properties, such as density, heat capacity and thermal conductivity, depend on the associated base fluid and nanoparticles properties, as well as the particle volume fraction, f_v . We note that, in reality, these properties are also temperature dependent; however, they do not vary much across small temperature fluctuations. Hence for simplicity, we calculate them using the inlet temperature, and assume they remain constant as the nanofluid flows through the collector. The nanofluid density and specific heat capacity are calculated using classical mixing theory:

$$\rho_{nf} = f_v \rho_{np} + (1 - f_v) \rho_{bf}, \quad c_{p,nf} = \frac{f_v \rho_{np} c_{p,np} + (1 - f_v) \rho_{bf} c_{p,bf}}{\rho_{nf}}, \quad (2.2.5)$$

where the subscripts bf , and np denote base fluid, and nanoparticle, respectively. It is well-known that the thermal conductivity of a nanofluid may be significantly higher than that predicted by the classical Maxwell theory. This has led to many models and mechanisms to explain the ‘enhanced thermal conductivity’. Yu and Choi [69] add a nanolayer around the particle, with unknown thickness and conductivity. Other models are either multi-component or include clustering. In each case, the correct choice of the introduced unknowns permits better agreement with experiment. Myers et al. [43], point out that the Maxwell model is derived from the assumptions of steady-state heat flow on an infinite domain, so it is only valid for highly disperse nanofluids (with effectively an infinite distance between particles). Hence, it should not be expected to hold for typical nanoparticle volume fractions. Myers et al. [43] perform the analysis for unsteady heat flow over a finite fluid volume and obtain

$$k_{nf} = \frac{k_{bf}}{\left(1 - f_v^{1/3}\right)^2} \left[(1 - f_v) + f_v \frac{\rho_{np} c_{p,np}}{\rho_{bf} c_{p,bf}} \right] \frac{n - 1}{2(n + 1)} \left[\frac{1 + f_v^{1/3}}{2} - \frac{1}{n + 1} \right]^{-1}, \quad (2.2.6)$$

where $n = 2.233$ results from the solution technique. Equation (2.2.6) is accurate for higher volume fractions than Maxwell’s model and has no fitting parameters. It also shows excellent agreement with experimental results; as f_v increases, Maxwell’s model under-predicts thermal conductivity; see for example Figure 4 in Myers et al. [43] which shows that at $f_v = 0.01$, (2.2.6) outperforms Maxwell’s model.

We note that typical NDAPSC particle volume fractions are in the range of $0 \leq f_v \leq 0.01$; a nanofluid’s thermophysical properties approach those of its base fluid at such low particle concentrations. For example, at 50°C the thermophysical properties of pure water are $\rho = 0.988 \times 10^3 \text{ kg m}^{-3}$, $c_p = 4.181 \times 10^3 \text{ J kg}^{-1} \text{ K}^{-1}$, and $k = 0.644 \text{ W m}^{-1} \text{ K}^{-1}$; meanwhile a water/Aluminium nanofluid at $f_v = 0.01$ has $\rho = 0.998 \times 10^3 \text{ kg m}^{-3}$, $c_p = 4.128 \times 10^3 \text{ J kg}^{-1} \text{ K}^{-1}$, and $k = 0.65 \text{ W m}^{-1} \text{ K}^{-1}$; the density, heat capacity, and thermal conductivity change by only 1%, -1.3% , and 0.9% , respectively, as f_v increases from 0 to 0.01. Therminol[®] VP-1 is another commonly used base fluid in nanofluid-based solar collectors, and at 50°C the thermophysical properties of pure Therminol[®] VP-1 are $\rho = 1.0395 \times 10^3 \text{ kg m}^{-3}$, $c_p = 1.6301 \times 10^3 \text{ J kg}^{-1} \text{ K}^{-1}$, and $k = 0.1332 \text{ W m}^{-1} \text{ K}^{-1}$. At the same temperature, a Therminol[®] VP-1/Aluminium nanofluid at $f_v = 0.01$ has

$\rho = 1.0561 \times 10^3 \text{ kg m}^{-3}$, $c_p = 1.612 \times 10^3 \text{ J kg}^{-1} \text{ K}^{-1}$, and $k = 0.1388 \text{ W m}^{-1} \text{ K}^{-1}$; the density, heat capacity, and thermal conductivity change by only 1.6%, -1.14%, and 4.3%, respectively as f_v increases from 0 to 0.01.

Nanofluids also have different optical properties compared to their base fluids. In particular, adding nanoparticles to a base fluid dramatically increases the amount of light that is absorbed and scattered, which leads to an increase in the efficiency of a DASC. Attenuation of the solar radiation takes place through scattering and absorption in the nanofluid and is accounted for by the extinction coefficient:

$$K_e = K_a^{bf} + K_s^{bf} + K_a^{np} + K_s^{np}, \quad (2.2.7)$$

where K_a and K_s are the absorption and scattering coefficients, respectively. We assume independent scattering in the nanofluid and thus the intensities may be added [60]. For pure fluids, light scattering is negligible, and only the attenuation due to absorption need be considered [33]. Hence, the spectral absorption and scattering coefficients for the base fluid are

$$K_a^{bf} = (1 - f_v) \frac{4\pi\kappa_a^{bf}}{\lambda}, \quad K_s^{bf} \approx 0, \quad (2.2.8)$$

where κ_a^{bf} is the fluid index of absorption, and λ is the wavelength. We note that we have modified the definition of K_a^{bf} from [10, 33] to account for the base fluid's volume fraction via the $(1 - f_v)$ term. For small particle volume fractions, $(1 - f_v) \approx 1$, but as f_v rises, the definition in (2.2.8) is more precise. The dominant wavelengths of incoming solar radiance are greater than 250 nm, and are thus at least ten times larger than the mean diameter (D) of typical NDASC nanoparticles ($< 25 \text{ nm}$). Hence, the higher order spectral components associated with Mie scattering theory may be neglected, and the Rayleigh scattering approximation is applicable [59]. The extinction coefficient for a spherical nanoparticle [4] is

$$K_a^{np} + K_s^{np} = \frac{3f_v}{2D} (Q_{np}^a + Q_{np}^s). \quad (2.2.9)$$

From [10, 53, 59, 63], the nanoparticle absorption and scattering efficiencies are

$$Q_{np}^a = 4\alpha \operatorname{Im} \left\{ \frac{m^2 - 1}{m^2 + 2} \left[1 + \frac{\alpha^2}{15} \left(\frac{m^2 - 1}{m^2 + 2} \right) \frac{m^4 + 27m^2 + 38}{2m^2 + 3} \right] \right\}, \quad (2.2.10)$$

$$Q_{np}^s = \frac{8}{3} \alpha^4 \left| \frac{m^2 - 1}{m^2 + 2} \right|^2, \quad (2.2.11)$$

where $\alpha = (\pi D)/\lambda$ is the size parameter, n_{np} and n_{bf} are the refractive indices, κ_{np} is the nanoparticle absorption index, and $m = (n_{np} + i\kappa_{np})/n_{bf}$ is the relative complex refractive index of particles to the fluid. The values for n_{np} , n_{bf} , and κ_{np} depend on the nanoparticle and base fluid. We note that, although most NDASC studies model light scattering via the Rayleigh approximation, several studies include larger nanoparticles and thus require the Mie scattering approximation [35, 41, 46].

2.2.4 Conservation of momentum

We express the conservation of momentum in the system via the steady-state Navier-Stokes equations for laminar, incompressible fluid flow down an inclined plane under the action of gravity

$$(\mathbf{u} \cdot \nabla) \mathbf{u} + \frac{1}{\rho_{nf}} \nabla p^* - \frac{\mu_{nf}}{\rho_{nf}} \nabla^2 \mathbf{u} = \mathbf{g}, \quad (2.2.12)$$

where μ_{nf} is the viscosity of the nanofluid, $\mathbf{u} = (u^*, v^*)$ is the fluid velocity, p^* is the pressure, and \mathbf{g} is the forces exerted on the system due to gravity. Acheson [2] uses the following argument to express (2.2.12) in a simpler form: since $\mathbf{u} = 0$ on $z^* = 0, H$ (due to the no-slip conditions at these boundaries), \mathbf{u} needs to depend on z^* . Furthermore, since we have no reason to believe that \mathbf{u} also depends on anything else, let's explore the case where $\mathbf{u} = (u^*(z^*), v^*(z^*))$. Since the liquid in this system is incompressible, mass continuity implies

$$\frac{\partial v^*}{\partial z^*} = 0, \quad (2.2.13)$$

i.e., v^* is constant. Moreover, for v^* to be constant and also satisfy the no-slip condition, then $v^* = 0$. Therefore, substituting $\mathbf{u} = (u^*(z^*), 0)$ into (2.2.12) yields

$$-\frac{\partial p^*}{\partial x^*} + \mu_{nf} \frac{\partial^2 u^*}{\partial z^{*2}} + \rho_{nf} g \sin \theta = 0, \quad -\frac{\partial p^*}{\partial z^*} + \rho_{nf} g \cos \theta = 0. \quad (2.2.14)$$

We integrate the latter of these equations and apply the boundary condition $p^*(0) = p_a^*$ (where p_a is the ambient pressure), to obtain $p^* = p_a^* + \rho_{nf}gz^* \cos \theta$, and this result implies that $\partial p^*/\partial x^* = 0$. Therefore, a solution for u^* is found by integrating the first PDE in (2.2.14) twice and applying the no-slip boundary conditions at the upper and lower surfaces of the collector yielding

$$u^* = \frac{\rho_{nf}gH^2 \sin \theta}{2\mu_{nf}} \left(\frac{z^*}{H} - \frac{z^{*2}}{H^2} \right). \quad (2.2.15)$$

2.2.5 Heat source

The heat source, q , from 2.2.2 is obtained via an energy balance, whereby the change in the normally-incident solar spectral flux due to attenuation of the nanofluid is dissipated as heat is released. The spectral intensity at the top of the receiver, J_0 , is approximated via Planck's Black-body relation and can be expressed as

$$J_0 = \frac{2hc^2\Omega_S S_{Att} \Upsilon_T}{\lambda^5 \left(\exp \left(\frac{hc}{\lambda k_B T_{Sun}^*} \right) - 1 \right)}, \quad (2.2.16)$$

where h is Plancks constant, c the speed of light, Ω_S the solid angle of the sun, S_{Att} the attenuation of sunlight through the Earths atmosphere, k_B the Boltzmann constant, T_{Sun}^* the temperature of the sun, and Υ_T the transmittance of the glass cover.

We model a system that operates at temperatures below 750 K, and thus follow the approach of Veeraragavan et al. [66] where thermal re-emission in the fluid is presumed negligible since it constitutes less than 5% of the total radiative heat loss. The change in normally incident solar radiation is given by the radiative transport equation

$$\frac{dJ_\lambda^*}{dz^*} = -K_e J_\lambda^*, \quad (2.2.17)$$

with the associated boundary condition $J_\lambda^*|_{z^*=0} = J_0$. Recall that we calculate the extinction coefficient, K_e , using (2.2.7) (which is defined earlier in Section 2.2.3). The solution to (2.2.17) is thus

$$J_\lambda^*(z^*) = J_0 e^{-K_e z^*}. \quad (2.2.18)$$

To determine the radiative flux, $P^*(z^*)$, we integrate (2.2.18) over the entire

spectrum of wavelengths, i.e.,

$$P^*(z^*) = \int_0^\infty J_0 e^{-K_e z^*} d\lambda. \quad (2.2.19)$$

However, (2.2.19) is highly non-linear with respect to wavelength due to the wavelength-dependent J_0 and K_e terms; so, to make analytic progress, we follow the approach of Cregan and Myers [10] and use the method of least squares to approximate this radiative flux integral. They show that the radial flux is well approximated for a water/aluminium nanofluid by the power law

$$\int_0^\infty J_0 e^{-K_e z^*} d\lambda \approx \frac{G_s^*}{\left(1 + \frac{\beta_0}{H} z^*\right)^{\beta_1}}, \quad (2.2.20)$$

where β_0 , and β_1 are dimensionless fitting parameters, and G_s^* is the solar intensity at $z^* = 0$. We differentiate the radial flux, (2.2.20), with respect to z^* to obtain the heat source term

$$q^*(z^*) = -\frac{dP^*}{dz^*} = \frac{G_s^* \beta_0 \beta_1}{H \left(1 + \frac{\beta_0}{H} z^*\right)^{\beta_1 + 1}}. \quad (2.2.21)$$

Incoming radiation enters the receiver at $z^* = 0$ and is attenuated due to the scattering and absorption as it passes through the receiver. The qualitative behaviour of $P^*(z^*)$ is depicted in Figures 2.3 and 2.4. In Figure 2.3 we compare a numerical solution for $P^*(z^*)$ (solid line) with the approximated solution (dashed line) when (a) $H = 0.0012$ m and (b) $H = 0.01$ m for a water/aluminium nanofluid. The qualitative behaviour of the radiative flux integral depends on two parameters: channel depth, and particle volume fraction. As the channel depth increases, the nanofluid absorbs more of the incoming radiation; hence, we observe that the radiative intensity is lower at $z^* = 0.01$ m (Figure 2.3b) than at $z^* = 0.0012$ m (Figure 2.3a) across all particle fractions. Furthermore, radiative intensity is lower at the end of the channel as the nano-particle volume fraction increases; even at small particle volume fractions, the nanofluid absorbs much more of the incoming solar radiation than the pure base fluid. We note that Figure 2.3a is also shown in Cregan and Myers [10], while Figure 2.3b is new. Both Figures 2.3a and 2.3b show good agreement between the fitted functions and the exact solutions, and this result is also demonstrated in Cregan and Myers [10].

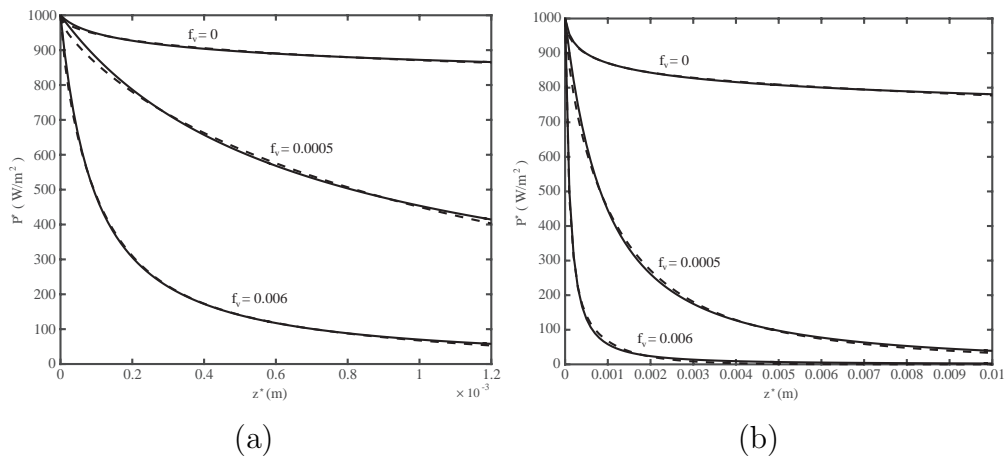


Figure 2.3: Comparison of numerical solution (solid line) for $P^*(z^*)$ with approximate solution (dashed line) when (a) $H = 0.0012$ m and (b) $H = 0.0012$ m for a water/aluminium nanofuid.

While Figure 2.3 shows that the fitted function approximates the exact radiative flux integral quite well in a water based nanofuid, in Figure 2.4 the dashed and solid lines are colinear—this approximation method works even better for a Therminol[®] VP-1 based nanofuid. Figure 2.4 shows the numerical solution for $P^*(z^*)$ (solid line) and the approximated solution for $P^*(z^*)$ (dashed line) when (a) $H = 0.0012$ m and (b) $H = 0.01$ m for a Therminol[®] VP-1/aluminium nanofuid. The qualitative behaviour of $P^*(z^*)$ in a Therminol[®] VP-1 based nanofuid depends on the same two parameters as the water based nanofuid: H , and f_v . However, we note that $P^*(z^*)$ declines faster across all particle volume fractions in Figure 2.3 than in Figure 2.4—water is better than Therminol[®] VP-1 at absorbing solar radiation.

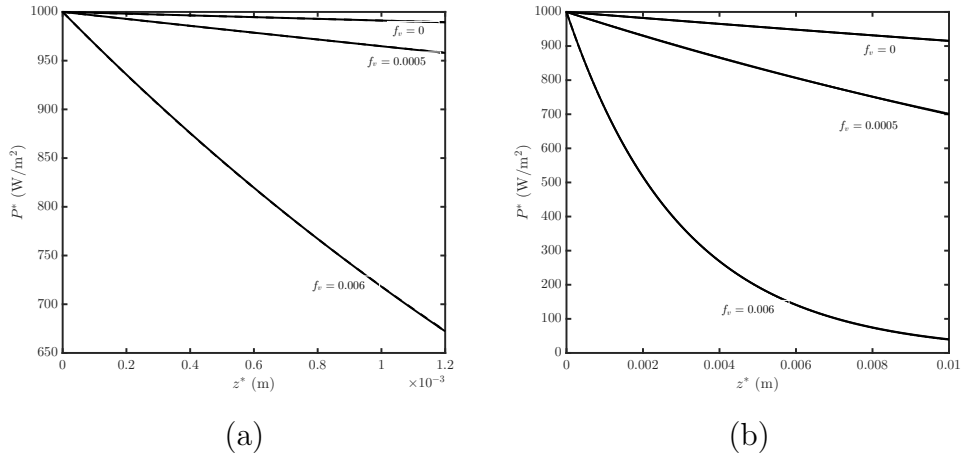


Figure 2.4: Comparison of numerical solution (solid line) for $P^*(z^*)$ with approximate solution (dashed line) when (a) $H = 0.0012$ m and (b) $H = 0.01$ m for a Therminol[®] VP-1/aluminium nanofluid.

Figure 2.5 shows the extinction coefficients for (a) water, and (b) Therminol[®] VP-1-based nanofluids (note that these plots are Figures 5 and 7 from Taylor et al. [59]). While Therminol[®] VP-1 has a larger extinction coefficient than water at shorter wavelengths ($\lambda < 1 \mu\text{m}$), at longer wavelengths the extinction coefficient of water is larger than Therminol[®] VP-1. Since the extinction coefficients of these base fluids are qualitatively different, we would also expect qualitative differences in $P^*(z^*)$, β_0 , and β_1 across the two different base fluids.

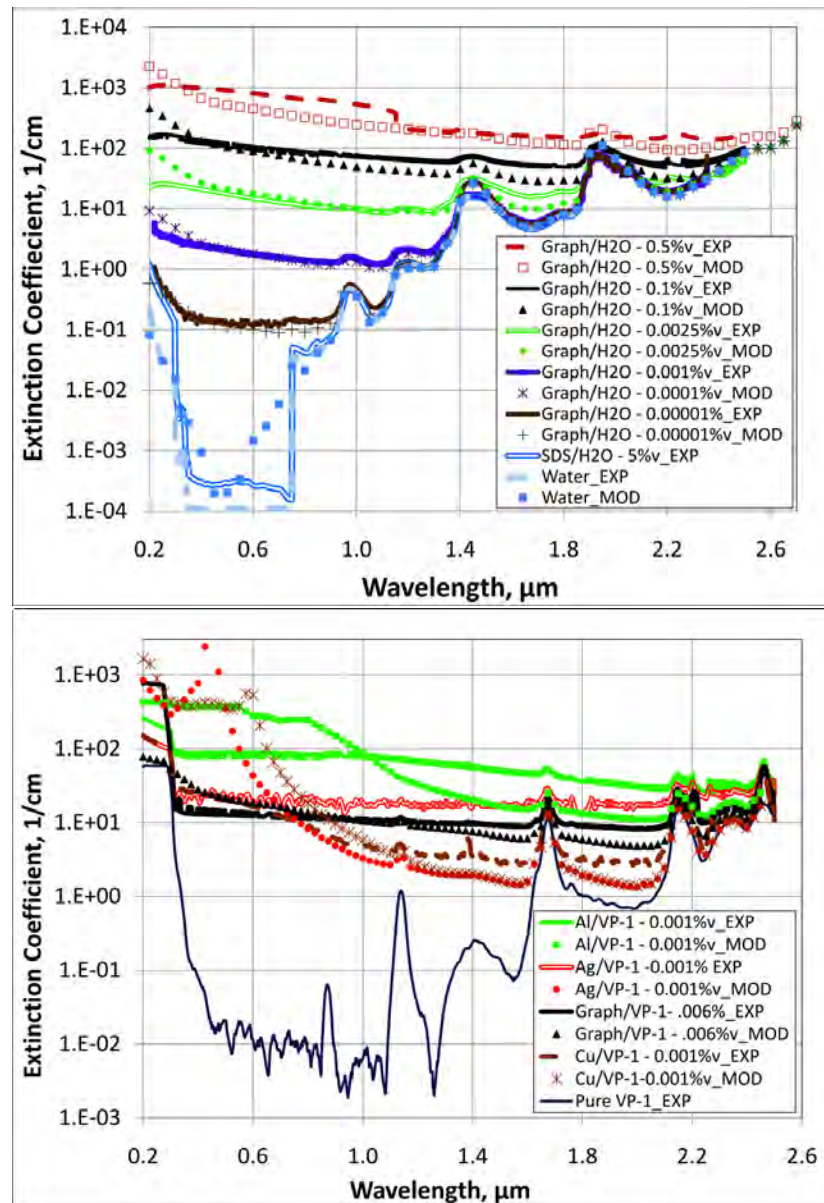


Figure 2.5: Extinction coefficients for (a) water, and (b) Therminol[®] VP-1 based nanofluids from Taylor et al. [59].

The β_0 and β_1 fitting parameters vary across different base fluids, nanoparticle volume fractions, and channel depths. In Figures 2.6 and 2.7 the relationship between the properties of a nanofluid and the fitting parameters are demonstrated for a water based nanofluid with aluminium nanoparticles (Figures 2.6a and 2.6b) and for a Therminol[®] VP-1 based nanofluid with aluminium nanoparticles (Figures 2.7a and 2.7b). Figures 2.6a and 2.6b show the variation of β_0 and β_1 in a

water based nanofluid flowing through two different channel heights. We observe a qualitative difference between how the fitting parameters vary across two different channel heights. Both parameters change rapidly near $f_v = 0$; β_0 decreases, while β_1 increases. However, for larger particle volume fractions β_1 remains $O(1)$, while β_0 rises to $O(100)$. This rise is monotonic for $H = 0.01$ m but is non-linear for $H = 0.07$ m.

In Figures 2.7a and 2.7b we demonstrate how (a) β_0 and (b) β_1 vary across particle volume fraction for $H = 0.01$ m (solid lines) and $H = 0.07$ m (dashed lines) in a Therminol[®] VP-1 based nanofluid. The first fitting parameter, β_0 , increases monotonically with particle volume fraction across both receiver channels for a Therminol[®] VP-1 based nanofluid. The rate of increase, however, differs by an order of magnitude between the two channel heights tested and β_0 rises much quicker with f_v in the deeper receiver. The behaviour of β_1 for a Therminol[®] VP-1 based nanofluid is fundamentally different than the behaviour of β_0 . After an initial rapid decrease near $f_v = 0$, β_1 remains $O(1)$ for larger particle volume fractions.

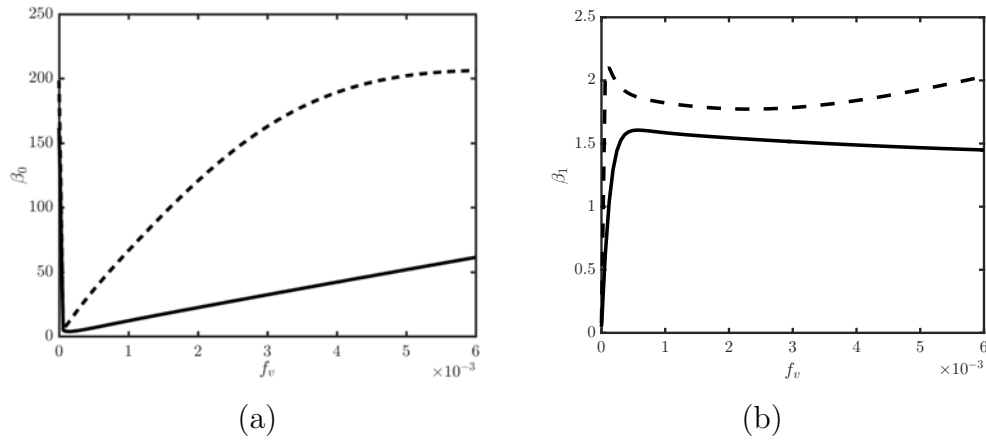


Figure 2.6: Variation of (a) β_0 and (b) β_1 with f_v for $H = 0.01$ m (solid lines) and $H = 0.07$ m (dashed lines) in a water based nanofluid.

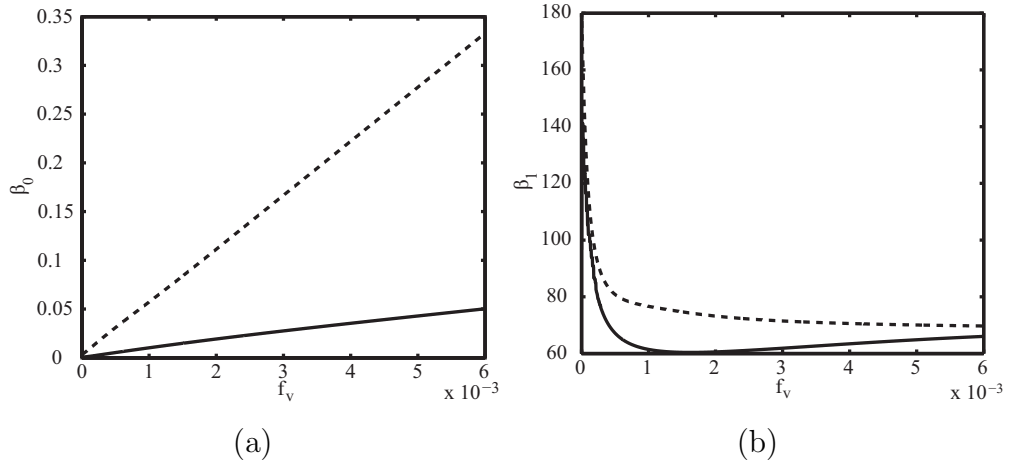


Figure 2.7: Variation of (a) β_0 and (b) β_1 with f_v for $H = 0.01$ m (solid lines) and $H = 0.07$ m (dashed lines) in a Therminol[®] VP-1 based nanofluid.

2.2.6 Dimensional analysis

Recall, the conservation of energy when this collector is at a steady-state is expressed via

$$\rho_{nf} c_{p,nf} \mathbf{u} \cdot \nabla T^* = k_{nf} \nabla^2 T^* + q. \quad (2.2.22)$$

Using the velocity from (2.2.15), and the source term from (2.2.21), we write this conservation of energy more explicitly as

$$\frac{c_{p,nf} \rho_{nf}^2 g \sin \theta}{2\mu_{nf}} (Hz^* - z^{*2}) \frac{\partial T^*}{\partial x^*} = k_{nf} \frac{\partial^2 T^*}{\partial z^{*2}} + k_{nf} \frac{\partial^2 T^*}{\partial x^{*2}} + \frac{G_S \beta_0 \beta_1}{(1 + \beta_0 \frac{z^*}{H})^{\beta_1+1}}, \quad (2.2.23)$$

with boundary conditions,

$$\left. \frac{\partial T^*}{\partial z^*} \right|_{z^*=H} = 0, \text{ and } k_{nf} \left. \frac{\partial T^*}{\partial z^*} \right|_{z^*=0} = h_s \left(T^* \Big|_{z^*=0} - T_{Amb}^* \right), \quad (2.2.24)$$

and the inlet and outlet conditions

$$T^* \Big|_{x^*=0} = T_I^* \quad \frac{\partial T^*}{\partial x^*} \Big|_{x^*=L} = 0. \quad (2.2.25)$$

We non-dimensionalise this model using the dimensionless variables

$$x^* = Lx, \quad z^* = Hz, \quad T^* = T\Delta T + T_I^*, \quad (2.2.26)$$

where the source term drives the temperature scale and ΔT is chosen such that

$$\Delta T = \frac{G_S L \beta_0 \beta_1}{H U c_{p,nf} \rho_{nf}}, \quad \text{where} \quad U = \frac{\rho_{nf} g_{nf} H^2 \sin \theta}{2 \mu_{nf}}. \quad (2.2.27)$$

Therefore, in dimensionless form (2.2.23) is

$$(z - z^2) \frac{\partial T}{\partial x} = \gamma \frac{\partial^2 T}{\partial z^2} + \frac{1}{\text{Pe}} \frac{\partial^2 T}{\partial x^2} + \frac{1}{(1 + \beta_0 z)^{\beta_1 + 1}}, \quad (2.2.28)$$

where γ and the Peclet number, Pe , are the dimensionless parameters that describe the ratio of diffusion to advection. These parameters are given by

$$\gamma = \frac{k_{nf} L}{c_{p,nf} \rho_{nf} U H^2}, \quad \text{Pe} = \frac{\rho_{nf} c_{p,nf} L U}{k_{nf}}. \quad (2.2.29)$$

We note that (2.2.28) is an elliptic partial differential equation, also, since $1/\text{Pe}$ is $O(10^{-8})$ the system has a boundary layer that is $O(10 \text{ nm})$ at $x^* = L$. Common NDASC modelling practice suggests that we neglect the $1/\text{Pe}$ term (and consequently, the boundary layer at $x^* = L$) [10, 36, 62, 63], thus approximating (2.2.28) with the parabolic partial differential equation

$$(z - z^2) \frac{\partial T}{\partial x} = \gamma \frac{\partial^2 T}{\partial z^2} + \frac{1}{(1 + \beta_0 z)^{\beta_1 + 1}}. \quad (2.2.30)$$

Close to the boundary at $x = 1$, one can rescale the system using the dimensionless variable \bar{x} , where \bar{x} is defined such that $x = 1 - 1/\text{Pe} \bar{x}$. In the boundary layer the system is governed by

$$-(z - z^2) \frac{\partial \bar{T}}{\partial \bar{x}} = \frac{\partial^2 \bar{T}}{\partial \bar{x}^2} \quad (2.2.31)$$

at leading order. This differential equation has a solution of the form

$$\bar{T}(\bar{x}, z) = f_1(z) e^{-(z-z^2)\bar{x}} + f_2(z), \quad (2.2.32)$$

and after we impose the rescaled boundary condition at the outlet, $\bar{T}_{\bar{x}}|_{\bar{x}=0} = 0$, we find that $f_1(z) = 0$, and so $\bar{T}(z) = f_2(z)$. The function $f_2(z)$ is obtained from matching with the outer solution, and so $\bar{T}(z) = T(x = 1, z)$ where $T(x, z)$ is the solution to (2.2.30) at the boundary. This leads to a weak boundary layer at leading order where T does not vary with x . One would have to go

to the second order to resolve this. Section 2.2.10 contains further discussion on the implications of this approximation method. We also rescale and non-dimensionalise the boundary conditions, obtaining

$$\left. \frac{\partial T}{\partial z} \right|_{z=1} = 0, \text{ and } \left. \frac{\partial T}{\partial z} \right|_{z=0} = \text{Nu} \left(T \Big|_{z=0} - \hat{T} \right) \quad (2.2.33)$$

where Nu, the Nusselt number, is the well known dimensionless parameter describing the ratio of convective to conductive heat transfer on the upper panel—more specifically, $\text{Nu} = (Hh_s)/k_{nf}$. Meanwhile, the inlet and outlet conditions are

$$T \Big|_{x=0} = 0, \text{ and } \left. \frac{\partial T}{\partial x} \right|_{x=1} = 0, \quad (2.2.34)$$

although, we note that the outlet condition is not satisfied when the boundary layer at $x^* = L$ is ignored.

2.2.7 Case study

As a case study for exploring our model further, we consider an Aluminum/Water nanofluid and, unless otherwise stated, use the parameter values given in Table 2.1, as these values are largely used by Cregan and Myers [10] and Tyagi et al. [63]. The thermophysical properties of the aluminium nanoparticles are taken from [51]. The spectral-dependent refractive indexes n_{np} and n_{bf} and the nanoparticle absorption index κ_{np}^a are from [47, 51].

Quantity	Symbol	Value	Units
Collector length/width/height	$L/W/H$	1, 1, 0.0012	m
Collector angle of inclination	θ	$\pi/9$	-
Viscosity (H ₂ O)	μ_{bf}	10^{-3}	kg m ⁻¹ s ⁻¹
Surface heat transfer coefficient	h_s	6.43	W m ⁻² K ⁻¹
Air/inlet nanofluid temperature	T_{Amb}/T_I^*	298.15/308.15	K
Incident solar radiation	G_S	1000	W m ⁻²
Gravity	g	9.8	m s ⁻²
Density water/aluminium	ρ_{bf}/ρ_{np}	1000/2700	kg m ⁻³
Conductivity water/aluminium	k_{bf}/k_{np}	0.609/247	W m ⁻¹ K ⁻¹
Specific heat capacity water/aluminium	$c_{p,bf}/c_{p,np}$	4187/900	J kg ⁻¹ K ⁻¹
Fitting parameters (for $\phi = 0.006$)	β_0/β_1	10.60/1.14	-
Dimensionless parameters	$\gamma/\text{Nu}/\hat{T}/\text{Pe}$	0.042/0.012/11.48/1.78 × 10 ⁷	-

Table 2.1: Solar collector and nanofluid parameters and physical constants from Cregan and Myers [10].

2.2.8 Solution method

The system described by (2.2.30) and (2.2.33) is a second-order, linear partial differential equation. We solve for T via the method of separation of variables. The presence of non-homogeneous terms in the system suggests a solution of the form $T(x, z) = v(x, z) + w(z)$ leading to

$$(z - z^2)v_x = \gamma v_{zz} + \gamma w_{zz} + \frac{1}{(1 + \beta_0 z)^{\beta_1 + 1}}. \quad (2.2.35)$$

We choose $w(z)$ such that

$$\gamma w_{zz} + \frac{1}{(1 + \beta_0 z)^{\beta_1 - 1}} = 0, \quad (2.2.36)$$

which has a solution

$$w(z) = \frac{1}{\gamma \beta_1 (\beta_1 - 1) \beta_0^2 (1 + \beta_0 z)^{\beta_1 + 1}} + C_1 z + C_2. \quad (2.2.37)$$

The integration constants, C_1 and C_2 , are obtained after applying the boundary conditions (which are defined in (2.2.33)); more explicitly, these constants are:

$$C_1 = -\frac{1}{\gamma \beta_0 \beta_1 (1 + \beta_0)^{\beta_1}}, \quad C_2 = \frac{1}{Nu} \left(\frac{1}{\gamma \beta_0 \beta_1} + C_1 \right) + \frac{1}{\gamma \beta_0^2 \beta_1 (\beta_1 - 1)} + \hat{T}. \quad (2.2.38)$$

Returning our attention to $v(x, z)$, the homogeneous part of $T(x, z)$, we assume $v(x, z) = f(x)g(z)$; therefore, (2.2.35) is rearranged to obtain

$$\frac{f_x}{\gamma f} = \frac{g_{zz}}{(z - z^2)g} = -p_n^2 \quad (2.2.39)$$

for some constant p_n . We find expressions for $f(x)$ and $g(z)$ by solving the ordinary differential equations

$$\frac{f_x}{\gamma f} = -p_n^2 \quad (2.2.40)$$

and

$$\frac{g_{zz}}{(z - z^2)g} = -p_n^2. \quad (2.2.41)$$

The solution to (2.2.40) is $f(x) = K_1 e^{-\gamma p_n^2 x}$ for some constant K_1 . Meanwhile, we obtain $g(z)$ via a change of variables: first we let

$$z = \frac{\bar{z}}{\sqrt{2p_n}} + \frac{1}{2}, \quad (2.2.42)$$

which enables us to rewrite (2.2.41) as

$$\bar{g}_{\bar{z}\bar{z}} + \left(\nu + \frac{1}{2} - \frac{1}{4}\bar{z}^2\right)\bar{g} = 0, \quad (2.2.43)$$

where $\nu = (p_n - 4)/8$. Equation (2.2.43) has solutions of the form

$$\bar{g}(\bar{z}) = K_2 D_\nu(\bar{z}) + K_3 D_\nu(-\bar{z}) \quad (2.2.44)$$

for some constants K_2 and K_3 , where $D_a(b)$ is the parabolic cylinder function (we are using the notion described in Whittaker [68] for this expression). However, (2.2.44) is still defined in terms of \bar{z} and so we rewrite it in terms of its original variable z ,

$$g(z) = K_2 D_\nu\left(\sqrt{2p_n}\left[z - \frac{1}{2}\right]\right) + K_3 D_\nu\left(-\sqrt{2p_n}\left[z - \frac{1}{2}\right]\right), \quad (2.2.45)$$

Which suggests a solution to our model of the form

$$T(x, z) = w(z) + \sum_{n=1}^{\infty} \left[C_n \exp(-\lambda p_n^2 x) \left[D_\nu\left(\sqrt{2p_n}\left[z - \frac{1}{2}\right]\right) + K_3 D_\nu\left(-\sqrt{2p_n}\left[z - \frac{1}{2}\right]\right) \right] \right].$$

The weight function in the Sturm-Liouville problem, defined by (2.2.41), is $(z - z^2)$ and so orthogonality requires

$$\int_0^1 (z - z^2) g_n g_m dz = 0 \quad (2.2.46)$$

for $n \neq m$. The series coefficient C_n is determined, after imposing the inlet condition, and the constant K_3 is obtained by applying the boundary conditions;

therefore,

$$K_3 = \frac{\nu D_{\nu-1} \left(\sqrt{\frac{p_n}{2}} \right) - D_{\nu+1} \left(\sqrt{\frac{p_n}{2}} \right)}{\nu D_{\nu-1} \left(\sqrt{-\frac{p_n}{2}} \right) - D_{\nu+1} \left(-\sqrt{\frac{p_n}{2}} \right)}, \quad (2.2.47)$$

$$C_n = - \frac{\int_0^1 w(z)(z - z^2) [D_\nu (\sqrt{2p_n} [z - \frac{1}{2}]) + K_3 D_\nu (-\sqrt{2p_n} [z - \frac{1}{2}])] dz}{\int_0^1 (z - z^2) [D_\nu (\sqrt{2p_n} [z - \frac{1}{2}]) + K_3 D_\nu (-\sqrt{2p_n} [z - \frac{1}{2}])]^2 dz}, \quad (2.2.48)$$

where the eigenvalues, p_n satisfy

$$\begin{aligned} & \left[\nu D_{\nu-1} \left(-\sqrt{\frac{p_n}{2}} \right) - D_{\nu+1} \left(-\sqrt{\frac{p_n}{2}} \right) - K_3 \left[\nu D_{\nu-1} \left(\sqrt{\frac{p_n}{2}} \right) - D_{\nu+1} \left(\sqrt{\frac{p_n}{2}} \right) \right] \right] \\ & = \sqrt{\frac{2Nu^2}{p_n}} \left[D_\nu \left(-\sqrt{\frac{p_n}{2}} \right) + K_3 D_\nu \left(\sqrt{\frac{p_n}{2}} \right) \right]. \end{aligned} \quad (2.2.49)$$

We acknowledge that some software programs do not have inbuilt parabolic cylinder functions, and so this hypergeometric function based solution is not universally practical; therefore, in Appendix A we demonstrate two alternative expressions for this analytic solution: one is an expression in terms of an alternative hypergeometric function, and the other is expressed via an infinite series.

2.2.9 Efficiency

Collector efficiency is defined as the ratio of usable thermal energy to incident solar energy. Otanicar et al. [48] and Tyagi et al. [63] calculate the efficiency, η , of an NDASC with

$$\eta = \frac{\dot{m} \rho_{nf} c_{p,nf} (\hat{T}_O^* - T_I^*)}{G_S A}, \quad (2.2.50)$$

where \dot{m} is the mass flow rate of the fluid through the collector, \hat{T}_O^* is the mean fluid outlet temperature and A is the top surface area of the collector—this is a three-dimensional calculation of efficiency. Cregan and Myers [10] calculate the solar collector efficiency in two-dimensional space with

$$\eta = \frac{\dot{m} \rho_{nf} c_{p,nf} (\hat{T}_O^* - T_I^*)}{G_S L}. \quad (2.2.51)$$

However, these analytic expressions are limited since they do not consider depth-dependence in the nanofluid velocity profile. Lee and Jang [36] alter this efficiency calculation to be a true measure of the ratio of usable thermal energy to incident solar energy, i.e.,

$$\eta = \frac{\rho_{nf} c_{p,nf}}{G_S L} \int_0^H (T_O^*(z^*) - T_I^*) u(z^*) dz^*, \quad (2.2.52)$$

or in its non-dimensional form

$$\eta = \beta_0 \beta_1 \int_0^1 T_O(z) (z - z^2) dz. \quad (2.2.53)$$

However, sometimes the ratio of usable thermal energy to incident solar energy is a bad measure of collector efficiency. For example, Turkyilmazoglu [62] use this definition of efficiency while modelling an NDASC with an isothermal (fixed temperature) base panel (rather than the insulated base panel which is used in this chapter's model). Turkyilmazoglu reports 100% efficiency; however, this result only occurs when the base panel is sufficiently hotter than the liquid flowing through the receiver. In fact, Turkyilmazoglu might have even reported $\eta > 100\%$ had the base panel been heated further. Of course, efficiencies exceeding 100% are unphysical. Since the base of Turkyilmazoglu's collector is at a constant (in this case elevated) temperature, the temperature gradient of the nanofluid at $z^* = H$ is non-zero, and the isothermal base panel is a source of heat. In Figure 7 (c) (from Turkyilmazoglu [62]), for example, the nanofluid's initial temperature rise is predominantly due to the fixed temperature boundary condition at the base panel. This additional heating phenomenon is not included in an efficiency expression defined by (2.2.52). We propose, that in the case of a non-zero flux boundary condition, this additional source/sink of heat should be accounted for, i.e.,

$$\eta = \frac{\rho_{nf} c_{p,nf} \int_0^H (T_O^*(z^*) - T_I^*) u(z^*) dz^*}{G_S^* L + k_{nf} \int_0^L \left. \frac{dT^*}{dz^*} \right|_{z^*=H} dx^*}, \quad (2.2.54)$$

the second term in the denominator represents the energy entering the system across the boundary at $z^* = H$ along the length of the collector.

2.2.10 Results

We remind the reader that the analytic expression of temperature that is obtained in this chapter is approximately equivalent to that which is proposed by Lee and Jang [36] (who analytically reproduced the results from Tyagi et al. [63]). Therefore, the results in this chapter closely mirror those reported in both Tyagi et al., and Lee and Jang. This chapter also makes a direct comparison to the model proposed by Cregan and Myers [10].

Figure 2.8 shows the temperature of the system versus channel depth for a water-aluminium nanofluid at $x = 0.25L$ (dotted line), $x = 0.5L$ (dash-dotted line), $x = 0.75L$ (dashed line) and $x = L$ (solid line) for $f_v = 0.006$. Incoming radiation is greatest near $z^* = 0$, so we observe the highest temperatures near the upper panel, and temperature decreases with channel depth. Also, we note that the temperature increases as the nanofluid flows through the channel. When $z^* = H$ we observe that the temperature gradient is zero, this is due to the imposed zero flux boundary condition.

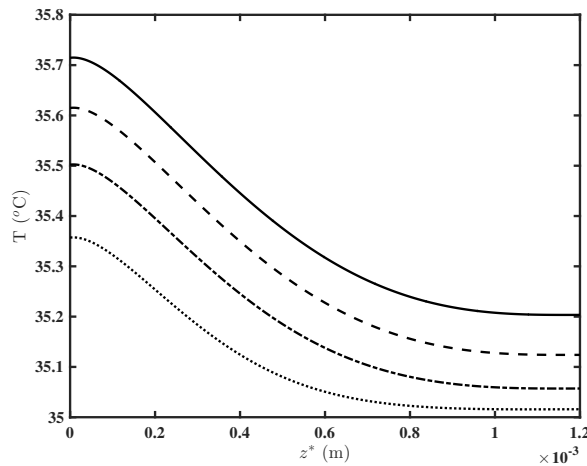


Figure 2.8: Temperature profiles for a water-aluminium nanofluid at $x = 0.25L$ (dotted line), $x = 0.5L$ (dash-dotted line), $x = 0.75L$ (dashed line) and $x = L$ (solid line) for $f_v = 0.006$.

Figure 2.9 plots the efficiency versus collector depth for the model proposed in this chapter (solid lines) and the plug flow velocity model from Cregan and Myers [10] (dashed lines). Firstly, the efficiency—as calculated by both models—increases as H increases and the collector absorbs more of the overall available incoming radiation; this is to be expected. However, Figure 2.9 also demonstrates

that the inclusion of depth-dependent velocity can have a small, but noticeable, effect on the efficiency of an NDASC. The model incorporating a depth-dependent velocity predicts $O(1\%)$ lower efficiencies than the plug flow model proposed by Cregan and Myers [10]. The depth-dependent velocity model predicts slower velocities close to $z^* = 0$ than the plug flow model; this leads to hotter temperatures at the upper panel which in turn leads to greater heat losses and lower efficiencies. Lee and Jang [36] report collector efficiency differences of up to 15 % when comparing the plug-flow and depth-dependent models. However, in order to achieve these differences they alter the surface heat transfer coefficient from $6.43 \text{ W/m}^2 \text{ K}$ to $250 \text{ W/m}^2 \text{ K}$. Although $250 \text{ W/m}^2 \text{ K}$ is a general maximum value of forced convection heat transfer coefficient for gases, it is much larger than what one might expect for a typical NDASC [22, 63]. At $h_s = 6.43 \text{ W/m}^2 \text{ K}$, which is a much more realistic heat surface transport coefficient, Lee and Jang [36] report differences between the two models that are comparable to the ones reported here ($O(1\%)$).

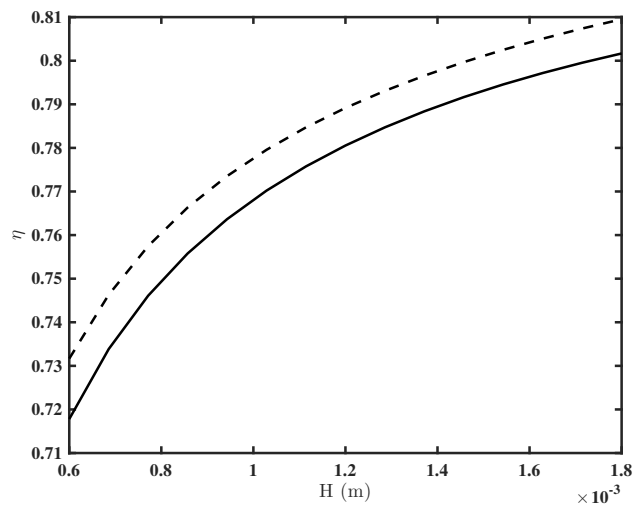


Figure 2.9: Collector efficiency versus collector height for plug flow (dashed line), and depth-dependent flow (solid line), when $\phi = 0.006$.

Figure 2.10 shows the efficiency of the solar collector versus particle volume fraction for $H = 0.0006$ (solid line), $H = 0.0012$ (dashed line), and $H = 0.0018$ (dot-dashed line). We observe a sharp increase in collector efficiency across each of the three height configurations when nanoparticles are first added to the base

fluid and particle volume fractions are quite low. The presence of nanoparticles increases the rate at which incoming radiation is absorbed into the working fluid. However, as the nanoparticle volume fraction continues to rise, we observe different qualitative behaviours in all three of the collector configurations. This initial increase is sharpest at larger collector depths and is progressively more gradual as the collector depth decreases. The efficiencies of all three collector configurations plateau with further increase in f_v —after the system has absorbed all of the available incoming radiation any additional increase in particle volume fraction does not lead to any further efficiency enhancement. We note that Tyagi et al. [63] also observe this efficiency plateau at $\eta \sim 80\%$ in a numerical study of NDASCs.

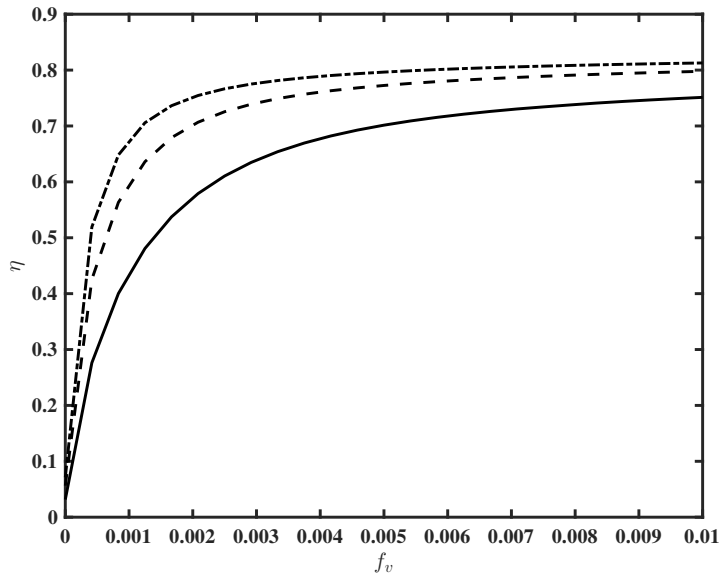


Figure 2.10: Efficiency of the solar collector versus particle volume fraction for $H = 0.0006$ (solid line), $H = 0.0012$ (dashed line), and $H = 0.0018$ (dot-dashed line).

Figure 2.11 illustrates collector efficiency versus $1/Pe$, where the efficiency is calculated using the full model, i.e., (2.2.28) (dashed line), and the reduced model i.e., (2.2.30) (solid line). Recall that the (2.2.30) neglects the $1/Pe$ term (and consequently, the boundary layer at $x^* = L$). In this plot, (2.2.28) is solved numerically (with a mesh of 4000×100 uniform nodes) via an elliptic finite difference scheme, also, $1/Pe$ is varied while the other dimensionless param-

ters are kept constant. When $1/\text{Pe}=1$, the simplified system overestimates the NDASC's efficiency by 73.5%. This error decreases as $1/\text{Pe}$ decreases, reducing to 3.5% when $1/\text{Pe}=10^{-3}$. In this chapter's case-study, $1/\text{Pe}$ is $O(10^{-8})$, and so neglecting the boundary layer introduces negligible errors. However, this analysis illustrates that it would not be appropriate to neglect the boundary layer if $1/\text{Pe}$ was significantly larger.

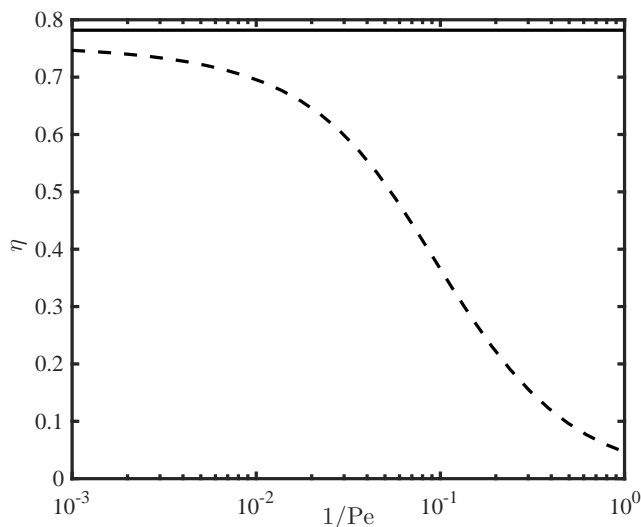


Figure 2.11: Collector efficiency versus $1/\text{Pe}$, where the efficiency is calculated using the full model, i.e., (2.2.28) (dashed line), and the reduced model i.e., (2.2.30) (solid line), when $\phi = 0.006$.

Figure 2.12 compares the temperature rise across the system ($T^* - T_I^*$) when T^* is calculated using: (a) the full model i.e., (2.2.28) with $1/\text{Pe} = 1 \times 10^{-3}$, and (b) the reduced model i.e., (2.2.30). The temperatures are slightly higher at the $x^* = L$ boundary in the reduced system, but overall both plots are quite similar. Qualitative similarities between Figures 2.12 (a) and (b) were to be expected since $1/\text{Pe} = 1 \times 10^{-3}$ corresponds to a small boundary layer of $O(1 \text{ mm})$. However, while this boundary layer is small, it does have a noticeable impact on the system. Due to computational limitations, we are unable to model the solution to (2.2.28) when $1/\text{Pe}$ is $O(10^{-8})$ (as it is in the case-study in this chapter). However, one would expect to find negligible differences between solutions to the full model and the reduced model if $1/\text{Pe}$ was that small.

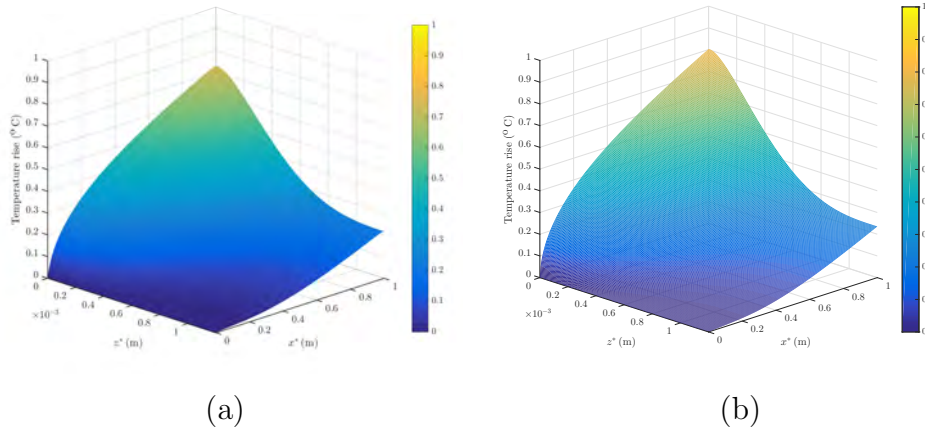


Figure 2.12: Temperature rise when the temperature is calculated with: (a) the full model i.e., (2.2.28) and $1/Pe = 1 \times 10^{-3}$, and (b) the reduced model i.e., (2.2.30), when $\phi = 0.006$.

2.3 Summary and discussion

In this chapter we developed a two-dimensional model for the efficiency of an inclined parallel plate nanofluid-based direct absorption solar collector. This type of collector has been modelled previously [10, 36, 62, 63], and all of the components of this model have been proposed in previous research; however, we are the first to combine them. Cregan and Myers [10] model the collector via the less accurate plug flow approximation and obtain an analytic expression for the radiative flux integral, whilst Lee and Jang [36] model the collector using a depth-dependent flow but they numerically evaluate the term describing the source of heat. We defined the system geometry in Section 2.2.1 and expressed the conservation of energy in Section 2.2.2. The conservation of energy equation requires values for the thermophysical properties of the nanofluid (which we described in Section 2.2.3), a fluid velocity term (which is obtained via a conservation of momentum argument in Section 2.2.4), and a heat source term (which we obtained via an approximation method in Section 2.2.5). We non-dimensionalised the conservation of energy PDE in Section 2.2.6, and the system was defined in terms of five dimensionless parameters, two of these parameters: β_0 , and β_1 describe the heat source term, γ describes the relative magnitude of diffusion relative to convection, \hat{T} describes the relative magnitude of newton cooling to the heat source, and Nu describes the ratio of convective to conductive heat transfer on the upper panel.

We applied parameter values to the system in Section 2.2.7, these parameter values were from Tyagi et al. [63] and Cregan and Myers [10].

We obtained a solution for the temperature in the system by applying a separation of variables method to the conservation of energy PDE. In Section 2.2.9, we define a collector efficiency, in doing so, we redefined the standard efficiency definition such that it now extends to a collector with an isothermal base panel. We plotted and discussed various parameter configurations and how they affect collector efficiency in Section 2.2.10. Figure 2.8 showed how the collector's temperature in the cross section varies at different positions along the receiver. Figure 2.9 highlighted the difference between Cregan and Myers' [10] plug flow model, and this depth-dependent model; the plug flow method overestimated collector efficiency by roughly 1% across all of the channel depths explored. Figure 2.10 showed how the efficiency of the collector increased with increasing nanofluid particle volume fraction before plateauing at 81.2% under the system parameters.

While this collector is quite efficient, it does not produce a substantial temperature increase between the inlet and the outlet, and so its utility in real-world applications is rather limited. In the succeeding chapters, we explore and discuss alternative collector designs with more real-world applications.

CHAPTER 3

COLLECTOR 2: A PARALLEL-PLATE NDASC WITH REFLECTIVE BASE PANEL

3.1 Introduction

In this chapter we model a low-profile NDASC consisting of nanofluid flowing between parallel plates on an inclined plane under a laminar flow regime; however, unlike Collector 1, this collector—Collector 2—has a reflective base panel. Figure 3.1 depicts the general layout of Collector 2; in this design, incoming solar radiation is absorbed as it propagates in through the system and also back out of the system after it is reflected by the base panel. The model proposed in this chapter is similar to Collector 1’s model; however, there are modifications that account for the reflected radiation.

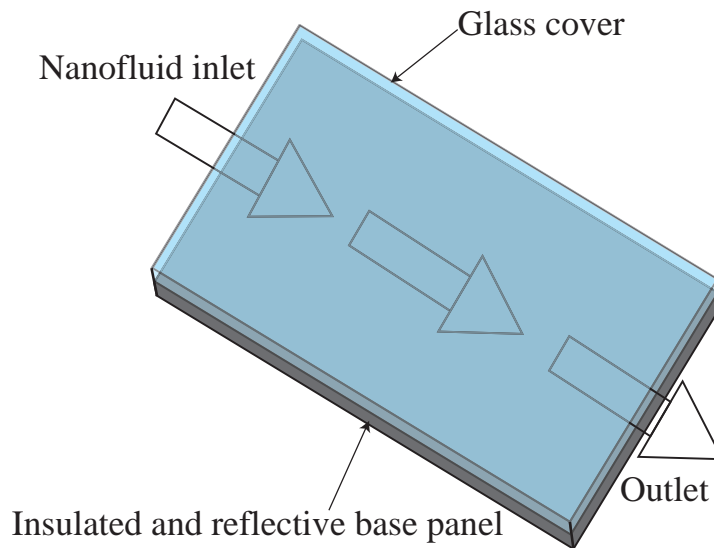


Figure 3.1: General design of Collector 2.

Otanicar et al. [48] use a reflective surface to coat the bottom of an NDASC and numerically and experimentally test the collector performance; in this chapter we model the same type of NDASC. A two-dimensional representation of Otanicar et al.'s [48] experimental setup is detailed in Figure 3.2. NDASC efficiency is very much dependent on receiver height, Otanicar et al. report relatively high collector efficiencies with a small collector height ($H = 0.00015$ m). While Collector 2 is only a slight modification to Collector 1, existing models for NDASCs are either solved numerically, or they fail to include a depth dependent velocity profile and the reflective base panel. Cregan and Myers [10] reproduce Otanicar et al.'s [48] results analytically; however, they achieve this by setting an unrealistic reflectance of the glass panel at the top of their solar collector ($\Upsilon_T = 0.65$), and using a much larger receiver height ($H = 0.0012$ m). In this chapter we propose a new model for an NDASC flowing through parallel plates where the base panel is reflective.

In Section 3.2.2 we present a two-dimensional model for the conservation of energy in a parallel-plate NDASC under laminar flow. In this system, the base panel of the collector is coated with aluminium foil which reflects incoming radiation back out of the receiver; therefore, in Section 3.2.4, we introduce a term describing the source of heat which accounts for reflected radiation. While NDASCs are designed to absorb sunlight, sometimes they are tested using heat lamps to generate incoming radiation. Heat lamps can produce a constant and predictable source of radiation making them ideal for testing solar collectors in

controlled environments. Therefore, it is important to better understand how the optical properties of nanofluids change with different sources of radiation. In Section 3.2.6, we propose a case study to consider two alternative sources of Black-body radiation; the first is a heat lamp at 3158 K, and the second is the sun at 5800 K. In Section 3.2.6 we apply the realistic parameter values to the model and discuss the collector performance further in Section 3.2.8.

3.2 Model

3.2.1 Introduction

We model Collector 2 as a two-dimensional channel on an inclined plane at an angle of θ to the horizontal, see Figure 3.2 for an illustrated schematic of the system. Conveniently, the system geometry used to model this collector is the same as the one used to model Collector 1. Recall, x^* is the coordinate in the downstream direction and z^* is the perpendicular distance downwards from the upper surface (* denotes a dimensional variable). The underside of the collector ($z^* = H$) is completely insulated and so heat is lost due to Newton cooling at the upper panel ($z^* = 0$). The temperature of the surrounding air, T_A^* , remains constant; also, the nanofluid enters the collector with initial temperature T_I^* , and heats up as it absorbs solar radiation volumetrically.

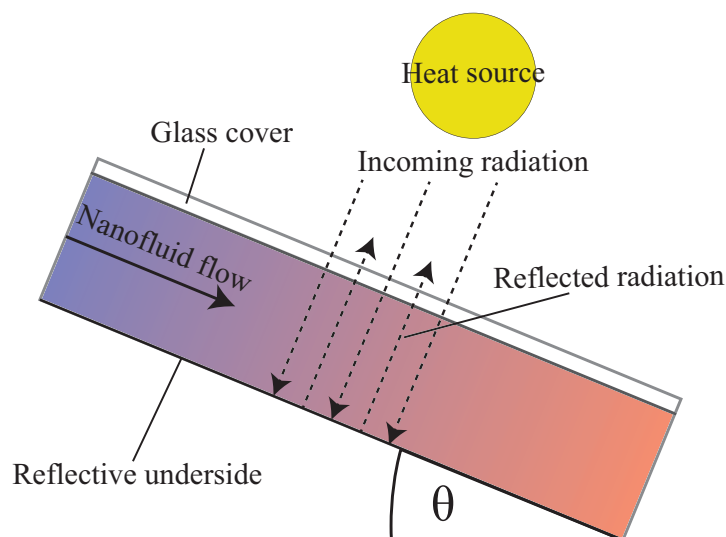


Figure 3.2: Nanofluid flow through a channel with a glass cover and a reflective underside.

3.2.2 Conservation of Energy

The conservation of energy in this system is similar to the conservation of energy for Collector 1, (which is described in (2.2.2)) with one key difference—the volumetric heat source term, q , is altered to more accurately model a collector with a reflective underside. Therefore, conservation of energy when this collector is at a steady-state is given by

$$\rho_{nf} c_{p,nf} \mathbf{u} \cdot \nabla T^* = k_{nf} \nabla^2 T^* + q. \quad (3.2.1)$$

There is a zero flux boundary condition at $z^* = H$ due to the underside of the collector being insulated, and a newton cooling (or heating) boundary condition at $z^* = 0$, the top of the collector. More explicitly these boundary conditions are

$$\left. \frac{\partial T^*}{\partial z^*} \right|_{z^*=H} = 0, \quad k_{nf} \left. \frac{\partial T^*}{\partial z^*} \right|_{z^*=0} = h_s \left(T^* \Big|_{z^*=0} - T_{Amb}^* \right). \quad (3.2.2)$$

The nanofluid enters the system at a constant temperature so $T^*(x^* = 0, z^*) = T_I^*$, also, the outlet condition is $T_{x^*}^*(x^* = L, z^*) = 0$.

3.2.3 Conservation of momentum

Conservation of momentum is expressed via the steady-state Navier-Stokes equations for laminar, incompressible fluid flow down an inclined plane under the action of gravity

$$(\mathbf{u} \cdot \nabla) \mathbf{u} + \frac{1}{\rho_{nf}} \nabla p^* - \frac{\mu_{nf}}{\rho_{nf}} \nabla^2 \mathbf{u} = \mathbf{g}, \quad (3.2.3)$$

and, following the method detailed in Section 2.2.4, we use (3.2.3) to obtain the velocity in the system:

$$u^*(z^*) = \frac{\rho_{nf} g H^2 \sin \theta}{2\mu_{nf}} \left(\frac{z^*}{H} - \frac{z^{*2}}{H^2} \right). \quad (3.2.4)$$

3.2.4 Heat source

Otanicar et al. [48] model a flat plate NDASC with a highly reflective bottom surface. In their system, incoming radiation is reflected back at the bottom of the collector and so they also split up the solar intensity into its incoming and outgoing directional components. We follow the approach taken by Otanicar et al. [48] and assume that the incoming radiation is reflected back off the aluminium

tape in the direction that is normal to the receiver. The change in normally incident solar spectral flux due to attenuation of the nanofluid is dissipated as heat release. Mathematically, it is given by

$$\frac{dJ_{A\lambda}^*}{dz^*} = -K_e J_{A\lambda}^*, \quad \frac{dJ_{B\lambda}^*}{dz^*} = K_e J_{B\lambda}^*, \quad (3.2.5)$$

where the subscripts A and B denote the incoming and outgoing directional components respectively. This system has solutions of the form

$$J_{A\lambda}^* = C_1 e^{-K_e z^*}, \quad J_{B\lambda}^* = C_2 e^{K_e z^*}, \quad (3.2.6)$$

where the integration constants C_1 , and C_2 are obtained after applying the boundary conditions

$$J_{A\lambda}^*(z^* = 0) = J_0, \quad J_{A\lambda}^*(z^* = H) = J_{B\lambda}^*(z^* = H), \quad (3.2.7)$$

and so

$$C_1 = J_0, \quad C_2 = J_0 e^{-K_e H}. \quad (3.2.8)$$

Using these constants, the spectral intensities are

$$J_{A\lambda}^*(z^*) = J_0 e^{-K_e z^*}, \quad J_{B\lambda}^*(z^*) = J_0 e^{-K_e H} e^{K_e z^*}. \quad (3.2.9)$$

Next, we integrate (3.2.9) over the entire wavelength spectrum to determine the corresponding radiative fluxes,

$$P_A^*(z^*) = \int_0^\infty J_0 e^{-K_e z^*} d\lambda, \quad P_B^*(z^*) = \int_0^\infty J_0 e^{-K_e H} e^{K_e z^*} d\lambda. \quad (3.2.10)$$

The equations in (3.2.10) are highly nonlinear with respect to wavelength. To make analytic progress we follow the approach of Cregan and Myers [10] which is detailed in Section 2.2.5. Recall from Section 2.2.5 that the radial flux is approximated via a power law decay of the form

$$\int_0^\infty J_{0,\lambda} e^{-K_e z^*} d\lambda \approx \frac{G_s^*}{\left(1 + \frac{\beta_0}{H} z^*\right)^{\beta_1}}, \quad (3.2.11)$$

3. COLLECTOR 2: A PARALLEL-PLATE NDASC WITH REFLECTIVE BASE PANEL

where β_0 , and β_1 are fitting parameters. Similarly, in this section we use (3.2.11) to approximate (3.2.10) and obtain

$$P_A^*(z^*) = \frac{G_s^*}{\left(1 + \frac{\beta_0}{H} z^*\right)^{\beta_1}}, \quad P_B^*(z^*) = \frac{G_s^*}{\left(1 + \frac{\beta_0}{H} (2H - z^*)\right)^{\beta_1}}. \quad (3.2.12)$$

The qualitative behaviours of P_A^* and P_B^* are understood with the aid of Figure 3.3. We observe that P_A^* decreases as z^* increases, this is because incoming radiation enters the receiver at $z^* = 0$ and is attenuated due to the scattering and absorption as it passes through the receiver. Meanwhile, P_B^* decreases as z^* decreases because at $z^* = H$ the solar radiation is reflected and continues to get attenuated until it exits the receiver at $z^* = 0$. As f_v increases, the incoming and outgoing radiative fluxes are attenuated more quickly. Only 15% of the incoming radiation is absorbed by the pure basefluid ($f_v = 0$), while the nanofluid with $f_v = 0.006$ absorbs 96% of the incoming radiation. We note that 100% of the incoming solar radiation at $z^* = H$ is reflected back out of the collector in order to generate Figure 3.3; however, most surfaces are not perfect reflectors so we introduce R_A , the reflectivity of the base panel. For example, an aluminum base panel has $R_A = 0.73$ and so it only reflects 73% of the incoming radiation [23].

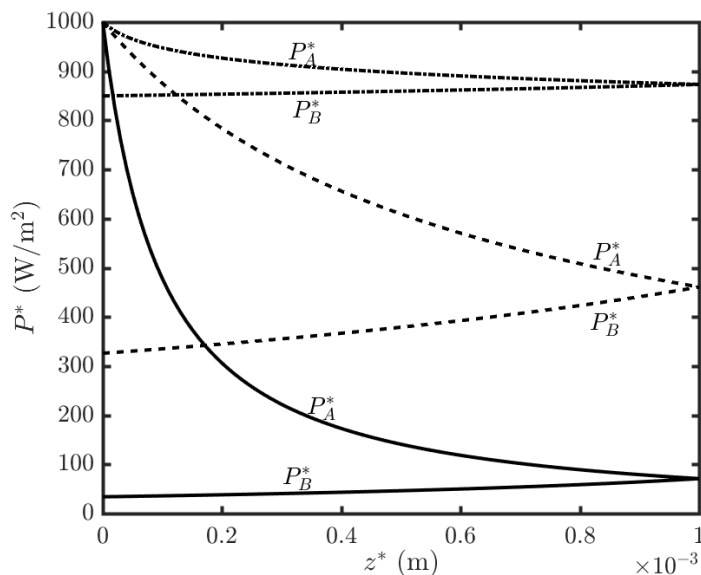


Figure 3.3: The solar intensities, $P_A^*(z^*)$, and $P_B^*(z^*)$ in the collector for $f_v = 0.006$ (solid lines), $f_v = 0.0005$ (dashed lines), and $f_v = 0$ (dot-dashed lines). The nanofluid is Water/Aluminium, $H = 0.001$ m, and $G_s^* = 1000$ Wm^{-2} .

The solar intensities given by (3.2.12) are differentiated to obtain the heat source term:

$$q^*(z^*) = \left(-\frac{dP_A^*}{dz^*} + \frac{dP_B^*}{dz^*} \right) \quad (3.2.13)$$

$$= \left(\frac{G_s^* \beta_0 \beta_1}{H \left(1 + \frac{\beta_0}{H} z^*\right)^{\beta_1+1}} + R_A \frac{G_s^* \beta_0 \beta_1}{H \left(1 + \frac{\beta_0}{H} (2H - z^*)\right)^{\beta_1+1}} \right). \quad (3.2.14)$$

3.2.5 Dimensional analysis

We rewrite the conservation of energy in the system using the velocity profile, (3.2.4), and the heat source term, (3.2.14), to obtain

$$\frac{c_{p,nf} \rho_{nf}^2 g \sin \theta}{2\mu_{nf}} (Hz^* - z^{*2}) \frac{\partial T^*}{\partial x^*} = k_{nf} \left(\frac{\partial^2 T^*}{\partial z^{*2}} + \frac{\partial^2 T^*}{\partial x^{*2}} \right) + \Upsilon_T \left(\frac{G_s^* \beta_0 \beta_1}{H \left(1 + \frac{\beta_0}{H} z^*\right)^{\beta_1+1}} + R_A \frac{G_s^* \beta_0 \beta_1}{H \left(1 + \frac{\beta_0}{H} (2H - z^*)\right)^{\beta_1+1}} \right), \quad (3.2.15)$$

with the boundary conditions

$$\left. \frac{\partial T^*}{\partial z^*} \right|_{z^*=H} = 0, \quad \text{and} \quad k_{nf} \left. \frac{\partial T^*}{\partial z^*} \right|_{z^*=0} = h_s \left(T^* \Big|_{z^*=0} - T_{Amb}^* \right). \quad (3.2.16)$$

For consistency, we rescale and non-dimensionalise (3.2.15) choosing the same dimensionless parameters that were used to rescale (2.2.23) in the model that describes Collector 1. Therefore, (3.2.15)—in dimensionless form—is

$$(z - z^2) \frac{\partial T}{\partial x} = \gamma \frac{\partial^2 T}{\partial z^2} + \frac{1}{\text{Pe}} \frac{\partial^2 T}{\partial x^2} + \frac{1}{(1 + \beta_0 z)^{\beta_1+1}} + \frac{R_A}{(1 + \beta_0(2 - z))^{\beta_1+1}}, \quad (3.2.17)$$

a second order inhomogeneous partial differential equation with an initial condition $T(x=0) = 0$, outlet condition $T_x(x=L) = 0$ and the boundary conditions

$$\left. \frac{\partial T}{\partial z} \right|_{z=1} = 0, \quad \text{and} \quad \left. \frac{\partial T}{\partial z} \right|_{z=0} = \text{Nu} \left(T \Big|_{z=0} - \hat{T} \right). \quad (3.2.18)$$

Recall from the last chapter how since $1/\text{Pe} \ll 1$, one can ignore the boundary layer at $x^* = L$, and approximate (3.2.18) with

$$(z - z^2) \frac{\partial T}{\partial x} = \gamma \frac{\partial^2 T}{\partial z^2} + \frac{1}{(1 + \beta_0 z)^{\beta_1+1}} + \frac{R_A}{(1 + \beta_0(2 - z))^{\beta_1+1}}, \quad (3.2.19)$$

3. COLLECTOR 2: A PARALLEL-PLATE NDASC WITH REFLECTIVE BASE PANEL

and drop the boundary condition at the outlet.

3.2.6 Case study

As a case study for exploring this model further, we apply the parameter values used by Otanicar et al. [48]; these parameter values are detailed in Table 3.1.

Quantity	Symbol	Value	Units
Collector length/width/height	$L/W/H$	1, 1, 0.00015	m
Average velocity downstream	\bar{u}	0.0259 m s ⁻¹	-
Viscosity (H ₂ O)	μ_{bf}	10 ⁻³	kg m ⁻¹ s ⁻¹
Surface heat transfer coefficient	h_s	23	W m ⁻² K ⁻¹
Air/inlet nanofluid temperature	T_{Amb}^*/T_I^*	298.15/308.15	K
Incident solar radiation	G_S	1000	W m ⁻²
Gravity	g	9.8	m s ⁻²
Density water/aluminium	ρ_{bf}/ρ_{np}	1000/2700	kg m ⁻³
Conductivity water/aluminium	k_{bf}/k_{np}	0.609/247	W m ⁻¹ K ⁻¹
Specific heat capacity water/aluminium	$c_{p,bf}/c_{p,np}$	4187/900	J kg ⁻¹ K ⁻¹
Fitting parameters (for $\phi = 0.006$)	β_0/β_1	3.4135/0.4014	-
Dimensionless parameters	$\gamma/\text{Nu}/\hat{T}$	12.62 / 0.0056 / 2.63	-

Table 3.1: Solar collector and nanofluid parameters and physical constants from Otanicar et al. [48].

Recall from Chapter 2 where we applied parameter values from Cregan and Myers [10] to explore the model for Collector 1. Some of the key differences between parameter values from Chapter 2's case study and the parameter values from Otanicar et al.'s [48] case study are detailed in Table 3.2; we discuss these parameter values further in Section 3.2.8, highlighting the differences between the two case studies.

	Collector 1	Collector 2
Temperature of source	5800 K	3158 K
Receiver depth	0.0012 m	0.00015 m
Material at $z^* = 0$	Non reflective insulator	Aluminium tape ($R_A = 0.73$ from Janecek [23])
Nanoparticles	Aluminium	Carbon nanotubes, graphite, and silver

Table 3.2: Some key differences between the case study used to explore Collector 1 and the case study used to explore Collector 2.

3.2.7 Solution method

We note the similarities between (3.2.19) from this chapter and (2.2.28) from the previous chapter: they are both second order inhomogeneous partial differential equations (albeit with different source terms). Therefore, we also obtain a solution for T in this chapter via the method of separation of variables. The presence of non-homogeneous terms in the system suggests a solution of the form $T(x, z) = v(x, z) + w(z)$, and we choose $w(z)$ such that

$$\gamma w_{zz} + \frac{1}{(1 + \beta_0 z)^{\beta_1 + 1}} + \frac{R_A}{(1 + \beta_0(2 - z))^{\beta_1 + 1}} = 0, \quad (3.2.20)$$

which has the solution

$$w(z) = \frac{1}{\gamma \beta_1 (\beta_1 - 1) \beta_0^2} \left(\frac{1}{(1 + \beta_0 z)^{\beta_1 - 1}} + \frac{R_A}{(1 + \beta_0(2 - z))^{\beta_1 - 1}} \right) + K_1 z + K_2. \quad (3.2.21)$$

We apply the boundary conditions to (3.2.21) and solve for the integration constants

$$\begin{aligned} K_1 &= \frac{R_A - 1}{\gamma \beta_1 \beta_0 (1 + \beta_0)^{\beta_1}}, \\ K_2 &= \frac{1}{Nu} \left(\frac{1}{\gamma \beta_0 \beta_1} - \frac{R_A}{\gamma \beta_0 \beta_1 (1 + 2\beta_0)^{\beta_1}} + K_1 \right) \\ &\quad + \frac{1}{\gamma \beta_0^2 \beta_1 (\beta_1 - 1)} \left(1 + \frac{R_A}{(1 + 2\beta_0)^{\beta_1 - 1}} \right) + \hat{T}. \end{aligned}$$

We note that, in this case $v(x, z)$ is identical to $v(x, z)$ from Section 2.2.8, and so the temperature of the nanofluid is given by

$$\begin{aligned} T(x, z) &= w(z) + \\ &\sum_{n=1}^{\infty} \left[C_n \exp(-\lambda p_n^2 x) \left[D_\nu \left(\sqrt{2p_n} \left[z - \frac{1}{2} \right] \right) + K_3 D_\nu \left(-\sqrt{2p_n} \left[z - \frac{1}{2} \right] \right) \right] \right]. \end{aligned}$$

The series coefficient C_n is determined after imposing the initial condition, and the constant K_3 is obtained by applying the boundary conditions:

$$K_3 = \frac{\nu D_{\nu-1} \left(\sqrt{\frac{p_n}{2}} \right) - D_{\nu+1} \left(\sqrt{\frac{p_n}{2}} \right)}{\nu D_{\nu-1} \left(\sqrt{-\frac{p_n}{2}} \right) - D_{\nu+1} \left(-\sqrt{\frac{p_n}{2}} \right)}, \quad (3.2.22)$$

$$C_n = - \frac{\int_0^1 w(z)(z - z^2) [D_\nu (\sqrt{2p_n} [z - \frac{1}{2}]) + K_3 D_\nu (-\sqrt{2p_n} [z - \frac{1}{2}])] dz}{\int_0^1 [D_\nu (\sqrt{2p_n} [z - \frac{1}{2}]) + K_3 D_\nu (-\sqrt{2p_n} [z - \frac{1}{2}])]^2 dz}, \quad (3.2.23)$$

where the eigenvalues, p_n satisfy

$$\begin{aligned} & \left[\nu D_{\nu-1} \left(-\sqrt{\frac{p_n}{2}} \right) - D_{\nu+1} \left(-\sqrt{\frac{p_n}{2}} \right) - K_3 \left[\nu D_{\nu-1} \left(\sqrt{\frac{p_n}{2}} \right) - D_{\nu+1} \left(\sqrt{\frac{p_n}{2}} \right) \right] \right] \\ & = \sqrt{\frac{2Nu^2}{p_n}} \left[D_\nu \left(-\sqrt{\frac{p_n}{2}} \right) + K_3 D_\nu \left(\sqrt{\frac{p_n}{2}} \right) \right]. \end{aligned} \quad (3.2.24)$$

We calculate the efficiency of this collector via the equations outlined in Section 2.2.9; in dimensional notation,

$$\eta = \frac{\rho_{nf} c_{p,nf}}{G_S L} \int_0^H (T_O^*(z^*) - T_I^*) u(z^*) dz^*, \quad (3.2.25)$$

or equivalently in dimensionless notation,

$$\eta = \beta_0 \beta_1 \int_0^1 T_O(z)(z + z^2) dz. \quad (3.2.26)$$

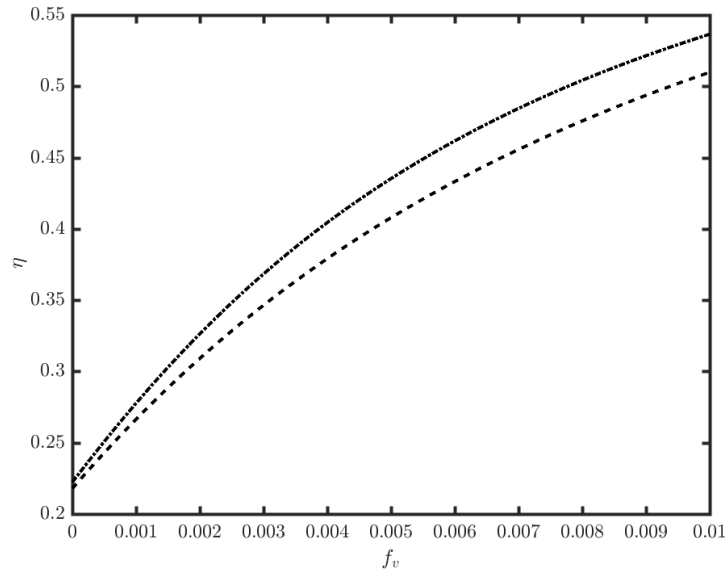
3.2.8 Results

Although the case study in this chapter closely resembles the case study that is explored in Otanicar et al. [48], the nanoparticles used in this chapter differ to the nanoparticles used in that study. Therefore, both nanofluids have different extinction coefficients, and we cannot do a like-for-like comparison between these two studies. Nonetheless, in this section we do make several indirect comparisons between Otanicar et al.'s [48] research and the work in this chapter.

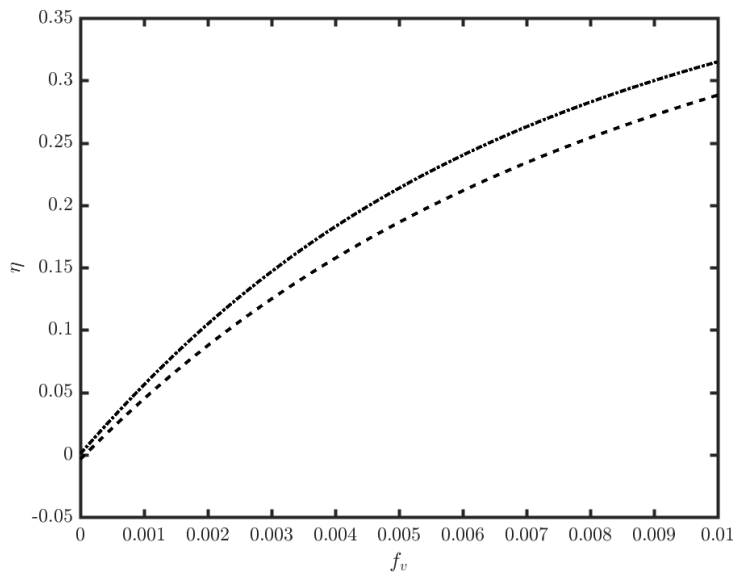
Figure 3.4 shows collector efficiency versus particle volume fraction across two different inlet temperatures for an NDASC with a reflective base panel (dashed

lines) and an NDASC without a reflective base panel (dot-dashed lines). The nanofluid heats up as it absorbs the incoming radiation ($P_A^*(z^*)$); this incoming radiation is reflected back out at $z^* = H$ and so the nanofluid also absorbs outgoing radiation, $P_B^*(z^*)$, thus, heating up further. Therefore, an NDASC coated with a reflective base panel absorbs more radiation than an uncoated NDASC. In Figure 3.4 the coated NDASC performs better than the uncoated NDASC under all circumstances due to this increased amount of absorbed radiation. Both collectors perform similarly when $f_v = 0$ and little incoming radiation is absorbed; however, the performance differences between the two collectors become more pronounced as the nanofluid's particle volume fractions are increased—the efficiency of Collector 2 rises faster than the efficiency of Collector 1. In Figure 3.4a, when $T_A^* = T_I^*$, both NDASCs are more efficient than in Figure 3.4b when $T_A^* = T_I^* - 10$ °C; as the temperature of the nanofluid in the system increases, more energy is lost via Newton cooling at $z^* = 0$ and this decreases collector performance.

3. COLLECTOR 2: A PARALLEL-PLATE NDASC WITH REFLECTIVE BASE PANEL



(a)



(b)

Figure 3.4: Efficiency versus particle volume fraction for Collector 1 (dot-dashed line), and Collector 2 (dashed line), (a) $T_I = T_{Amb}$, and (b) $T_I = T_{Amb} + 10 \text{ }^\circ\text{C}$.

Figure 3.5 shows the outlet temperature versus receiver depth for Collector 1, an NDASC without a reflective base panel (dot-dashed line), and Collector 2, an NDASC with a reflective base panel (dashed line), when $T_I^* = 25 \text{ }^\circ\text{C}$,

$f_v = 0.01$, and $\Upsilon_T = 1$. The nanofluid is hotter at the outlet of Collector 2, than at the outlet of Collector 1 because Collector 2 absorbs more radiation. The temperature profile of the nanofluid as it flows through the receiver does not vary much with receiver depth because heat is diffused in the z^* -dimension at a much faster rate than it is absorbed volumetrically. Since the depth of the receiver is so small ($H = 0.00015$ m), $\gamma = 12.96$, and the diffusion term dominates the model in (3.2.19). If the receiver depth was larger, γ would be smaller and we would observe larger gradients in the temperature profile at the outlet.

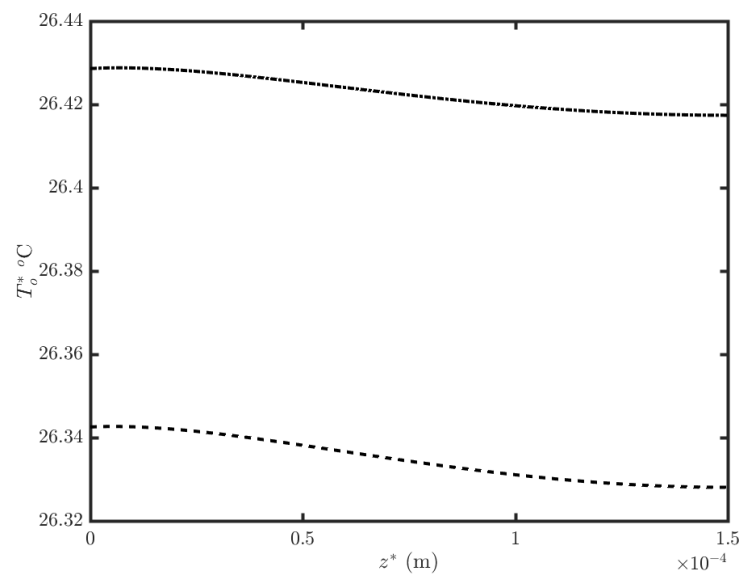


Figure 3.5: Temperature at the outlet versus receiver depth for Collector 1 (dot-dashed line), and Collector 2 (dashed line).

We use Planck’s Black-body relation, (2.2.16), to calculate the spectral intensity of the incoming electromagnetic radiation. The spectral intensity is highly dependent on the temperature of the source. Sunlight was the source of incoming radiation in the case study used to explore Collector 1; however, in this case study we follow Otanicar et al.’s experimental trials and use a heat lamp at 3158 K as the source of incoming radiation [48]. We note that the surface of the sun, at 5800 K, is much hotter than the heat lamp used in Otanicar et al.’s experimental trials; Figure 3.6 illustrates the spectral distribution of Planck’s Black-body relation for two objects, one at the temperature of the sun, and the other at the temperature of the heat lamp. While the spectral intensities have been scaled

3. COLLECTOR 2: A PARALLEL-PLATE NDASC WITH REFLECTIVE BASE PANEL

such that the area under both curves is 1000 w/m^2 ; the radiative intensities are distributed differently across the electromagnetic spectrum. The radiation emitted from the heat lamp is noticeably more intense at longer wavelengths and less intense at shorter wavelengths.

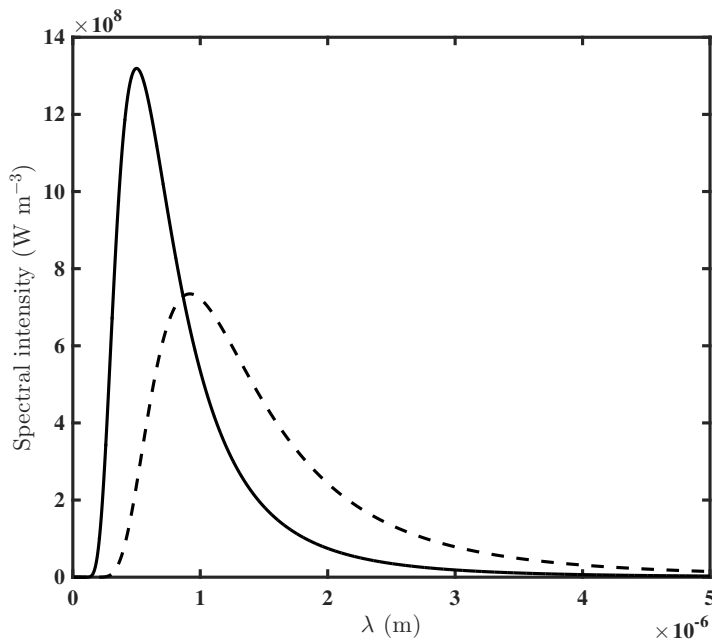


Figure 3.6: Spectral dependence of Black-body radiation for two bodies at 5800 K and 3158 K.

The qualitative performance of an NDASC depends on the spectral power distribution of the incoming radiation and so it is important to consider this phenomenon when designing and testing NDASCs. Figure 2.5 shows how water is better at absorbing radiation at longer wavelengths; therefore, one might expect the water-based NDASC to always perform better when incoming radiation comes from the heat lamp rather than from the sun. However, we observe in Figure 3.7 that this is not always the case. When $f_v = 0$, Collector 2 is more efficient when the incoming radiation is emitted by the heat lamp; however, when $f_v = 0.01$, Collector 2 is more efficient when the incoming radiation is emitted by the sun. This is because the water is better at absorbing the heat lamp generated radiation, but the aluminium nanoparticles are better at absorbing solar radiation. As the nanoparticle volume fraction in the nanofluid increases, the efficiency of the

sunlight-absorbing NDASC increases faster than the efficiency of the NDASC which is absorbing radiation from the heat lamp.

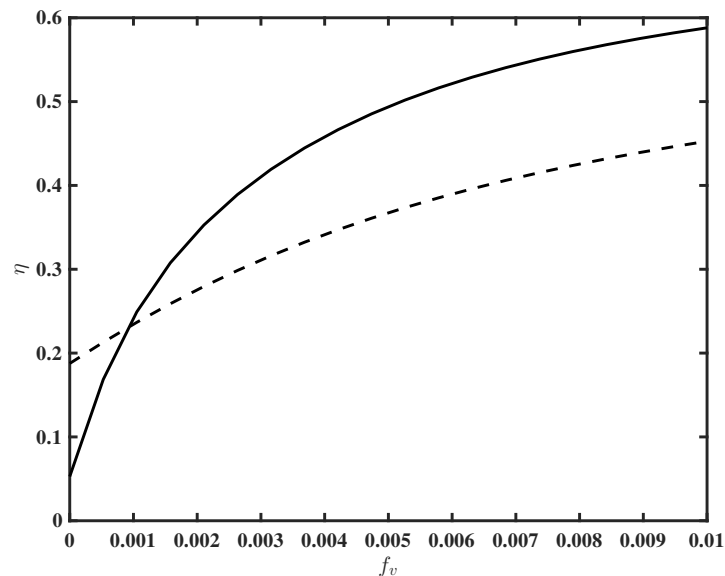


Figure 3.7: Efficiency of the solar collector versus nanofluid particle fraction. The source of radiation is a Black-body at 5800 K (solid line) 3158 K (dashed line).

Figure 3.8 shows the efficiency of the solar collector versus particle volume fraction for $H = 0.0006$ (solid line), $H = 0.0012$ (dashed line), and $H = 0.0018$ (dot-dashed line) using parameter values from the case-study detailed in Table 2.1. This plot demonstrates Collector 2's performance when its parameter values are equivalent to the ones that produced the optimal efficiency of Collector 1 (81.2%); we note that Figure 3.8 is directly comparable to Figure 2.10. In Figure 3.8 we observe a sharp increase in collector efficiency across each of the three height configurations when nanoparticles are first added to the base fluid and particle volume fractions are quite low. The presence of nanoparticles increases the rate at which incoming radiation is absorbed into the working fluid. However, as the nanoparticle volume fraction continues to rise, we observe different qualitative behaviours in all three of the collector configurations. This initial increase is sharpest at larger collector depths and is progressively more gradual as the collector depth decreases. The efficiencies of all three collector configurations plateau with further increase in f_v ; after the system has absorbed all of the available incoming radiation any additional increase in particle volume fraction does

not lead to any further efficiency enhancement. We note that there are subtle differences between Figures 2.10 and 3.8; in Figure 3.8, the maximum efficiency value is (81.3%), and so Collector 2 performs marginally better than Collector 1. Furthermore, the efficiency of Collector 2 plateaus at lower particle volume fractions across all three heights than the efficiency of Collector 1—the reflective base-panel is always increases efficiency across all of the operating conditions.

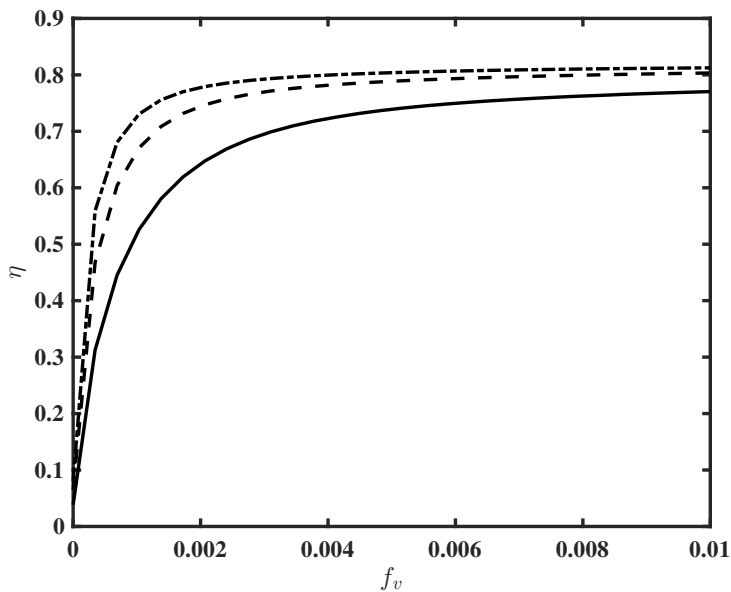


Figure 3.8: Efficiency of the solar collector versus particle volume fraction for $H = 0.0006$ (solid line), $H = 0.0012$ (dashed line), and $H = 0.0018$ (dot-dashed line).

3.3 Summary and discussion

In this chapter we modelled the efficiency of a parallel plate NDASC on an inclined plane with a reflective base panel. This type of collector has been studied experimentally and modelled numerically; however, this particular system configuration has not been studied analytically. The modelling approach taken in this chapter closely followed the modelling methodology outlined in Chapter 2. These first two models have many similarities: the system geometries are defined using the same coordinate system, conservation of momentum takes the same form, the thermophysical properties of the nanofluid are calculated using the same method,

and there are various other system parallels. However, there are also some fundamental differences between Collectors 1 and 2. One major difference is the heat source term; in Section 3.2.4 we showed how the reflective base panel alters the form of the radiative flux integral and thus the PDE describing the conservation of energy. Other significant differences between the two collectors are highlighted in Table 3.2 from Section 3.2.6, where we detailed the parameter values used in this chapter's case study. Following dimensionless analysis, we observed that $\gamma \sim O(10)$ and so diffusion has much more relative importance in this system than in Collector 1. The dimensionless conservation of energy PDE describing this collector was solved via a separation of variables; the homogeneous component of this solution was equivalent to the homogeneous solution from Chapter 2. Meanwhile, the inhomogeneous part of the solution was new, and we outlined its solution method in Section 3.2.7.

We plotted and discussed various parameter configurations and how they affect collector efficiency in Section 3.2.8. Figure 3.4 shows that the reflective base panel does indeed improve collector efficiency, as does nanoparticle volume fraction. The efficiency in this figure reaches 54% and does not plateau like the efficiency in Figure 2.10 from Chapter 2 because the channel much more shallow. We compared the efficiencies of Collectors 1 and 2 in Figure 3.8, showing that Collector 2 can reach efficiency values of up to 81.3% when its channel height was comparable to the channel height which produced Collector 1's optimal performance. At lower channel heights the distinction between the efficiencies of Collectors 1 and 2 became more pronounced, Collector 2 was universally more efficient. In Figure 3.5 we highlighted the difference that a reflective base panel makes to the temperature at the outlet, we also noted that even though this collector has lower efficiencies than Collector 1, it has a higher temperature at the outlet due to its decreased cross-sectional area—although this system does not absorb as much of the incoming radiation, there is a lower volume of nanofluid to heat and so the overall temperature rise across the system is greater. Figure 3.7 shows how the temperature of the heat source significantly affects collector efficiency, this is important to note as it suggests that NDASCs will perform differently when they are in some testing environments than they will in exposure to real sunlight.

The reflective base panel certainly improves collector performance over the non-reflective base panel, and the temperature at the outlet improves with de-

3. COLLECTOR 2: A PARALLEL-PLATE NDASC WITH REFLECTIVE BASE PANEL

creasing channel height; however, at higher operating temperatures this solar collector becomes less efficient, and the temperature rise across the system is still too low for most real-world applications. In the following chapters, we discuss alternative receiver geometries and propose new collector designs with an aim to increase the viability of NDASCs in real-world settings.

CHAPTER 4

COLLECTOR 3: A NON-CONCENTRATING CYLINDRICAL NDASC

4.1 Introduction

This chapter discusses a novel NDASC design. In most non-concentrating NDASCs the nanofluid flows between parallel plates [10, 36, 48, 62, 63]; however, the third collector modelled in this thesis, ‘Collector 3’, is an alternative to the parallel plate design wherein the nanofluid flows through a series of optically transparent pipes. Figure 4.1 illustrates a basic example of Collector 3’s design. The model for this collector requires several fundamental changes to the models describing Collectors 1 and 2; most notably, Collector 3’s model (which is expressed in a three-dimensional cylindrical coordinate system) requires a numerical solution rather than an analytic solution due to its complexity.

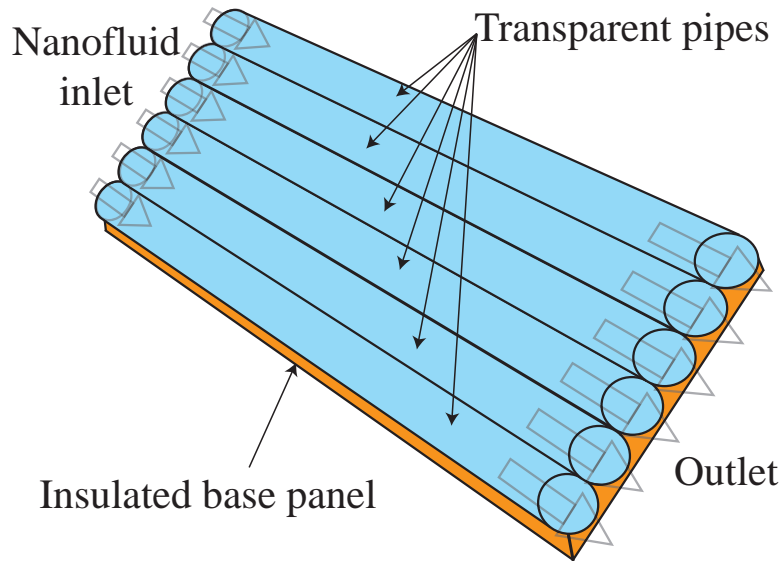


Figure 4.1: General design of Collector 3.

The system's three-dimensional cylindrical coordinate geometry is defined in Section 4.2.1. In Section 4.2.2 we model the conservation of energy, this conservation equation requires us to obtain a fluid velocity profile and a heat source term. We use the steady-state Navier-Stokes equations for laminar, incompressible fluid flow down an inclined pipe under the action of gravity in Section 4.2.3 to find the velocity profile of the nanofluid as it flows through the collector. The nanofluid heats up as it absorbs incoming radiation; in Section 4.2.4 we propose a novel analytic expression describing this heat source. We use these heat source and velocity expressions to fully express the conservation of energy before rescaling and non-dimensionalising the model in Section 4.2.5. Parameter values are applied to this dimensionless model using a hypothetical, but realistic, case study in Section 4.2.6. In Section 4.2.7 we discuss the Crank-Nicolson scheme that is applied to the model in order to obtain a numerical expression for temperature; this temperature is then used to discuss the performance of Collector 3 in Sections 4.2.8 and 4.3.

4.2 Model

4.2.1 Introduction

Figure 4.2 shows a schematic representing the layout of this system. The nanofluid is confined within a cylindrical pipe of radius R and length L ; this pipe has an optically transparent surface (such as glass) and thus permits the majority of the incident solar flux to pass into the nanofluid. The variables x^* , r^* , and ϕ define a three-dimensional cylindrical coordinate system such that x^* is the axial coordinate and it ranges from $x^* = 0$ (the inlet) to $x^* = L$ (the outlet), r^* is the radial dimension and it ranges from the $r^* = 0$ (the centre axis) to $r^* = R$, (the surface). Again, the $*$ notation here denotes dimensional variables. The third coordinate, ϕ , measures the azimuthal angle where $\phi \in [0, \pi]$. Incoming solar radiation is absorbed as it propagates through the collector leading to heat generation in the nanofluid. Newton cooling/heating takes place at the upper surface (when $r^* = R$ and $\phi \leq \pi/2$) and this is modelled using a surface heat transfer coefficient. Meanwhile, the underside of the collector is insulated and so there is zero heat flux when $r^* = R$ and $\phi > \pi/2$.

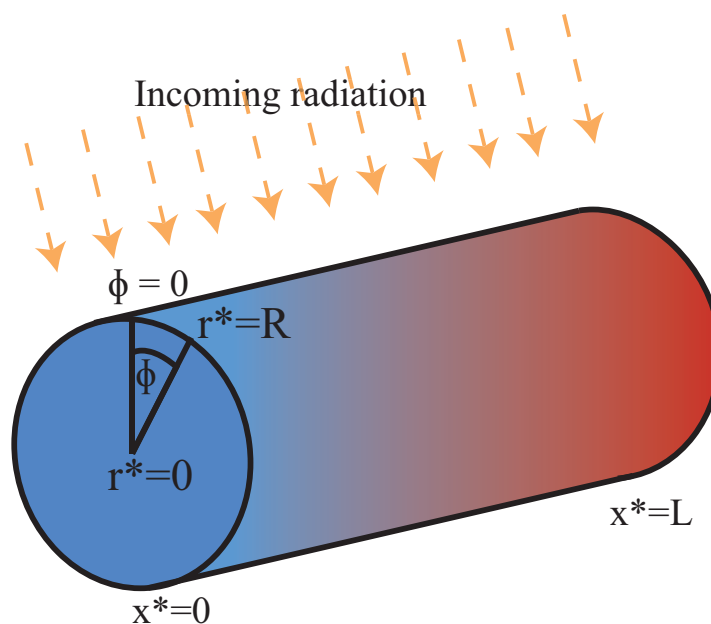


Figure 4.2: Schematic of the cylindrical coordinates and how they represent this problem.

4.2.2 Conservation of energy

The steady-state equation describing the conservation of energy in this collector is

$$\rho_{nf} c_{p,nf} \mathbf{u} \cdot \nabla T^* = k_{nf} \nabla^2 T^* + q, \quad (4.2.1)$$

where $\mathbf{u} = (u^*, v^*, w^*)$ is the velocity field. As mentioned, heat loss takes place via Newton cooling at the top surface of the collector and the underside of the collector is insulated; therefore, we apply the discontinuous boundary condition

$$k_{nf} \frac{\partial T^*}{\partial r^*} \Big|_{r^*=R} = (1 - H(\phi - \pi/2)) h_s \left(T^* \Big|_{r^*=R} - T_{Amb}^* \right), \quad (4.2.2)$$

where $H(\cdot)$ is the Heaviside step function. Also, the nanofluid enters the collector at constant inlet temperature T_I^* , while the outlet condition is $T_x^*(x^* = L) = 0$. This system is symmetric, and the symmetry expressed via the boundary condition

$$\frac{\partial T^*}{\partial \phi} \Big|_{\phi=0,\pi} = 0. \quad (4.2.3)$$

4.2.3 Conservation of momentum

Flow in the receiver is laminar, Newtonian, and steady. The incompressible continuity equation in cylindrical coordinates is

$$\frac{\partial u^*}{\partial x^*} + \frac{1}{r^*} \frac{\partial (r^* v^*)}{\partial r^*} + \frac{1}{r^*} \frac{\partial w^*}{\partial \phi} = 0, \quad (4.2.4)$$

however, since the velocity field is axisymmetric and there is parallel flow, (4.2.4) can be reduced to

$$\frac{\partial u^*}{\partial x^*} = 0, \quad (4.2.5)$$

and so u^* is constant across all values of x^* . At the surface of the receiver there is a no-slip condition, i.e., $\mathbf{u} = 0$ when $r^* = R$. The steady-state momentum equation is

$$-\rho_{nf} g \sin \theta = \frac{\mu}{r^*} \frac{\partial}{\partial r^*} \left(r^* \frac{\partial u^*}{\partial r^*} \right), \quad (4.2.6)$$

which has the solution

$$u^*(r^*) = -r^{*2} \frac{\rho_{nf} g \sin \theta}{4\mu_{nf}} + C_1 \ln r^* + C_2. \quad (4.2.7)$$

The integration constants, C_1 and C_2 , are found by applying the boundary conditions

$$u^*|_R = 0, \quad \left. \frac{du^*}{dr^*} \right|_{r^*=0} = 0, \quad (4.2.8)$$

to (4.2.7), and thus

$$u^*(r^*) = -\frac{\rho_{nf} g \sin \theta}{4\mu_{nf}} (r^{*2} - R^2). \quad (4.2.9)$$

4.2.4 Heat source

Cregan and Myers' [10] heat source approximation method (detailed in Chapters 2 and 3) is expressed in terms of z^* , where z^* is the depth of the nanofluid that solar radiation passes through before reaching a given point in the collector. We obtain an equivalent expression to z^* in this system via the geometrical relation which is illustrated in Figure 4.3:

$$z^* = \sqrt{R^2 - r^{*2} \sin^2(\phi)} - r^* \cos(\phi). \quad (4.2.10)$$

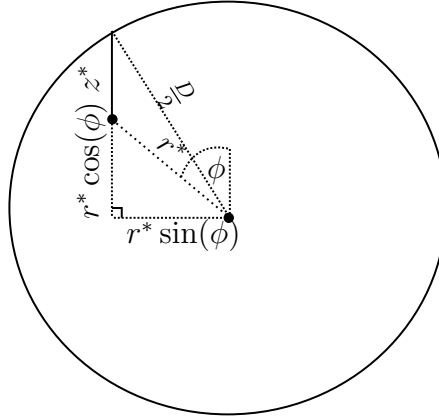


Figure 4.3: Geometry of the source term in cylindrical coordinates.

This result is applied to Cregan and Myers' heat source term [10],

$$q(z^*) = \frac{G_s^* \beta_0 \beta_1}{h [1 + \beta_0 \frac{z^*}{2R}]^{\beta_1 + 1}}, \quad (4.2.11)$$

to obtain Collector 3's heat source term

$$q(r^*, \phi) = \frac{G_s^* \beta_0 \beta_1 (1/R) r^* \cos(\phi)}{2R \left[1 + \beta_0 \frac{\sqrt{R^2 - r^{*2} \sin^2(\phi) - r^* \cos(\phi)}}{2R} \right]^{\beta_1 + 1}}. \quad (4.2.12)$$

Figure 4.4 illustrates how the intensity of the incoming radiation varies across the cross section of the receiver when $f_v = 0$ (i.e. pure water), and $R = 0.0006$. The radiative intensity is greatest at the upper surface of the collector ($r^* = R$ and $\phi = \pi/2$) and it decreases as it is absorbed by the nanofluid while propagating through the collector.

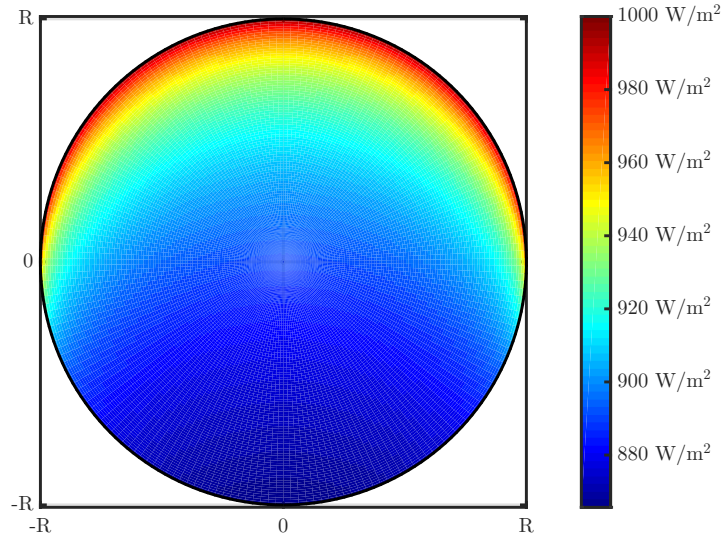


Figure 4.4: Contour plot of the cross sectional radiative intensity in the receiver for $f_v = 0$, and $R = 0.0006$.

4.2.5 Dimensional analysis

The velocity term, (4.2.9), and the heat source term, (4.2.12), are used to fully express the conservation of energy in this system as

$$\rho_{nf} c_{p,nf} u^*(r^*) \frac{\partial T^*}{\partial x^*} = k_{nf} \left[\frac{\partial}{\partial r^*} r^* \frac{\partial T^*}{\partial r^*} + \frac{1}{r^*} \frac{\partial^2 T^*}{\partial \phi^2} + \frac{\partial^2 T^*}{\partial x^{*2}} \right] + q(r^*, \phi), \quad (4.2.13)$$

with boundary conditions

$$k_{nf} \frac{\partial T^*}{\partial r^*} \Big|_{r^*=R} = (1 - H(\phi - \pi/2)) h_s \left(T^* \Big|_{r^*=R} - T_{Amb}^* \right), \quad (4.2.14)$$

$$\frac{\partial T^*}{\partial \phi} \Big|_{\phi=0,\pi} = 0, \quad (4.2.15)$$

This system is non-dimensionalised via the dimensionless parameters

$$r^* = Rr, \quad T^* = T\Delta T + T_I, \quad x^* = Lx, \quad (4.2.16)$$

where ΔT is driven by the source term, i.e.,

$$\Delta T = \frac{2G_s^* L \beta_0 \beta_1 \mu_{nf}}{R^3 c_{p,nf} \rho_{nf}^2 g \sin \theta}. \quad (4.2.17)$$

The dimensionless system is thus:

$$(1 - r^2) \frac{\partial T}{\partial x} = \frac{\gamma}{r} \left[\frac{\partial}{\partial r} r \frac{\partial T}{\partial r} + \frac{1}{r} \frac{\partial^2 T}{\partial \phi^2} \right] + \frac{1}{Pe} \frac{\partial^2 T}{\partial \phi^2} + \frac{r \cos(\phi)}{\left(1 + \frac{\beta_0}{2} \left(\sqrt{1 - r^2 \sin^2(\phi)} - r \cos(\phi) \right) \right)^{\beta_1 + 1}}, \quad (4.2.18)$$

and—similar to previous chapters—we approximate (4.2.18) with

$$(1 - r^2) \frac{\partial T}{\partial x} = \frac{\gamma}{r} \left[\frac{\partial}{\partial r} r \frac{\partial T}{\partial r} + \frac{1}{r} \frac{\partial^2 T}{\partial \phi^2} \right] + \frac{r \cos(\phi)}{\left(1 + \frac{\beta_0}{2} \left(\sqrt{1 - r^2 \sin^2(\phi)} - r \cos(\phi) \right) \right)^{\beta_1 + 1}}, \quad (4.2.19)$$

since, $1/Pe \ll 1$, thus the boundary layer at $x^* = L$ is ignored. This system has

the dimensionless boundary conditions

$$\frac{\partial T}{\partial r} \Big|_{r=1} = (1 - H(\phi - \pi/2)) Nu \left(T \Big|_{r=1} - \hat{T} \right), \quad (4.2.20)$$

$$\frac{\partial T}{\partial \phi} \Big|_{\phi=0,1} = 0, \quad (4.2.21)$$

and the dimensionless inlet condition is $T(x = 0) = 0$. The dimensionless parameters in this system are

$$\hat{T} = \frac{T_{Amb} - T_I}{\Delta T}, \quad \gamma = \frac{3\mu_{nf}k_{nf}L}{c_{p,nf}\rho_{nf}^2gR^4 \sin \theta}, \quad \text{Nu} = \frac{Rh_s}{k_{nf}}, \quad (4.2.22)$$

where \hat{T} is the relative magnitude of the heat loss, γ is the ratio of diffusion to advection, and Nu is the Nusselt number.

4.2.6 Case study

This NDASC design does not appear in the previous literature; so, as a case study for exploring this model further, we propose hypothetical, yet reasonable, physical parameter values which are informed by existing collector designs [10, 48, 63]. We consider an Aluminum/Water nanofluid and, unless otherwise stated, apply the parameter values given in Table 4.1. The spectral-dependent refractive indexes n_{np} and n_{bf} and the nanoparticle absorption index κ_{np}^a are from [47, 51].

Quantity	Symbol	Value	Units
Collector length/width/radius	$L/W/R$	1, 1, 0.0012	m
Collector angle of inclination	θ	$\pi/9$	-
Viscosity (H ₂ O)	μ_{bf}	10^{-3}	kg m ⁻¹ s ⁻¹
Surface heat transfer coefficient	h_s	6.43	W m ⁻² K ⁻¹
Air/inlet temperature	T_{Amb}^*/T_I^*	298.15/308.15	K
Incident solar radiation	G_s^*	1000	W m ⁻²
Gravity	g	9.8	m s ⁻²
Density water/aluminium	ρ_{bf}/ρ_{np}	1000/2700	kg m ⁻³
Conductivity water/aluminium	k_{bf}/k_{np}	0.609/247	W m ⁻¹ K ⁻¹
Specific heat capacity water/aluminium	$c_{p,bf}/c_{p,np}$	4187/900	J kg ⁻¹ K ⁻¹
Fitting parameters (for $\phi = 0.006$)	β_0/β_1	18.75/1.26	-
Dimensionless parameters	$\gamma/\text{Nu}/\hat{T}$	0.059/0.025/6.18	-

Table 4.1: The solar collector and nanofluid's parameters and physical constants for Collector 3.

4.2.7 Solution method

The efficiency of the solar collector, η , is defined as the fraction of ratio of usable thermal energy to incident solar energy, more specifically

$$\eta = \frac{2 \int_0^\pi \int_0^R \rho_{nf} c_{p,nf} r^* u^*(r^*) (T_O^* - T_I^*) dr^* d\phi}{G_{s,a} L 2R}. \quad (4.2.23)$$

This is expressed in dimensionless form

$$\frac{\beta_0 \beta_1}{2} \int_0^\pi \int_0^1 (r - r^3) T_O dr d\phi. \quad (4.2.24)$$

We apply a Crank-Nicolson finite difference scheme to obtain a numerical expression for the temperature of the nanofluid as it flows through the collector. The conservation of energy equations, (4.2.19)-(4.2.21), are expressed in a discrete space, $T_{i,j}^n$, where $i = 1, 2, \dots, I$ is the r component, $j = 1, 2, \dots, J$ is the ϕ component, and $n = 1, 2, \dots, N$ is the x component. Figure 4.5 shows this numerical discretisation of the collector space when $I = 5$, and $J = 7$ (although, we note that this is an extremely coarse mesh; low values for I and J are used purely for clarity in this illustration).

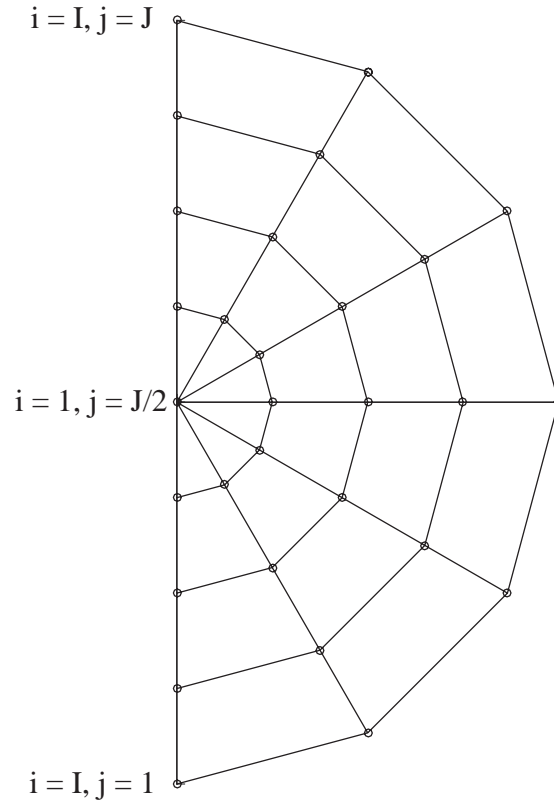


Figure 4.5: Example of mesh used to discretise model where $I = 5$ and $J = 7$.

The discretisation of the PDE (4.2.19) is therefore

$$\begin{aligned}
 \frac{1}{\Delta x} (r_i^2 - r_i^4) (T_{i,j}^{n+1} - T_{i,j}^n) &= \frac{\gamma}{2\Delta r^2} r_i^2 (T_{i+1,j}^{n+1} - 2T_{i,j}^{n+1} + T_{i-1,j}^{n+1} + T_{i+1,j}^n - 2T_{i,j}^n + T_{i-1,j}^n) \\
 &\quad + \frac{\gamma}{4\Delta r} r_i (T_{i+1,j}^{n+1} - T_{i-1,j}^{n+1} + T_{i+1,j}^n - T_{i-1,j}^n) \\
 &\quad + \frac{\gamma}{2\Delta \phi^2} (T_{i,j+1}^{n+1} - 2T_{i,j}^{n+1} + T_{i,j-1}^{n+1} + T_{i,j+1}^n - 2T_{i,j}^n \\
 &\quad \quad \quad + T_{i,j-1}^n) + r_i^2 q_{i,j},
 \end{aligned} \tag{4.2.25}$$

where $i = 2, \dots, I-1$, $j = 2, \dots, J-1$, $n = 2, \dots, N$, and

$$q_{i,j} = \frac{r_i \cos(\phi_j)}{\left(1 + \frac{\beta_0}{2} \left(\sqrt{1 - r_i^2 \sin^2(\phi_j)} - r_i \cos(\phi_j)\right)\right)^{\beta_1+1}}. \tag{4.2.26}$$

The boundary condition at $i = I$, i.e., (4.2.20), is

$$\frac{1}{2\Delta r} (T_{I,j}^{n+1} - T_{I-1,j}^{n+1} + T_{I,j}^n - T_{I-1,j}^n) = (1 - H(\phi_j - \pi/2)) \text{Nu} \left(\frac{T_{I,j}^{n+1} + T_{I,j}^n}{2} - \hat{T} \right), \quad (4.2.27)$$

which holds for $j = 2, \dots, J - 1$, and $n = 2, \dots, N$. Meanwhile, the boundary condition at $i = 1$ is

$$\frac{1}{2} (T_{1,j}^{n+1} + T_{1,j}^n) = \frac{1}{2I} \sum_{i=1}^I (T_{2,j}^{n+1} + T_{2,j}^n), \quad (4.2.28)$$

and, symmetry of the system at $j = 1, J$ is expressed with the boundary conditions

$$\frac{1}{2\Delta\phi} (T_{i,2}^{n+1} - T_{i,1}^{n+1} + T_{i,2}^n - T_{i,1}^n) = 0, \quad (4.2.29)$$

and

$$\frac{1}{2\Delta\phi} (T_{i,J}^{n+1} - T_{i,J-1}^{n+1} + T_{i,J}^n - T_{i,J-1}^n) = 0 \quad (4.2.30)$$

respectively.

4.2.8 Results

Since this collector is a new NDASC design, we are unable to make direct comparisons between the results in this chapter and results from previous literature. Instead, this section discusses Collector 3's performance and how it relates to qualitative phenomena exhibited by collectors in previous studies. Figure 4.6 shows a contour plot of the temperature in the cross section at the outlet for $f_v = 0.006$, and $T_I^* = T_{Amb}^*$. The nanofluid is hottest at the top of the collector and its temperature decreases the closer it is to the bottom of the collector; although, we note that the temperature variation over the entire cross section at the outlet is relatively small, $O(0.3^\circ\text{C})$.

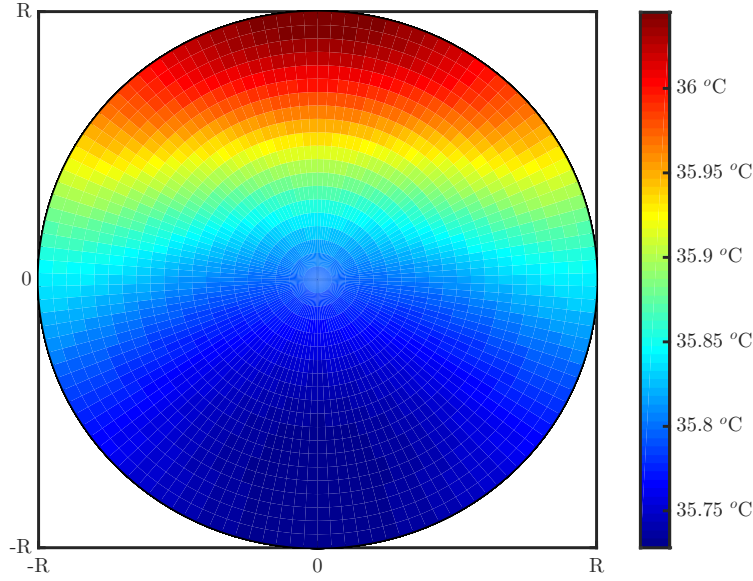


Figure 4.6: Contour plot of the temperature of the nanofluid for $f_v = 0.006$, and $T_I^* = T_{Amb}^*$.

The optimal nanoparticle volume fraction varies across different pipe diameters. Figure 4.7 demonstrates collector efficiency versus particle volume fraction for $R = 0.0006$ (solid line), $R = 0.0012$ (dashed line), and $R = 0.0024$ (dot-dashed line). We observe a sharp increase in collector efficiency across each of the three parameter value configurations when nanoparticles are initially added to the base fluid and particle volume fractions are quite low. The presence of nanoparticles increases the rate at which incoming radiation is absorbed into the working fluid; however, as the nanoparticle volume fraction continues to rise, each of the three parameter configurations perform differently. The efficiency of the collector when $R = 0.0006$ (the smallest system) continues to rise with increasing nanoparticle volume fraction, albeit at a progressively slower rate. The efficiency of the collector when $R = 0.0012$ rises with increasing particle volume fraction until $f_v \approx 0.006$, at which point its efficiency plateaus. As was the case with Collectors 1 and 2, after Collector 3 has absorbed all of the available incoming radiation any additional increase in particle volume fraction does not lead to any further efficiency enhancement. Meanwhile, the efficiency of the collector with $R = 0.0024$ (the largest system) peaks at $f_v \approx 0.0037$, after which point η begins

to decrease as the particle volume fraction increases further. As f_v increases, so too does the extinction coefficient of the nanofluid. As the extinction coefficient increases, the incoming radiation is attenuated at a faster rate; therefore, more of this incoming radiation is absorbed closer to the surface of the collector (where the heat loss occurs) resulting in lower collector efficiencies.

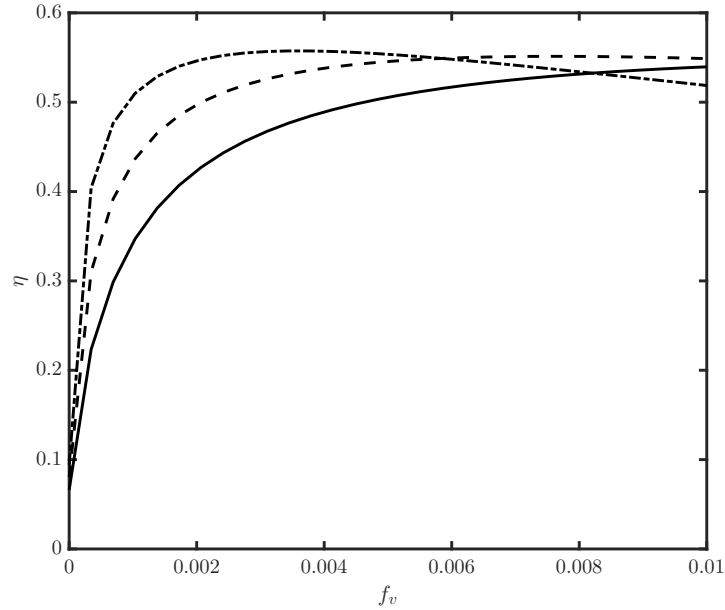


Figure 4.7: Efficiency of the solar collector versus particle volume fraction for $R = 0.0006$ (solid line), $R = 0.0012$ (dashed line), and $R = 0.0024$ (dot-dashed line).

4.3 Summary and discussion

In this chapter, we modelled the efficiency of a novel NDASC design. The solar collector was described in a three-dimensional cylindrical coordinate system in Section 4.2.1. We modelled the conservation of energy in the system in Section 4.2.2; this model included a term describing the nanofluid flow (discussed in Section 4.2.3) and an expression describing the absorption of incoming solar radiation (discussed in Section 4.2.4). We nondimensionalised the model and applied realistic parameter values in order to investigate the relative importance of the dimensionless parameters in Section 4.2.6. Unlike in previous chapters, in this chapter the temperature of the nanofluid in the collector was obtained

numerically rather than analytically. This temperature was used to calculate the efficiency of the collector. We presented and discussed our results in Section 4.2.8. This NDASC design has two fundamental flaws. Firstly, cooling takes place over a large surface area in this design. The ratio between the aperture area and receiver area is $\pi/2$; so, the total surface area where heat loss takes place is $\pi/2$ times larger in Collector 3 than in Collectors 1 and 2. This ratio can be reduced by concentrating the incoming solar radiation (more on this in the upcoming chapters), or by simply adopting the parallel plate NDASC design used in Collectors 1 and 2. Secondly, much of the incoming radiation is not normal to the receiver surface. In a volumetric receiver, one must also consider the angle that the incoming radiation makes to the normal of the receiver; this angle determines P^* , the maximum path length that incoming radiation can propagate through before exiting the absorbing medium. Suppose the incoming radiation makes an angle of $\hat{\theta}$ to the normal (as shown in Figure 4.8), then $P^* = 2R \cos \hat{\theta}$.

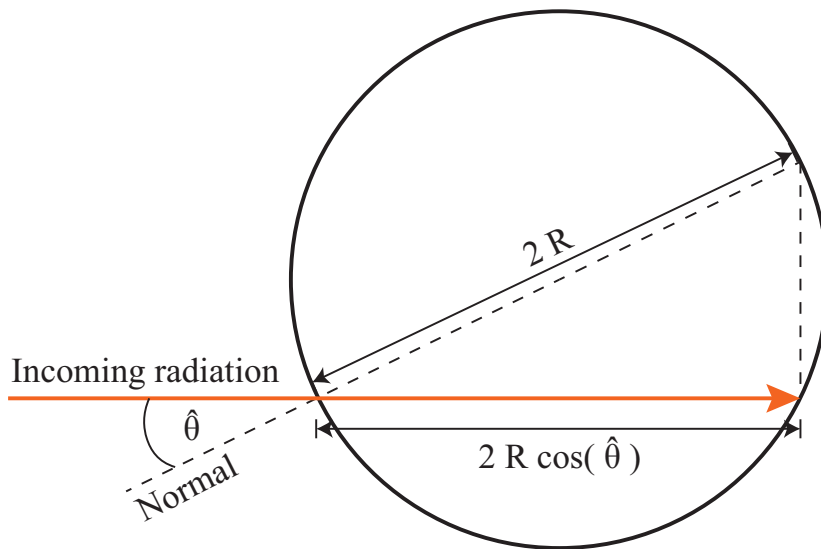


Figure 4.8: Incoming radiation at an angle of $\hat{\theta}$ to the normal.

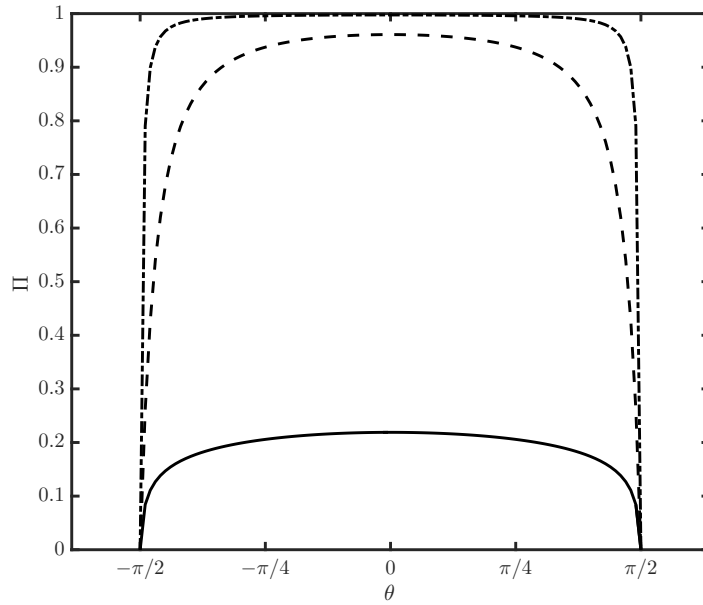
When designing a solar collector, one must ensure that P^* is large enough for most of the incoming radiation to get absorbed. Recall from (2.2.21), the heat source term was given by

$$q^*(z^*) = \frac{G_s^* \beta_0 \beta_1}{H \left(1 + \frac{\beta_0}{H} z^*\right)^{\beta_1 + 1}}. \quad (4.3.1)$$

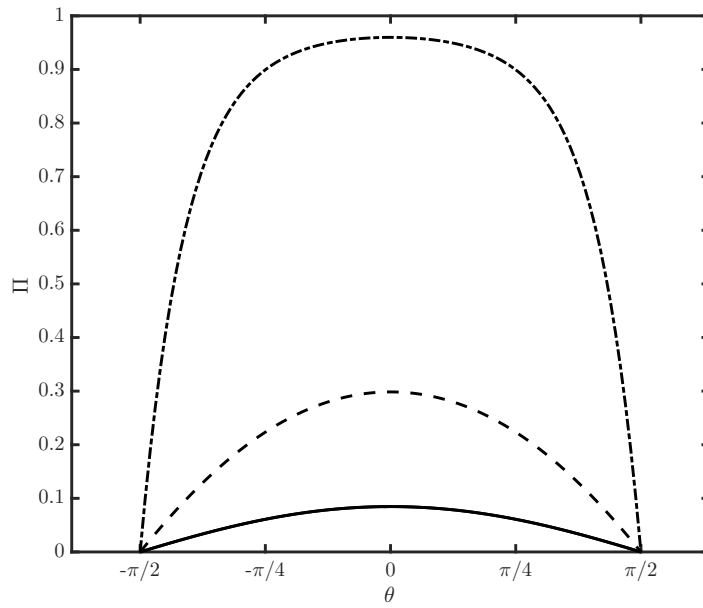
Integrating (4.3.1) from zero to P^* with respect to z^* reveals an expression for the overall amount of radiation absorbed by the collector when incoming radiation has a maximum path-length of P^* . One can divide this integral by the amount of solar radiation at the surface of the collector to obtain Π , where Π is the total fraction of incoming radiation that gets absorbed by the collector, more explicitly

$$\Pi = \frac{\int_0^{P^*} q^*(z^*) dz^*}{G_s^*} = 1 - \frac{1}{\left(1 + \beta_0 \cos \hat{\theta}\right)^{\beta_1}}. \quad (4.3.2)$$

Figure 4.9 shows how Π varies with $\hat{\theta}$ across three different nanofluid particle volume fractions for a) a water based nanofluid flowing through a receiver, and b) a Therminol[®] VP-1 based nanofluid flowing through a receiver. Overall, the water based nanofluid is a better absorber of incoming radiation than the Therminol[®] VP-1 based nanofluid at each particle volume fraction. The path-length P^* is maximised when $\hat{\theta} = 0$, and the radiation travels normal to the collector surface; therefore, Π is also maximised when $\hat{\theta} = 0$. As $\hat{\theta}$ moves further from 0 and P^* gets smaller, the collectors absorb less of the incoming radiation.



(a)



(b)

Figure 4.9: Fraction of incoming radiation absorbed as it passes through a 1 cm diameter receiver (Π) versus incident radiation angle to the normal (θ) for $f_v = 0$ (solid lines), $f_v = 0.0005$ (dashed lines), and $f_v = 0.006$ (dot-dashed lines) (a) water based nanofluent, and (b) Therminol[®] VP-1 based nanofluent.

CHAPTER 5

COLLECTOR 4: A LOW-PROFILE PARABOLIC TROUGH NDASC

5.1 Introduction

Li et al. [38] compare the performance of a concentrating NDASC with the performance of a similar surface-absorbing collector, demonstrating that overall, both collectors can perform well, but that more research is needed on volumetric receivers. However, Li et al.'s solar concentration method uses a combination of prisms and parabolic reflectors to focus solar radiation onto the surface of a collector; while this method works quite well for surface based solar collectors (where the radiation is absorbed at the surface of the collector), it does not necessarily work as well for volumetric collectors because the concentrated radiation is not always normal to the receiver. However, in light of their promising experimental results, and the clear room for design improvement, in this chapter we design and model another new solar collector design (Collector 4). As Figure 5.1 shows, in Collector 4, incoming solar radiation is concentrated onto the receiver by a parabolic trough; therefore, it is called a nanofluid-based direct absorption parabolic trough solar collector (NDAPSC). While NDAPSCs have been studied previously, Collector 4 is a novel design wherein incoming solar radiation is reflected and concentrated by a parabolic trough reflector into the nanofluid which flows through an optically transparent pipe that is situated on the focal line of

the parabolic reflector. A parabolic reflector concentrates incoming radiation (that is parallel to its plane of symmetry) onto its focal line. This method of solar concentration is useful as it ensures that incoming radiation is normal to the receiver (see Figure 5.5 for an illustration of this effect). In this design, the volumetric flow rate is reduced in order to achieve a high temperature yield and the nanofluid flow is controlled and driven by a pump (unlike the collectors from previous chapters).

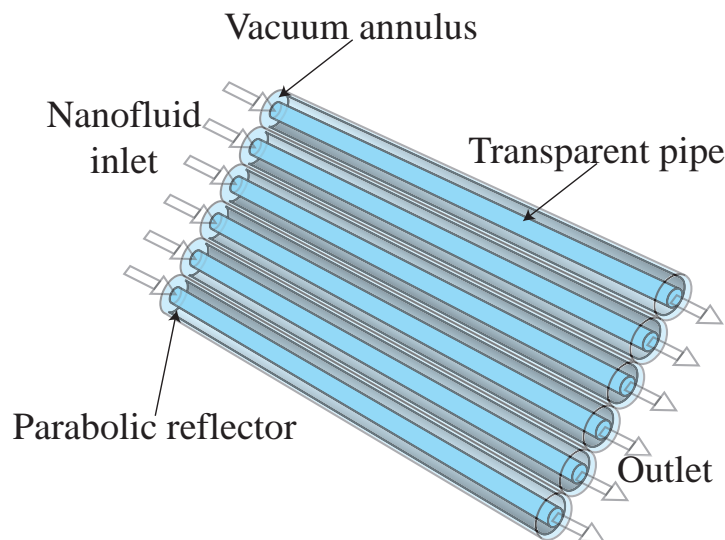


Figure 5.1: General design of Collector 4.

Collector 4 incorporates several ideas not yet introduced in this thesis; in Section 5.2, we discuss these design considerations further. Collector 4 is modelled as a three-dimensional cylindrical pipe where laminar flow is driven by a pressure gradient. This cylindrical coordinate system used in this chapter is slightly different to the one used to model Collector 3, and so we define it in Section 5.3.1. Section 5.3.2 discusses the conservation of energy in the system. The steady-state Navier-Stokes equations for laminar, incompressible fluid flow are applied to find the velocity profile of the nanofluid as it flows through the collector in Section 5.3.3. In Section 5.3.4 we define a novel heat source term in this new coordinate system. The heat source and velocity terms are used to express the conservation of energy in its complete form before the model is non-dimensionalised in Section 5.3.6. We apply sensible parameter values to the model from a realistic case study and Section 5.3.6 also describes how the Crank-Nicolson scheme is applied to the dimensionless energy equation to obtain a numerical solution for

temperature. However, the traditional Crank-Nicolson scheme introduces some error into the system and so we outline a method for reducing this error. We use the temperature solution to express collector efficiency, which is used to discuss the performance of Collector 4 in Sections 5.3.7 and 5.4.

5.2 Design considerations

5.2.1 Heat-mirrors

Taylor et al. [59] note that since most base fluids are good absorbers at longer wavelengths, most nanofluids will be good emitters at those same wavelengths. Some solar collectors operate at low temperatures where heat lost due to Black-body radiation is negligible; however, at higher operating temperatures, Black-body radiation is the dominant mechanism for heat loss. Khullar et al. [28] observe that volumetric-based solar collectors are a promising technology, however, radiative losses tend to escalate as operating temperatures rise. One solution to overcome the problem of Black-body radiative heat losses is to install a heat-mirror over the collector to stop long-wavelength emitted radiation from leaving the system. A heat-mirror is a selectively transmissive/reflective material that is highly transparent at short (solar) wavelengths, but highly reflective at long wavelengths. If the surface of a volumetric receiver is coated with a suitable heat-mirror, most of the incoming solar radiation is able to pass through the surface while the majority of the emitted Black-body radiation is reflected off the surface and prevented from leaving the system [28, 38, 59].

Although selective absorbing surfaces are well developed and very successful commercially, selective transparent surfaces are comparatively underserved by scientific literature [58]. There is limited existing research in applying heat-mirrors to NDASCs; moreover, no previous study has determined the analytic relationship between heat-mirrors and collector efficiency.

Fan and Bachner [16] introduce the heat-mirror for use in solar-thermal energy conversion applications in 1976. They compare the performance of Sn-doped In_2O_3 selectively transparent coatings and TiO_2 selectively transparent coatings, against selective absorbing coatings under similar operating conditions (solar air mass of two and the temperature of the Black-body, $T_{Bb}^* = 121^\circ\text{C}$). Under these operating conditions, the $0.35\ \mu\text{m}$ thick, Sn-doped In_2O_3 film coated with

an MgF_2 anti-reflection coating, performed the best out of all of the selectively transparent coatings with effective solar transmittance and the effective infra-red emissivity values of $F = 0.9$ and $\epsilon = 0.081$ respectively. While Fan and Bachner's [16] results are promising, they do not explore the full parameter space of potential operating conditions for solar collectors; many volumetric solar collectors can operate at various different temperatures.

Li et al. [38] use numerical simulations and experimental data to compare the performance of an NDASC coated with a heat-mirror (indium tin oxide (ITO)) versus a more traditional surface-based absorber coated with a selective absorbing material (black chrome). They demonstrate that both receivers could work. The ITO coating on borosilicate glass has an effective solar absorptivity and the effective infra-red emissivity values of $F = 0.82$ and $\epsilon = 0.35$ at room temperature. Figure 5.2 (which is a graph of Table 3 from Li et al., [38]) shows that the black chrome's black-body weighted emittance rises as the absorber's temperature increases from 50-250 °C; meanwhile, the glass/ITO tube's emittance is relatively constant across the same Black-body temperature range. Black chrome has a higher emissivity at short wavelengths, whereas glass/ITO has relatively constant optical properties for long wavelengths. The black chrome is more optimised for solar-thermal applications. Li et al. [38] conclude that volumetric receivers may yet provide an effective and a low-cost approach to bring nanotechnology into industrial heating and air-conditioning applications, but that more research is needed.

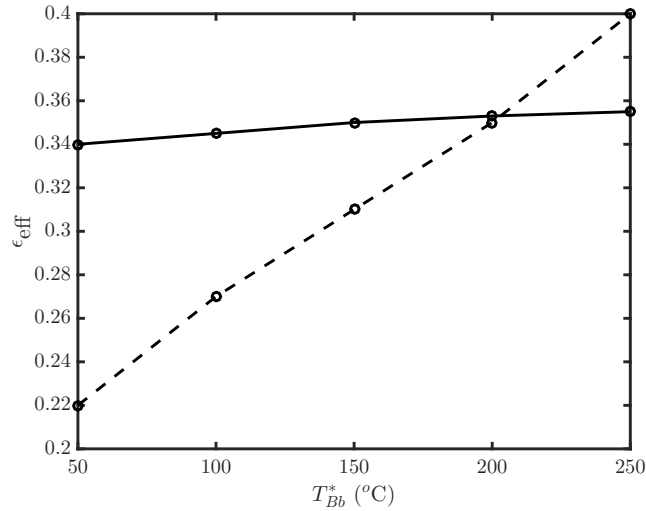


Figure 5.2: Effective emissivity versus Black-body temperature for an ITO coated on borosilicate glass (solid line), and black chrome coated on copper (dashed line) from Table 3 in Li et al., [38].

Taylor et al. [57, 58] examine two categories of heat-mirror (‘type-1’, and ‘type-2’) using various metrics to determine their suitability for use in solar collectors. They categorise ‘type-1’ materials by a dielectric-metal-dielectric sandwich in which the materials and the thicknesses of the three layers each represent a degree of design freedom; and, they categorise ‘type-2’ by single-layer dispositions of doped semiconductors, namely, transparent conductive oxides. Taylor et al. [58] report that thin films of ITO and ZnS-Ag-ZnS provided the most promising results; the best ‘type-1’ heat-mirror reported is ZnS-Ag-ZnS, and the best ‘type-2’ heat-mirror reported is ITO—for example, at a concentration ratio of 10 and $T_{Bb}^* = 100$ °C, $F = 0.845$ and $\epsilon = 0.53$ for ZnS-Ag-ZnS and $F = 0.803$ and $\epsilon = 0.408$ for ITO [58]. At lower temperatures they conclude that uncoated collectors are more efficient where radiative heat losses are smaller. They note that ‘type-2’ heat-mirrors are more commercially viable since they are easier to manufacture.

There are two frameworks for assessing the performance of a heat-mirror, the first was introduced by Fan and Bachner [16] and the second was introduced by Taylor et al. [57]. To evaluate a heat-mirror’s performance, Fan and Bachner [16] define the effective solar transparency, τ_{eff} , and the effective infra-red emissivity,

ϵ_{eff} , of a heat-mirror as

$$\tau_{\text{eff}} = \frac{\int_0^\infty F(\lambda) J_s(\lambda) d\lambda}{\int_0^\infty J_s(\lambda) d\lambda}, \quad \epsilon_{\text{eff}} = \frac{\int_0^\infty (1 - R(\lambda)) J_{Bb}(\lambda) d\lambda}{\int_0^\infty J_{Bb}(\lambda) d\lambda}, \quad (5.2.1)$$

where $J_s(\lambda)$ is the incoming solar radiance, $J_{Bb}(\lambda)$ is the outgoing Black-body radiance, ϵ_{eff} is the fraction of Black-body radiation that is not reflected, and $R(\lambda)$ is the wavelength-dependent reflectance. In this framework τ_{eff} should be maximised and ϵ_{eff} should be minimised. Taylor et al. [57] introduces the Efficiency Factor of Selectivity (EFS) as an alternative, albeit similar, metric for assessing heat-mirror performance. The EFS is defined as

$$\text{EFS} = \frac{G_s^* C_A \tau_{\text{eff}} - \tau_{Bb,\text{eff}} \sigma T_{Bb}^{*4} - \epsilon \sigma T_{Bb}^{*4}}{G_s^* C_A}, \quad (5.2.2)$$

where $\tau_{Bb,\text{eff}}$ is the effective transmittance of the heat-mirror to Black-body radiation at temperature T_{Bb}^* , and C_A is the solar concentration ratio. We note that Fan and Bachner [16] combine $\tau_{Bb,\text{eff}}$ and ϵ to calculate ϵ_{eff} , and this is one of the key differences between the two metrics. In the EFS framework, a heat-mirror with a higher EFS score is more desirable, a heat-mirror's EFS score depends on the T_{Bb}^* and C_A , along with its optical properties. The EFS framework enables us to easily compare two different heat-mirrors against each other; however, since the optical properties of an ideal heat-mirror are not explicitly defined in the literature, the maximum possible EFS score is unknown—this value would be a useful tool for evaluating heat-mirrors further and understanding the scope for future performance improvements. In Appendix B we discuss ideal-heat mirrors further before giving an upper bound to the maximum possible EFS score by calculating the hypothetical optical properties of an ideal heat-mirror.

5.2.2 Collector design

In this section we summarise Collector 4's design; or, more specifically, we outline three potential variations of this design (shown in Figure 5.3). Collector 4 (a) has no vacuum annulus, Collector 4 (b) has a vacuum annulus but no heat-mirror coating, and Collector 4 (c) has a vacuum annulus and a heat-mirror coating. The vacuum annulus and heat-mirror coatings enhance thermal efficiency by negating Newton cooling/radiative heat losses; however, they also reduce optical efficiency.

In the following sections we compare all three design variations to understand how they affect NDAPSC performance.

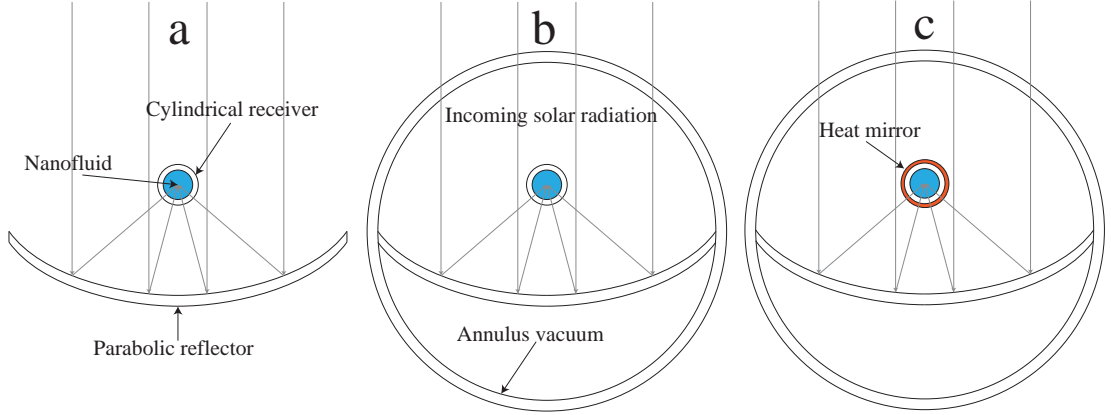


Figure 5.3: The three different DAPSC designs tested in this study.

These three designs are similar in principle to the vacuum glass tube component of the collector proposed by Li et al. [38], with a few notable differences: (1) The width of the parabolic trough is maximised so that it is equal to the inner diameter of the vacuum glass tube, (2) These tubes rotate to track the sun, while Li et al.'s design [38] has no moving parts, (3) This design does not incorporate lens or prisms, the parabolic trough is the only mechanism for solar concentration.

5.3 Model

5.3.1 Introduction

A cylinder with radius R is used to represent the receiver. As shown in Figure 5.4, (x^*, r^*, ϕ) define a three-dimensional cylindrical coordinate system such that x^* is the axial coordinate, r^* is the radial coordinate and ϕ is the angle highlighted (again, $*$ denotes a dimensional variable). The nanofluid enters the collector at the inlet ($x^* = 0$) with an initial temperature of T_I^* . It is pumped through the system while being heated as it absorbs incoming solar radiation before exiting at the outlet ($x^* = L$) with a final temperature of T_O^* , and a boundary condition of $T_{x^*}^* = 0$.

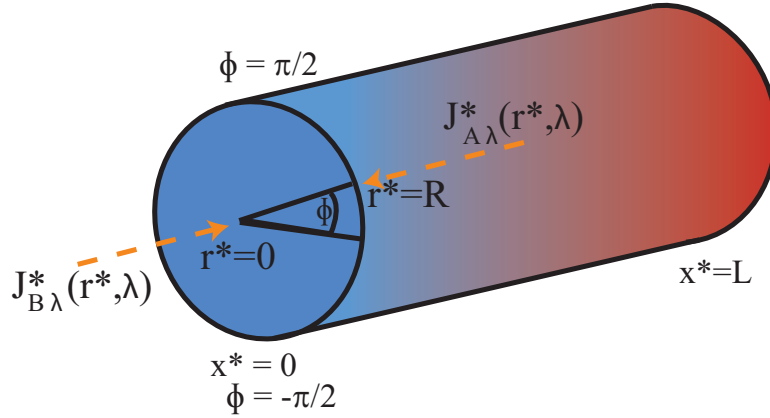


Figure 5.4: Schematic of receiver in cylindrical geometry.

5.3.2 Conservation of energy

The steady-state equation describing the conservation of heat energy in this system is

$$\rho_{nf} c_{p,nf} \mathbf{u} \cdot \nabla T^* = k_{nf} \nabla^2 T^* + q. \quad (5.3.1)$$

Heat loss takes place via both Newton cooling and thermal radiation. Thus, the boundary condition at the surface of the receiver is

$$T_{r^*}^*|_R = \frac{h_s}{k_{nf}} (T^*|_R - T_{Amb}^*) + \frac{\sigma \epsilon}{k_{nf}} (T^{*4}|_R - T_{Amb}^{*4}), \quad (5.3.2)$$

where h_s is the surface heat transfer coefficient, σ is Stefan's constant, and ϵ is the emissivity constant. The second term of the boundary condition represents the radiative cooling/heating.

5.3.3 Conservation of momentum

In order to achieve a high temperature yield in this low-profile parabolic-trough solar collector, the volumetric flow rate is low (in this study we explore a case when the mean flow rate, \bar{u}^* , is up to 0.1 ms^{-1}); this results in lower Reynolds numbers and laminar flow regimes. The Reynolds number is $\text{Re} = 2\bar{u}^* R/\nu$, where R is the radius of the pipe and ν is the kinematic viscosity of the working fluid. Pipe flow is typically laminar when $\text{Re} < 2000$, in this study we consider cases when $\text{Re} < 1000$. So, flow in the receiver is laminar, Newtonian, and steady; the

incompressible continuity equation in cylindrical coordinates is

$$\frac{\partial u^*}{\partial x^*} + \frac{1}{r^*} \frac{\partial (r^* v^*)}{\partial r^*} + \frac{1}{r^*} \frac{\partial w^*}{\partial \phi} = 0. \quad (5.3.3)$$

At the surface of the receiver there is a no-slip condition, and thus $\mathbf{u}|_{r^*=R} = 0$. Since the velocity field is axisymmetric and this is a parallel flow, (5.3.3) reduces to

$$\frac{\partial u^*}{\partial x^*} = 0, \quad (5.3.4)$$

indicating that $u^* = u^*(r^*)$. Ignoring the effects of gravity in the receiver, the steady-state momentum equation is

$$\frac{\partial p^*}{\partial x^*} = \frac{\mu}{r^*} \frac{\partial}{\partial r^*} \left(r^* \frac{\partial u^*}{\partial r^*} \right), \quad (5.3.5)$$

where p^* is the system pressure. Solving (5.3.5) and applying the boundary conditions

$$u^*(R) = 0, \quad \left. \frac{du^*}{dr^*} \right|_{r^*=0} = 0, \quad (5.3.6)$$

yields

$$u^*(r^*) = \frac{1}{4\mu} \frac{dp^*}{dx^*} (r^{*2} - R^2). \quad (5.3.7)$$

Alternatively, this velocity term is expressed in terms of mean velocity, \bar{u}^* , rather than pressure gradient. The mean velocity is defined as

$$\bar{u}^* = \frac{2\pi}{\pi R^2} \int_0^R r^* u^* dr^* = -\frac{R^2}{8\mu} \frac{dp^*}{dx^*}, \quad (5.3.8)$$

and so (5.3.7) is equivalently

$$u^*(r^*) = 2\bar{u}^* \left(1 - \frac{r^{*2}}{R^2} \right). \quad (5.3.9)$$

5.3.4 Heat source term

We apply a combination of coordinate geometry and calculus to express the angular and depth dependence of the solar intensity throughout the receiver. A parabolic mirror can be represented in coordinate geometry with the function $p(\hat{x}) = \hat{x}^2/4f$, where f is the focal length of the mirror—this is illustrated in Figure 5.5.

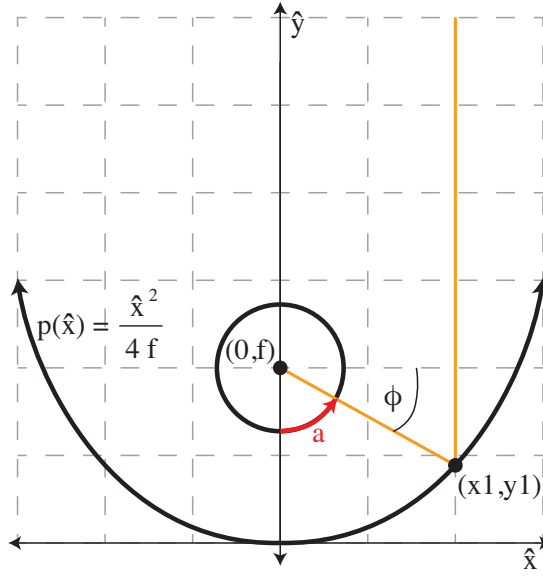


Figure 5.5: Parabolic concentrator in a coordinate geometry system where a is the arc-length highlighted, f is the focal length, and p is the quadratic line shown.

We use the chain rule to obtain a term that describes the incoming solar intensity at the surface of the receiver, i.e.,

$$G_{s,1}^* = \frac{dG_{s,c}^*}{da} = \frac{dG_{s,c}^*}{d\hat{x}} \frac{d\hat{x}}{d\phi} \frac{d\phi}{da}, \quad (5.3.10)$$

where the cumulative solar intensity, $G_{s,c}^*$, is defined as the overall amount of solar radiation between $\hat{x} = 0$ and $\hat{x} = X$, i.e.,

$$G_{s,c}^* = \int_0^X G_s^* d\hat{x} = G_s^* \hat{x}, \quad (5.3.11)$$

and $x \geq 0$. This chain rule method requires expressions for ϕ as a function of \hat{x} , and the arclength a as a function of ϕ (this arclength is shown in Figure 5.5). The angle ϕ is expressed as a function of \hat{x} via the relation

$$\tan \phi = \frac{p(\hat{x}) - f}{\hat{x}} = \frac{\hat{x}^2 - 4f^2}{4f\hat{x}}. \quad (5.3.12)$$

Rewriting (5.3.12) by isolating for \hat{x} yields

$$\hat{x} = 2f (\tan \phi + \sec \phi). \quad (5.3.13)$$

The arc-length a is given by

$$a(\phi) = R \left(\frac{\pi}{2} + \phi \right). \quad (5.3.14)$$

Using (5.3.10)-(5.3.14), the incoming solar intensity at the surface of the receiver is

$$G_{s,1}^* = \frac{dG_{s,c}^*}{da} = \frac{G_{s,a}2f}{R} (\sec \phi (\tan \phi + \sec \phi)) = \frac{G_{s,a}2f}{R} \frac{1}{\sin \phi - 1}. \quad (5.3.15)$$

However, we note that a physical system has a finite aperture width and so $G_{s,1}^*$ is only given by (5.3.15), while $\phi \leq \phi_{\text{crit}}$ (where ϕ_{crit} is the maximum angle of incoming reflected solar radiation). This angle is limited by the width of the aperture, W , and so

$$\phi_{\text{crit}} = \arctan \left[\frac{(W/2)^2 - 2f^2}{fW} \right]. \quad (5.3.16)$$

More specifically, the solar intensity at the surface of the collector is given by the piecewise function

$$G_{s,1}^*(\phi) = \begin{cases} 0 & \text{if } \phi > \phi_{\text{crit}} \\ \frac{G_{s,a}2f}{R} \frac{1}{\sin \phi - 1} & \text{if } \phi \leq \phi_{\text{crit}}. \end{cases} \quad (5.3.17)$$

Equation (5.3.17) is also derived in Jeter [24]; however, we apply a different method. We note that the method outlined in this section assumes that all of the solar intensity at the aperture hits the parabolic reflector, i.e., shadowing caused by the receiver is negligible; this assumption is also made by Jeter [24].

The spectral irradiance at the surface of the receiver is $G_{s,1}(\phi)J_0^*$, where $G_{s,1} = G_{s,1}^*/G_s^*$, and J_0^* is approximated via Planck's Black-body relation, i.e.,

$$J_0^* = \frac{2hc^2\Omega_S S_{Att} \Upsilon_T^2 \Upsilon_R}{\lambda^5 \left(\exp \left(\frac{hc}{\lambda k_B T_S^*} \right) - 1 \right)}, \quad (5.3.18)$$

where Υ_R and Υ_T are the reflectivity of the concentrator and the transmittance of the glass tube/envelope respectively. We note that this expression of J_0^* is valid when the collector consists of a glass tube surrounded by a glass annulus, i.e., incoming solar radiation passes through two layers of glass after being reflected

by the parabolic mirrors and so the transmittance of the glass is applied twice.

Our source term differs from [29] in that we split the spectral intensity into two parts, $J_{A\lambda}^*$ and $J_{B\lambda}^*$, as shown in Figure 5.4. Incoming radiation intensity at the surface of the receiver is denoted by $J_{A\lambda}^*$; in addition, since we are working in the domain $0 \leq r^* \leq R$ and $-\pi/2 \leq \phi \leq \pi/2$, we must also include $J_{B\lambda}^*$, the solar intensity remaining after the radiation has passed through the other half of the receiver. Recall from Chapter 3 where a similar method was applied when we also split up the solar intensity into its incoming and outgoing directional components. The angular dependence of outgoing intensity, $G_{s,2}^*(\phi)$, is introduced via a transformation of $G_{s,1}^*$,

$$G_{s,2}^*(\phi) = \begin{cases} 0 & \text{if } \phi < -\phi_{\text{crit}} \\ \frac{G_{s,1}^* 2f}{R} \frac{1}{1 - \sin(-\phi)} & \text{if } \phi \geq -\phi_{\text{crit}}. \end{cases} \quad (5.3.19)$$

While this collector is designed to reach higher temperatures than Collectors 1-3, we still model a system that operates at temperatures below 750 K, and thus follow the approach of [66] where thermal re-emission in the fluid is presumed negligible since it constitutes less than 5% of the total radiative heat loss. The change in normally incident solar radiation is given by the radiative transport equations

$$\frac{1}{r^*} \frac{\partial}{\partial r^*} (r^* J_{A\lambda}^*) = K_e J_{A\lambda}^*, \quad \frac{1}{r^*} \frac{\partial}{\partial r^*} (r^* J_{B\lambda}^*) = -K_e J_{B\lambda}^*, \quad (5.3.20)$$

with the associated boundary conditions

$$J_{A\lambda}^*(r^* = R) = J_0^*, \quad J_{A\lambda}^*(r^* \rightarrow 0) = J_{B\lambda}^*(r^* \rightarrow 0). \quad (5.3.21)$$

The solutions to (5.3.20) are thus

$$J_{A\lambda}^*(r^*) = \frac{J_0^* R}{r^*} e^{-K_e(R-r^*)}, \quad J_{B\lambda}^*(r^*) = \frac{J_0^* R}{r^*} e^{-K_e(R+r^*)}. \quad (5.3.22)$$

To determine the corresponding radiative fluxes, $P_A^*(r^*, \phi)$, and $P_B^*(r^*, \phi)$, we integrate (5.3.22) over the entire spectrum and multiply by the angular dependences

to obtain

$$P_A^*(r^*, \phi) = G_{s,1}(\phi) \int_0^\infty \frac{J_0^* R}{r^*} e^{-K_e(R-r^*)} d\lambda, \quad (5.3.23)$$

$$P_B^*(r^*, \phi) = G_{s,2}(\phi) \int_0^\infty \frac{J_0^* R}{r^*} e^{-K_e(R+r^*)} d\lambda. \quad (5.3.24)$$

Equations (5.3.23) and (5.3.24) are highly non-linear with respect to wavelength due to the J_0^* and K_e terms. To make analytic progress we follow the previously discussed approach of Cregan and Myers [10] and use the method of least squares to approximate (5.3.23) and (5.3.24) obtaining

$$P_A^*(r^*, \phi) = \frac{RG_{s,1}^*(\phi)}{r^*} \left(\frac{1}{\left(1 + \frac{\beta_0}{2R}(R-r^*)\right)^{\beta_1}} \right), \quad (5.3.25)$$

$$P_B^*(r^*, \phi) = \frac{RG_{s,2}^*(\phi)}{r^*} \left(\frac{1}{\left(1 + \frac{\beta_0}{2R}(R+r^*)\right)^{\beta_1}} \right). \quad (5.3.26)$$

Incoming radiation enters the receiver at $r^* = R$ and is attenuated due to scattering and absorption as it passes through the receiver. There is a singularity at $r^* = 0$; as $r^* \rightarrow 0$ the solar intensity becomes infinitely concentrated since the focal point of the parabolic concentrator coincides with the centre point of the receiver. The qualitative behaviours of P_A^* and P_B^* across three particle volume fractions are depicted in Figure 5.6. In the pure base fluid, incoming radiation is attenuated at a much slower rate than it is concentrated; we observe a rapid rise in P_A^* as $r^* \rightarrow 0$, and a rapid decay in P_B^* as $r^* \rightarrow R$. The incoming solar intensity at the surface of the receiver, $P_A^*(r^* = R)$, is less than twice as large as the outgoing solar intensity at the surface of the receiver, $P_B^*(r^* = R)$. Therefore, less than half of the available solar radiation is absorbed as it passes through the receiver. As the nanofluid's particle volume fraction increases, so does its extinction coefficient. When $f_v = 0.006$ the incoming solar radiation is attenuated quicker than it is concentrated and we observe a sharp decline in P_A^* as $r^* \rightarrow 0$. The outgoing solar radiation is very low when $f_v = 0.006$ as almost all of the available solar energy has been absorbed by the nanofluid before it reaches the centre of the receiver. The nanofluid with a relatively low particle volume fraction ($f_v = 0.0005$) exhibits an interesting combination of the traits of a pure base fluid and a higher particle volume fraction. Similar to the base fluid, we still observe a rapid rise in P_A^* as $r^* \rightarrow 0$, and a rapid decay in P_B^* as $r^* \rightarrow R$.

This indicates that the solar intensity is still being concentrated faster than it is attenuated. However, the outgoing solar radiation, $P_B^*(r^* = R)$, is noticeably much smaller than the outgoing solar intensity in the pure base fluid. Even at small particle volume fractions, the nanofluid absorbs much more of the incoming solar radiation than the pure base fluid.

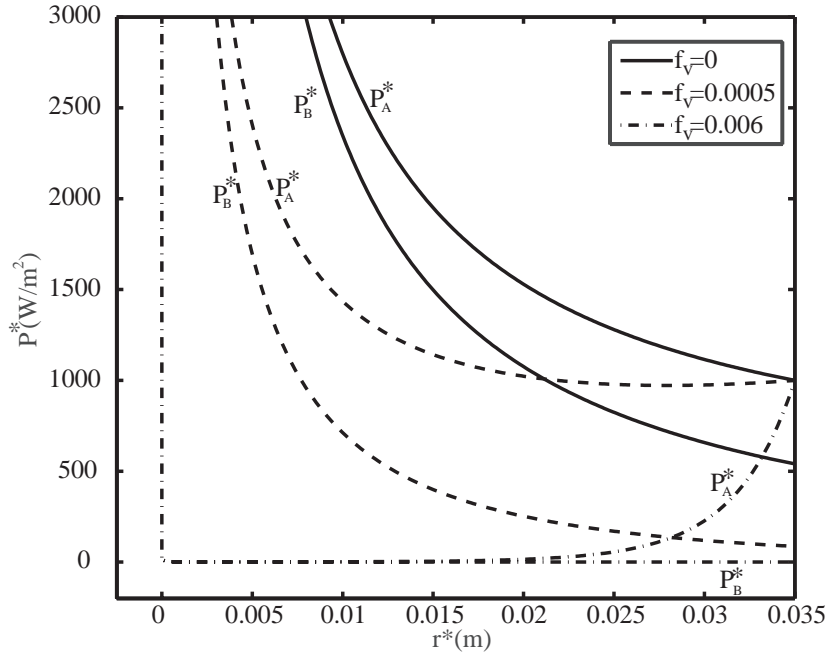


Figure 5.6: Solar intensity against radial distance for a Therminol[®] VP-1/Aluminium nanofluid with $f_v = 0$ (solid lines), $f_v = 0.0005$ (dashed lines), and $f_v = 0.006$ (dash-dotted lines).

In spite of the singularity at $r^* = 0$, (5.3.26) can be differentiated analytically to obtain the heat source term

$$q(r^*, \phi) = \frac{1}{r^*} \left(\frac{d}{dr^*}(r^* P_A^*) - \frac{d}{dr^*}(r^* P_B^*) \right) \quad (5.3.27)$$

$$= \frac{\beta_0 \beta_1}{2r^*} \left(\frac{G_{s,1}^*(\phi)}{\left(1 + \frac{\beta_0}{2R}(R - r^*)\right)^{\beta_1+1}} + \frac{G_{s,2}^*(\phi)}{\left(1 + \frac{\beta_0}{2R}(R + r^*)\right)^{\beta_1+1}} \right). \quad (5.3.28)$$

We rewrite the energy equation, (5.3.1), using the velocity profile in (5.3.9) and

the source term in (5.3.28):

$$\rho_{nf} c_{p,nf} 2\bar{u}^* \left(1 - \frac{r^{*2}}{R^2}\right) \frac{\partial T^*}{\partial x^*} = k_{nf} \left(\frac{1}{r^*} \frac{\partial}{\partial r^*} \left(r^* \frac{\partial T^*}{\partial r^*} \right) + \frac{1}{r^{*2}} \frac{\partial^2 T^*}{\partial \phi^2} + \frac{\partial^2 T^*}{\partial x^{*2}} \right) + q^*(r^*, \phi) \quad (5.3.29)$$

We non-dimensionalise this expression via the dimensionless variables:

$$x^* = Lx, \quad \bar{T}^* = T_I^* + \Delta T T, \quad z^* = Hz. \quad (5.3.30)$$

The temperature scale

$$\Delta T = \frac{G_{s,a} \beta_0 \beta_1 f L}{\bar{u}^* \rho_{nf} c_{p,nf} 2R^2}, \quad (5.3.31)$$

is chosen so that the temperature variation is driven by the source term. The dimensionless heat equation is thus:

$$(1 - r^2) \frac{\partial T}{\partial x} = \gamma \left(\frac{1}{r} \frac{\partial}{\partial r} \left(r \frac{\partial T}{\partial r} \right) + \frac{1}{r^2} \frac{\partial^2 T}{\partial \phi^2} \right) + \frac{1}{2\text{Pe}} \frac{\partial^2 T}{\partial x^2} + q(\phi, r), \quad (5.3.32)$$

with the dimensionless boundary conditions

$$\left. \frac{\partial T}{\partial \phi} \right|_{\phi=-\pi/2, \pi/2} = 0, \quad (5.3.33)$$

and

$$\left. \frac{\partial T}{\partial r} \right|_{r=1} = -\text{Nu}(T|_{r=1} + \hat{T}) + \hat{\gamma} (1 - (\lambda + \varphi T|_{r=1})^4), \quad (5.3.34)$$

where

$$\text{Pe} = \frac{\rho_{nf} c_{p,nf} L \bar{u}^*}{k_{nf}}, \quad \gamma = \left(\frac{L}{R} \right)^2 \frac{1}{2\text{Pe}}, \quad \varphi = \frac{\Delta T}{T_A^*}, \quad (5.3.35)$$

$$\hat{T} = \frac{T_I^* - T_A^*}{\Delta T}, \quad \lambda = \frac{T_I^*}{T_A^*}, \quad (5.3.36)$$

$$\text{Nu} = \frac{Rh_s}{k_{nf}}, \quad \hat{\gamma} = \frac{\sigma R \epsilon T_A^{*4}}{\Delta T k_{nf}}. \quad (5.3.37)$$

Recall, the Peclet number, Pe, describes the ratio of thermal advection to thermal diffusion, the Nusselt number, Nu, describes the ratio of convective to conductive heat transfer across the boundary, and $\hat{\gamma}$ describes the ratio of radiative to conductive heat transfer across the boundary for a black-body at ambient temper-

ature. The dimensionless parameters and their effects are summarised in Table 5.1. Two of the dimensionless parameters, γ , and $1/\text{Pe}$, describe the relative size of thermal diffusion, while the other dimensionless parameters are used to describe heat loss across the boundary at $r^* = R$.

Table 5.1: Dimensionless parameters and their effects on the system.

Dimensionless parameter	Physical constituents	Physical significance
Nu	R, h_s, k_{nf}	More heat is lost due to
\hat{T}	$T_I^*, T_A^*, G_{s,a}^*, \Upsilon_T, \Upsilon_R,$ $f_v, R, f, \bar{u}^*, \rho_{nf}, c_{p,nf}$	Newton cooling as dimensionless parameter increases
$\hat{\gamma}$	$\sigma, \epsilon, T_A^*, k_{nf}, G_{s,a}^*, \Upsilon_T,$ $\Upsilon_R, f_v, R, f, \bar{u}^*, \rho_{nf},$ $c_{p,nf}$	More heat is lost due to radiative cooling as dimensionless parameter increases
λ	T_I^*, T_A^*	parameter increases
φ	$T_A^*, G_{s,a}^*, \Upsilon_T, \Upsilon_R, f_v, R,$ $f, \bar{u}^*, \rho_{nf}, c_{p,nf}$	
γ	$L, R, \bar{u}^*, \rho_{nf}, c_{p,nf}, k_{nf}$	Diffusion is more
$1/\text{Pe}$	$L, \bar{u}^*, \rho_{nf}, c_{p,nf}, k_{nf}$	significant as dimensionless parameter increases

We also rescale the temperature at the inlet to obtain $T(x = 0) = 0$. The rescaled dimensionless source term, $q(\phi, r)$, is defined in terms of the two dimensionless expressions

$$G_{s,1}(\phi) = \begin{cases} 0 & \text{if } \phi > \phi_{\text{crit}} \\ \frac{1}{1-\sin\phi} & \text{if } \phi \leq \phi_{\text{crit}}, \end{cases} \quad (5.3.38)$$

and

$$G_{s,2}(\phi) = \begin{cases} 0 & \text{if } \phi < -\phi_{\text{crit}} \\ \frac{1}{1-\sin(-\phi)} & \text{if } \phi \geq -\phi_{\text{crit}}, \end{cases} \quad (5.3.39)$$

such that

$$q(\phi, r) = \frac{1}{r} \left(\frac{G_{s,1}(\phi)}{\left(1 + \frac{\beta_0}{2}(1-r)\right)^{\beta_1+1}} + \frac{G_{s,2}(\phi)}{\left(1 + \frac{\beta_0}{2}(1+r)\right)^{\beta_1+1}} \right). \quad (5.3.40)$$

5.3.5 Case Study

As a case study we compare the performance of the three different potential low-profile DAPSC designs illustrated in Figure 5.1(b). All three designs are assumed to use the same working fluid, a Therminol[®] VP-1/Aluminium nanofluid, and common parameters—which are given in Table 5.2. Table 5.3 shows the parameter values for the glass tubes [18], parabolic trough mirror [29], and heat-mirror [16]. Collector 4 (a) contains a parabolic mirror and a glass tube, Collector 4 (b) contains a parabolic mirror, a glass tube and a glass envelope, and Collector 4 (c) contains a parabolic mirror, a glass tube, a glass envelope, and a heat-mirror. The parameter values in these tables are in line with parameter spaces explored previously in the literature [10, 29, 38] and they are chosen with careful consideration so that they fit the collector design. For example, the maximum height, H_m , of a low-profile NDAPSC is a limiting factor to the maximum width of the aperture, W_m , through the relationship $W_m = 4\sqrt{H_m f}$, where f is the focal length of the parabolic concentrator. We choose parameter values to ensure this rule is not violated and (similar to the collector design in Li et al., [38]) $H_m < 15$ cm in this system.

5. COLLECTOR 4: A LOW-PROFILE PARABOLIC TROUGH NDASC

Table 5.2: Solar collector and nanofluid parameters and physical constants.

Quantity	Symbol	Value	Units
Collector length, radius	L, R	1, 0.005	m
Viscosity (Therminol [®] VP-1)	μ_{bf}	2.48×10^{-6}	$\text{kg m}^{-1} \text{s}^{-1}$
Surface heat transfer coefficient	h_s	6.43	$\text{W m}^{-2} \text{K}^{-1}$
Ambient, initial temperature	T_A^*, T_I^*	30, 250	$^{\circ}\text{C}$
Incident solar radiation	G_s^*	1000	W m^{-2}
Density Therminol [®] VP-1, Aluminium	ρ_{bf}, ρ_{np}	1060, 2700	kg m^{-3}
Conductivity Therminol [®] VP-1, Aluminium	k_{bf}, k_{np}	0.1357, 247	$\text{W m}^{-1} \text{K}^{-1}$
Specific heat capacity Therminol [®] VP-1, Aluminium	$c_{p,bf}, c_{p,np}$	1570, 900	$\text{J kg}^{-1} \text{K}^{-1}$
Mean velocity downstream	\bar{u}^*	0.1	ms^{-1}
Fitting parameters (for $\phi = 0.006$)	β_0, β_1	10.60, 1.14	-

Table 5.3: NDAPSC optical parameter values used in case study [16, 18, 29].

	Parabolic mirror	Tube/envelope	Heat-mirror
Material	Low-iron glass	Low-iron antireflective glass	Sn-doped In_2O_3 & Corning 7059 glass
Reflectivity	0.93	-	0.912 (Radiative heat loss)
Transmittance	-	0.96	0.90 (Incoming solar radiation)
Width (m)	0.13	-	-

Table 5.4: Dimensionless parameter values for three different input temperatures ranges and three different particle volume fractions ($f_v = 0, f_v = 0.0005, f_v = 0.006$). $T_A^* = 20^{\circ}\text{C}$, $Q = 0.912 \times 10^{-3} \text{ m}^3\text{s}^{-1}$.

	$T_I = 0^{\circ}\text{C}$	$T_I = 100^{\circ}\text{C}$	$T_I = 200^{\circ}\text{C}$
1/Pe	$(8.49, 8.29, 8.59) \times 10^{-7}$	$(7.21, 7.04, 7.3) \times 10^{-7}$	$(6.07, 5.93, 6.14) \times 10^{-7}$
γ	(0.017, 0.017, 0.017)	(0.014, 0.014, 0.015)	(0.012, 0.012, 0.012)
φ	(0.004, 0.015, 0.135)	(0.003, 0.014, 0.124)	(0.003, 0.013, 0.117)
λ^4	(0.659, 0.659, 0.659)	(2.296, 2.296, 2.296)	(5.93, 5.93, 5.93)
$\hat{\gamma}$	(14.42, 3.63, 0.39)	(16.98, 4.28, 0.45)	(20.16, 5.08, 0.54)
Nu	(0.233, 0.238, 0.23)	(0.252, 0.258, 0.248)	(0.282, 0.289, 0.278)
\hat{T}	(-27.06, -6.66, -0.73)	(68.86, 16.94, 1.86)	(177.12, 43.58, 4.79)
Re	403.23	403.23	403.23

5.3.6 Solution method

The efficiency of the solar collector, η , is defined as the fraction of usable thermal energy to incident solar energy [12]. We recall from Chapter 4,

$$\eta = \frac{2 \int_{-\frac{\pi}{2}}^{\frac{\pi}{2}} \int_0^R \rho_{nf} c_{p,nf} r^* u^*(r^*) (T_O^* - T_I^*) dr^* d\phi}{G_{s,a} LW}. \quad (5.3.41)$$

This is equivalently expressed using the dimensionless terms which were introduced in (5.3.30):

$$\eta = \frac{2\beta_0\beta_1 f}{W} \int_{-\frac{\pi}{2}}^{\frac{\pi}{2}} \int_0^1 (r - r^3) T_O dr d\phi. \quad (5.3.42)$$

The system defined in (5.3.32) - (5.3.34) can be reduced further by exploring the magnitude of the dimensionless parameters in Table 5.4. Since $\varphi, 1/\text{Pe} \ll 1$, their effect on the system is negligible and the energy equation can be reduced to

$$(1 - r^2) \frac{\partial T}{\partial x} = \gamma \left(\frac{1}{r} \frac{\partial}{\partial r} \left(r \frac{\partial T}{\partial r} \right) + \frac{1}{r^2} \frac{\partial^2 T}{\partial \phi^2} \right) + q(\phi, r). \quad (5.3.43)$$

Although we note that negating the effect of $1/\text{Pe}$, means that the thin boundary layer at $x^* = L$ is ignored (we revert the readers attention back to Chapter 2 where this is discussed in greater detail). The dimensionless symmetry boundary condition is

$$\left. \frac{\partial T}{\partial \phi} \right|_{\phi=-\pi/2, \pi/2} = 0, \quad (5.3.44)$$

and the linearised, thermal-exchange boundary condition is

$$\left. \frac{\partial T}{\partial r} \right|_{r=1} = -\text{Nu}(T|_{r=1} + \hat{T}) + \hat{\gamma} (1 - (\lambda^4 + 4\lambda^3\varphi T|_{r=1})). \quad (5.3.45)$$

We note that although γ is a relatively small term, ignoring it results in a solution where both boundary conditions cannot be satisfied simultaneously. Since (5.3.43) is singular at $r = 0$ and $r = 1$ (where the boundary conditions are imposed) and the source term is piecewise, this system requires a numerical solution. We apply a modified Crank-Nicolson scheme to equations (5.3.32)-(5.3.40) and describe it in terms of discretised temperature $T_{i,j}^n$ —the modified Crank-Nicolson method is discussed in further detail in Appendix C.

5.3.7 Results

Collector 4 is a novel NDASC design, therefore we are unable to make direct comparisons between the results in this chapter and results from prior literature. That notwithstanding, Collector 4's performance characteristics mirror qualitative phenomena exhibited by NDASCs in previous studies. The optimal collector

design is dependent on the operating conditions. This section compares the performance of all three collector variations across a wide parameter space to gain an insight into when and why each collector design is most efficient. The results depicted in Figures 5.7–5.11 are generated using the modified Crank-Nicolson method (which is detailed in Appendix C) and the spatial discretisation is defined by: $I = 40$, $J = 60$, and $N = 1500$.

Figure 5.7 plots the collector efficiency versus inlet temperature for Collector 4 (a) (dot-dashed line), Collector 4 (b) (dashed line), and Collector 4 (c) (solid line). As the inlet temperature increases, the dimensionless parameters λ and \hat{T} also increase, resulting in greater heat lost due to Newton and radiative cooling. As T_I^* increases (and thermal losses grow), thermal efficiency (i.e., minimising heat loss to the surroundings) becomes a more important design consideration. This effect is demonstrated in Figure 5.7: when $T_I^* > 237^\circ\text{C}$, Collector 4 (c) is more efficient than Collector 4 (b) due to its superior thermal efficiency. The heat-mirror's emissivity is much lower than the glass' emissivity ($0.088 \ll 0.92$), therefore $\hat{\gamma}$ is lower in Collector 4 (c) than it is in the other two collector designs. Collector 4 (c) is the most thermally efficient design, so, while all three Collectors become less efficient as T_I^* increases, the efficiency of Collector 4 (c) is significantly less sensitive to changes in T_I^* than the efficiency of the other two collector designs—as expected due to its superior thermal efficiency. However, we also note from Figure 5.7 that at lower inlet temperatures, Collector 4 (a) is the best performing design (in fact, when $T_I^* < 237^\circ\text{C}$ Collector 4 (c) is the least efficient design). At lower operating temperatures (when thermal losses are small), it is more important to optimise a collector's optical efficiency (i.e., maximise the amount of incoming radiation) than its thermal efficiency.

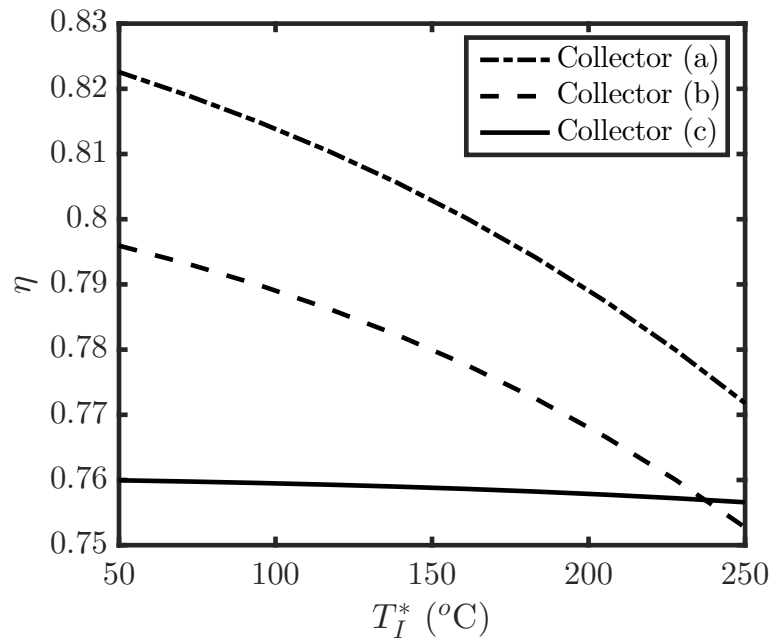


Figure 5.7: Efficiency of a solar collector versus inlet temperature for Collector 4 (a) (dot-dashed line), Collector 4 (b) (dashed line), and Collector 4 (c) (solid line).

As the radius of the receiver increases, the following dimensionless parameters change: Nu , \hat{T} , $\hat{\gamma}$, γ , and φ ; more specifically, Nu and \hat{T} are proportional to R and R^2 respectively, while $\hat{\gamma}$, φ , and γ are inversely proportional to R^3 , R^2 and R^2 respectively. Physically, when R increases, the surface area of the receiver (where heat loss occurs) also increases; meanwhile, the volume of liquid in the receiver increases and so the mean temperature in the system decreases. Figure 5.8 shows collector efficiency versus receiver radius for Collector 4 (a) (dot-dashed line), Collector 4 (b) (dashed line), and Collector 4 (c) (solid line). We note that Figure 5.8 only illustrates NDAPSC performance when R is sufficiently low enough for the flow to remain laminar; if the nanofluid's flow was turbulent, the collector's performance would be assessed using the model proposed in the next chapter. We use Π (the total fraction of incoming radiation that is absorbed by the collector) to explain the sharp rise in efficiency as R increases from 0.001 m to 0.003 m in Figure 5.8. When R is small, Π is also small, so collector efficiency improves as R increases from 0.001 m to 0.003 m (and $\Pi \rightarrow 1$). However, after the majority of the available radiation has been absorbed, any further increase in R leads to an efficiency reduction due to increased thermal losses. When $R > 0.01$ m, Collector 4 (c) is more efficient than the other two designs because it loses less heat due to

black-body radiation. We recall (from the discussion of Figure 5.7) that Collector 4 (c) is the most thermally efficient collector design, this is also demonstrated by Figure 5.8. When either $R < 0.0038$ m or $R > 0.01$ m, Collector 4 (c) outperforms the other two collectors. As R decreases, the volume of liquid in the cross section also decreases, leading to warmer operating conditions. When $R < 0.0038$ m, and the receiver's cross section is smallest, Collector 4 (c) is the best design due to its thermal efficiency.

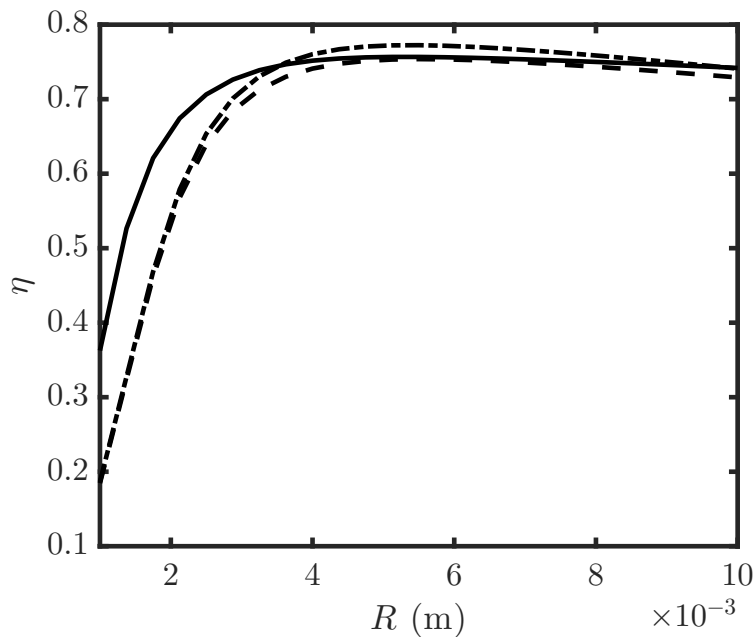


Figure 5.8: Efficiency of a solar collector versus receiver radius for Collector 4 (a) (dot-dashed line), Collector 4 (b) (dashed line), and Collector 4 (c) (solid line).

The mean velocity downstream affects the dimensionless parameters, \hat{T} , $\hat{\gamma}$, φ , γ , and Pe ; physically this suggests that as \bar{u}^* increases, heat loss and thermal diffusion effects become less significant. This can be explained as follows: as \bar{u}^* increases, the nanofluid spends less time in the receiver resulting in lower temperatures, and hence, lower thermal losses. Menbari et al. [42] show (using experimental and numerical results) that an NDAPSC's efficiency improves as its nanofluid flow rate increases. Figure 5.9 shows the efficiency of an NDAPSC as the mean velocity increases from 0.0025 ms^{-1} to 0.025 ms^{-1} for Collector 4 (a) (dot-dashed line), Collector 4 (b) (dashed line), and Collector 4 (c) (solid line). As expected, all three collectors demonstrate good qualitative agreement with

Menbari et al.'s [42] relationship between velocity and collector efficiency. In this scenario, Collector 4 (a) is the most efficient design when $\bar{u}^* > 0.0025 \text{ ms}^{-1}$; however, at lower velocities (i.e., hotter operating conditions) Collector 4 (c) is the most efficient design.

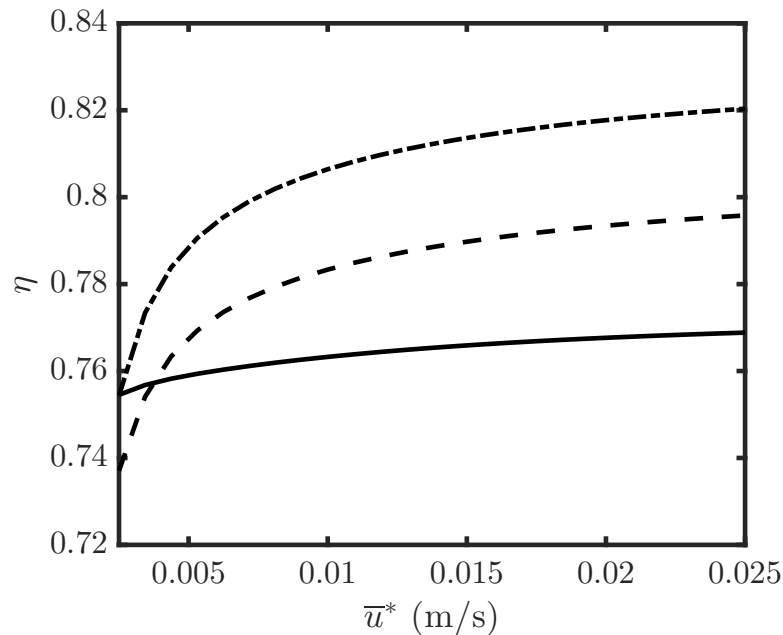


Figure 5.9: Efficiency of a solar collector versus mean velocity downstream for Collector 4 (a) (dot-dashed line), Collector 4 (b) (dashed line), and Collector 4 (c) (solid line).

Figure 5.10 demonstrates the relationship between collector efficiency and the nanofluid's particle volume fraction for Collector 4 (a) (dot-dashed line), Collector 4 (b) (dashed line), and Collector 4 (c) (solid line). As f_v increases, the working fluid absorbs more of the available incoming radiation, and so the collector's efficiency increases. This efficiency enhancement is initially large as f_v increases from 0 to 0.004, however, it subsides as f_v increases further and $\Pi \rightarrow 1$, i.e., all of the available incoming radiation has been absorbed. This observation confirms a widely observed result in previous studies of nanofluid-based direct absorption solar collectors [10, 29, 63, 66]. Interestingly, we note from Figure 5.10 that all three collectors perform similarly across the range of particle volume fractions studied. However, Collector 4 (a) is the most efficient design at higher particle volume fractions and Collector 4 (c) is the most efficient design in the case of a pure base fluid. Even though Collector 4 (a) has the highest radiative

and convective thermal losses, it is still more efficient than the other designs when $f_v > 0.001$ because it is more optically efficient: in Collector 4 (a), the incoming radiation only passes through one layer of glass. Therefore, the other collectors lose at least 4% more of the overall incoming solar radiation due to optical inefficiencies. If the glass surrounding the annulus vacuum had a higher transmissivity, the efficiencies of Collectors (b) and (c) would increase.

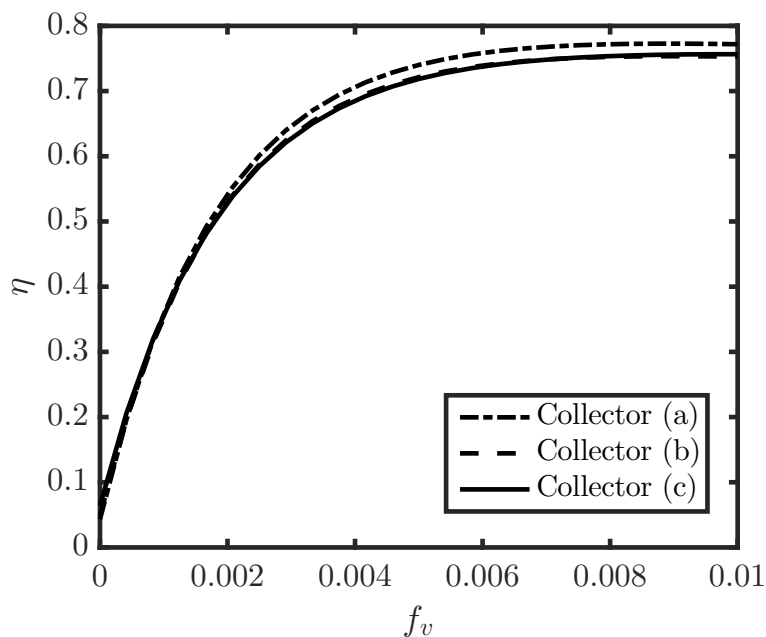


Figure 5.10: Efficiency of a solar collector versus the nanofluid’s particle volume fraction for Collector 4 (a) (dot-dashed line), Collector 4 (b) (dashed line), and Collector 4 (c) (solid line).

Figure 5.11 shows collector efficiency versus (a) focal length, and (b) aperture width for Collector 4 (a) (dot-dashed line), Collector 4 (b) (dashed line), and Collector 4 (c) (solid line). These plots also highlight how ϕ_{crit} affects collector efficiency, and the numerical solution method. We recall from (5.3.16) that ϕ_{crit} decreases as f increases and as W decreases. Due to the piecewise nature of the source term, (5.3.40), most of the incoming radiation is absorbed in the domain $[-\pi/2, \phi_{\text{crit}}]$, whilst nanofluid flowing through the rest of the receiver is predominantly heated via thermal diffusion. When ϕ_{crit} decreases, incoming solar radiation is concentrated onto a smaller fraction of the overall receiver, this leads to hotter maximum temperatures in the system. We note from Figure 5.11(a) that all three collectors perform more optimally at shorter focal lengths when

the system's temperature is more uniform; and furthermore, collector efficiency declines approximately linearly as ϕ_{crit} decreases. As W increases two conflicting phenomena affect collector performance: (1) more energy enters the system, leading to hotter temperatures which causes greater thermal losses, (2) ϕ_{crit} increases (and as Figure 5.11(a) shows, this leads to more uniform cross sectional temperatures which causes lower thermal losses). Figure 5.11(b) demonstrates how both of these phenomena interact, and affect collector efficiency. At smaller aperture widths, Collector 4 (c) is the most efficient design, however, when $W > 0.07$ m Collector 4 (a) demonstrates superior levels of efficiency. We note how the efficiency of all three collectors increases as W increases, and so phenomena (2) is a greater determinant of collector efficiency than phenomena (1) in this parameter space.

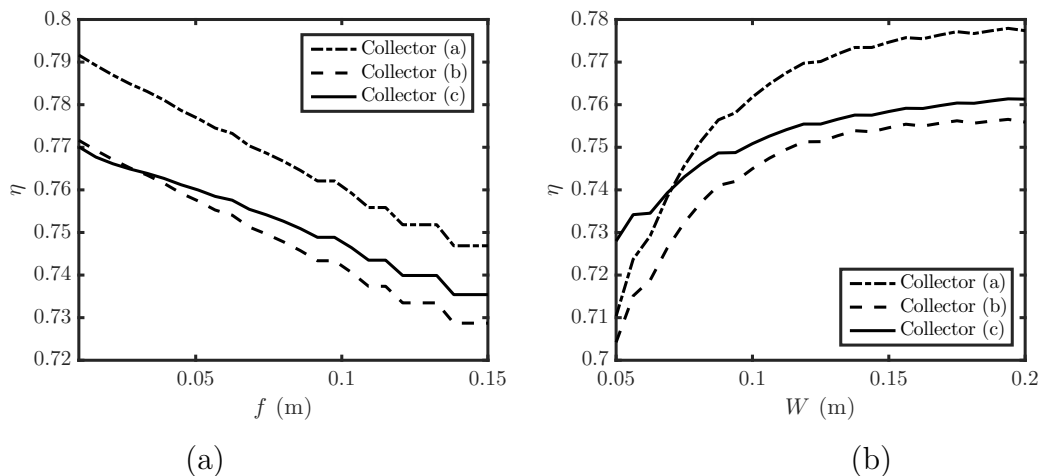


Figure 5.11: Efficiency of a solar collector versus (a) focal length, and (b) aperture width for Collector 4 (a) (dot-dashed line), Collector 4 (b) (dashed line), and Collector 4 (c) (solid line).

We note how Figures 5.11(a) and 5.11(b) exhibit increasingly erratic results as f increases and as W decreases. This volatility is caused by the piecewise nature of the source term. More specifically, the Crank-Nicolson method is less accurate as ϕ_{crit} decreases since this causes the source term's non-linearities to become more pronounced. In order to improve this model's numerical reliability, we modified the traditional Crank-Nicolson scheme and introduced an improved finite difference method (this is discussed in more detail in Appendix C). We note that the erratic perturbations in Figures 5.11(a) and 5.11(b) are $O(0.1\%)$, and

we also note that these results were generated via the improved finite difference method. In Appendix C, Figure C.2 shows that the traditional (unmodified) Crank-Nicolson scheme produces volatile errors $O(5\%)$ —had Figures 5.11(a) and 5.11(b) been generated using the traditional Crank-Nicolson scheme, the erratic perturbations would have been much larger.

5.4 Summary and discussion

In this chapter, we modelled the efficiency of another novel NDASC design. This collector design concentrates incoming solar radiation and can result in higher system temperatures; so, in Section 5.2.1 we discussed heat-mirrors since they offer a potential solution negating the increased thermal losses. We identified three possible configurations to a novel low-profile NDAPSC design: Collector 4 (a) had no vacuum annulus, Collector 4 (b) had a vacuum annulus, and Collector 4 (c) had a vacuum annulus and a heat-mirror. Collector 4 (a) was the most optically efficient design but the least thermally efficient, meanwhile, Collector 4 (c) was the least optically efficient design, but the most thermally efficient.

The model was governed by seven dimensionless parameters: two describe the rates of thermal diffusion to advection, two describe Newton cooling, and three describe radiative heat loss. We applied realistic parameter values from a case study to investigate the relative magnitudes of the dimensionless parameters in Section 5.3.5. This analysis revealed that one of the diffusive terms could be neglected and that the radiative heat-loss term could be linearised, resulting in a simplified system. The system of governing equations required a numerical method to obtain an expression for the outlet temperature. In Appendix C we introduced a modification to the standard Crank-Nicolson finite difference method which led to more accurate results, due to non-linearities in the source term.

We varied several of the system’s physical parameters to assess their affect on collector performance. The NDAPSC model shows qualitative performance agreement with existing NDAPSC models [28, 38, 42]: efficiency increased with increasing nanoparticle volume fraction, efficiency decreased with decreasing flow rates, and efficiency decreased with increasing inlet temperature. More specifically, Collector 4 (a) was the most efficient design at higher particle volume fractions while Collector 4 (c) was the most efficient design in the case of a pure base-fluid. Even though Collector 4 (a) had the highest radiative and convective

thermal losses, it was still more efficient than the other designs when $f_v > 0.001$ because it was more optically efficient. Also, Collector 4 (a) was the most efficient design when $\bar{u}^* > 0.0025 \text{ ms}^{-1}$; however, at lower velocities (i.e., hotter operating conditions) Collector 4 (c) was the most efficient design.

This chapter also explored the performance implications of design choices such as focal length, aperture width, and receiver radius. The focal length and aperture width determine ϕ_{crit} , and we found that collector efficiency declines approximately linearly as ϕ_{crit} decreases. We also found that at smaller aperture widths Collector 4 (c) was the most efficient design, however, when $W > 0.07 \text{ m}$ Collector 4 (a) demonstrated superior levels of efficiency. Meanwhile, when either $R < 0.0038 \text{ m}$ or $R > 0.01 \text{ m}$, Collector 4 (c) outperformed the other two collectors.

The parameter space exploration conducted in this study suggested that the optimal collector design largely depends on the operating conditions. Since Collector 4 (a) was the most optically efficient design, and Collector 4 (c) was the most thermally efficient design; in general, when greater thermal efficiency was desirable (i.e., when radiative heat losses are large), Collector 4 (c) outperformed the other designs. Meanwhile, at lower operating temperatures, greater optical efficiency was desirable and so Collector 4 (a) outperformed the other designs.

CHAPTER 6

COLLECTOR 5: A LARGE CONCENTRATING NDAPSC

6.1 Introduction

All of the previous collectors discussed in this thesis are low-profile, and thus small enough to fit on rooftops; however, in this chapter, we turn our attention towards a larger concentrating NDAPSC. We illustrate the general design of Collector 5 in Figure 6.1. Larger systems typically have higher Reynolds numbers and this leads to turbulent flow; therefore, this chapter includes some fundamental modelling differences to previous chapters. Recall, the Reynolds number is a well known ratio that determines the flow regime of a system; it is given by $Re = 2uR/\nu$, where u is the mean velocity of the fluid, and ν is the kinematic viscosity of the working fluid. This chapter focuses on a situation where Therminol[®] VP-1, a commonly used base-fluid, flows through a cylindrical pipe of diameter 7 cm, at a volumetric flow rate of $0.912 \times 10^{-3} \text{ m}^3\text{s}^{-1}$. This gives a Reynolds number of 13542—which is well inside the turbulent regime. For large Reynolds numbers, the turbulent thermal diffusion is much stronger than the molecular thermal diffusion [14]. Due to this turbulence, the nanofluid is well-mixed in the cross section as it flows through the receiver.

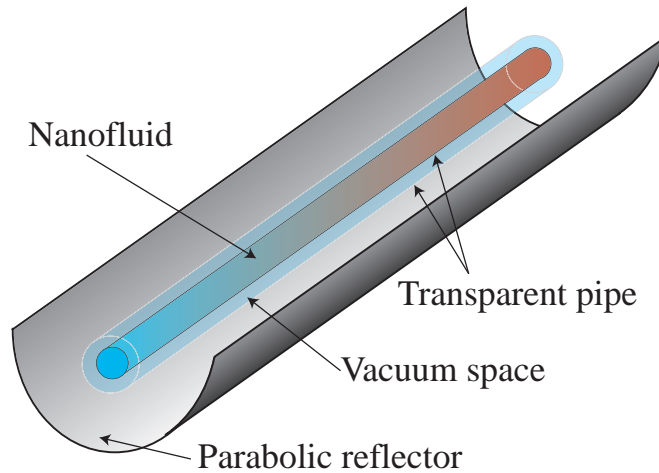


Figure 6.1: General design of Collector 5.

Khullar et al. [29] consider a two-dimensional model for the temperature and efficiency of an Al/Therminol[®] VP-1 based NDAPSC subject to coupled radiative and diffusive heat transfer in an absorbing, emitting, and scattering medium under plug flow. They compare a numerical treatment of their model with experimental data for conventional concentrating parabolic solar collectors, maintaining the same external conditions (i.e., ambient/inlet temperatures, wind speed, solar insolation, flow rate, concentration ratio, etc.). Khullar et al. [29] observe that NDAPSCs have 5-10% higher efficiency than conventional (surface-based) parabolic solar collectors. Menbari et al. [42] propose a model for a CuO/Water NDAPSC subject to steady turbulent depth-dependent flow. They validate the model by comparing a finite difference solution for the temperature with experimental results. Interestingly, in that study, the average axial nanofluid temperature rises almost linearly along the length of the receiver tube. Furthermore, the experimental and numerical results show that thermal efficiency of NDAPSCs improves by increasing the nanofluid flow rate. They also find that an increase in nanofluid particle volume fraction from 0.002% to 0.008% leads to an increase in thermal efficiency from 18% to 52%.

Analytical models for the performance of concentrating NDASCs are rare in the literature; moreover, analytic models for NDAPSCs are non-existent. Table 5 from Gorji and Ranjbar [19] provides a chronological summary of the literature on concentrating NDASCs. Of the seven studies mentioned, only one proposes a fully analytic solution for the temperature of the nanofluid as it flows through a receiver—Veeraragavan et al. [66]. Veeraragavan et al. assume laminar and

plug flow through a two-dimensional channel of height 1 cm and apply a zero-flux boundary condition at the bottom of the receiver. This model excludes the effect of scattering due to the nanoparticles, and also assumes that the base-fluid is a non-absorbing medium. Moreover, that model does not describe an NDAPSC—different types of concentrating systems must be modelled differently. The other six studies discussed in Table 5 from Gorji and Ranjbar [19] are numerical and/or experimental.

Many solar collectors are surrounded by a near-vacuum annulus to minimise convective heat loss in the system. Some solar collectors operate at low temperatures where thermal radiation is negligible, but at higher temperatures, blackbody radiation becomes the dominant mechanism for heat loss. Surface absorbing solar collectors receivers absorb solar radiation and emit black body radiation at the surface of the receiver. Coating a volumetric receiver with a selectively transmissive/reflective material, otherwise known as a 'heat-mirror', allows most of the incoming solar radiation through while trapping any emitted black body radiation inside the receiver [28, 38, 59]. Recall from Chapter 5, a heat-mirror is a selectively absorbing surface that is highly transparent at short (solar) wavelengths, but highly reflective at long (thermal emission) wavelengths. Li et al., [38] use numerical simulations and experimental data to compare the performance of volumetric absorbers coated with heat-mirrors versus more traditional surface-based absorbers coated with selective absorbing material, and demonstrates that overall, both receivers could work. They conclude that volumetric receivers may yet provide an effective and a low-cost approach to bring nanotechnology into industrial heating and air-conditioning applications, but that more research is needed. There is limited existing research in applying heat-mirrors to NDASCs; moreover, no previous study has determined the analytic relationship between heat-mirrors and collector efficiency.

While there has been some limited research on modelling of NDAPSCs, no existing model has been solved analytically. The cylindrical coordinate system used in this chapter was also used to model Collector 4 in Chapter 5; however, since each chapter in this thesis is designed to be readable as a stand-alone investigation, we redefine this cylindrical coordinate system in Section 6.2.1. In Section 6.2.2 we define the system and state the conservation of energy in the receiver at steady state. In Section 6.2.3 we discuss the incoming solar radiance and how it acts as a heat source. In Section 6.2.4 we reduce the model to a

one-dimensional problem before simplifying it further in Section 6.2.6 by applying realistic parameter values and then eliminating small terms arising from the dimensional analysis. We then solve the simplified model analytically and present results in Section 6.2.9.

6.2 Model

6.2.1 Introduction

Similar to Chapter 5, in this chapter we consider an NDAPSC with length L and a cylindrical receiver with radius R . As shown in Figure 6.2b, (x^*, r^*, ϕ) define a three-dimensional cylindrical coordinate system such that x^* is the axial coordinate, r^* is the radial coordinate and ϕ is the angle highlighted ($*$ denotes a dimensional variable). The nanofluid enters the receiver at the inlet ($x^* = 0$) at an initial temperature T_I^* before being pumped through the receiver. It is heated as it absorbs solar radiation and exits the receiver at the outlet ($x^* = L$) with a final temperature of T_O^* , and an outlet boundary condition of $T_{x^*}^*|_{x^*=L} = 0$.

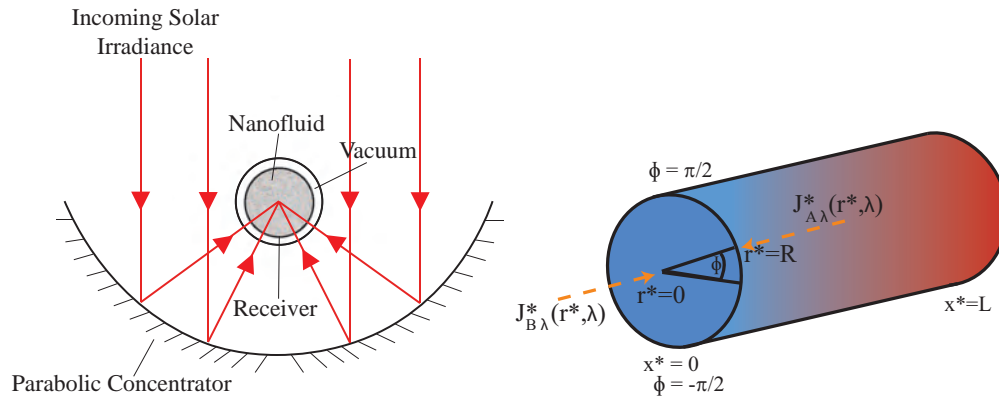


Figure 6.2: (a) Cross section of NDAPSC with length L and receiver with radius R , and (b) receiver geometry.

Since a vacuum surrounds the receiver, the only mechanism for heat loss occurs via thermal radiation at the receiver surface ($r^* = R$) [29, 42].

6.2.2 Conservation of energy

The steady-state equation describing the conservation of heat energy is

$$\rho_{nf} c_{p,nf} \mathbf{u} \cdot \nabla T^* = k_{nf} \nabla^2 T^* + q; \quad (6.2.1)$$

we recall from Chapter 5 that $\mathbf{u} = (u^*, w^*, v^*)$ is the fluid velocity, $T^*(x^*, r^*, \phi)$, the fluid temperature, q , the volumetric heat source, the subscript nf denotes nanofluid, and ρ_{nf} , $c_{p,nf}$, k_{nf} , are nanofluid density, specific heat capacity, and thermal conductivity respectively. This is a very similar conservation of energy system to the one used in Chapter 5 with one notable difference: in this model, fluid flow is turbulent. At the surface of the receiver there is no slip, and thus $u^*(R) = 0$. The radiative boundary condition at the surface of the receiver is

$$T_{r^*=R}^* = \frac{\sigma\epsilon}{k_{nf}} (T_A^{*4} - T^{*4}|_{r^*=R}), \quad (6.2.2)$$

where σ is Stefan's constant, ϵ the emissivity constant, and T_A^* the ambient temperature.

6.2.3 Heat source

In a NDAPSC, incoming is reflected off of the parabolic trough and onto the receiver where it is absorbed as it propagates through the nanofluid (this process is detailed more explicitly in Section 5.3.4). We apply the method from Chapter 5 and define the heat source term using (5.3.28), i.e.,

$$q(r^*, \phi) = \frac{\beta_0\beta_1}{2r^*} \left(\frac{G_{s,1}^*(\phi)}{\left(1 + \frac{\beta_0}{2R}(R - r^*)\right)^{\beta_1+1}} + \frac{G_{s,2}^*(\phi)}{\left(1 + \frac{\beta_0}{2R}(R + r^*)\right)^{\beta_1+1}} \right). \quad (6.2.3)$$

6.2.4 Solution method

Since the flow is turbulent, the nanofluid is fairly well mixed in the cross-sectional plane as it flows through the collector; so, $T(x^*, r^*, \phi) \simeq T(x^*)$. We multiply the heat equation (6.2.1) by r^* and integrate over the cross section to obtain the one-dimensional model

$$\frac{R^2}{2} \bar{u}^* T_{x^*}^* = \frac{k_{nf}}{\rho_{nf} c_{p,nf}} \left(\frac{R^2}{2} T_{x^*x^*}^* + \frac{R\sigma\epsilon}{k_{nf}} (T_A^{*4} - T^{*4}) \right) + \frac{\Pi R \pi C_A \Upsilon_T^2 \Upsilon_R G_s^*}{\rho_{nf} c_{p,nf}}, \quad (6.2.4)$$

where \bar{u} is the mean fluid velocity downstream, and we recall that Π is the total fraction of incoming radiation that gets absorbed as it propagates through the

receiver. To obtain Π , we integrate (6.2.3) over the cross-section, i.e.,

$$\Pi = \frac{1}{R\pi C_A \Upsilon_T^2 \Upsilon_R G_s^*} \int_{-\pi/2}^{\pi/2} \int_0^R r^* q(r^*, \phi) dr^* d\phi = 1 - \frac{1}{\left(\frac{\beta_0}{2} + 1\right)^{\beta_1}}. \quad (6.2.5)$$

Recall from Chapter 5 that the geometric concentration ratio, C_A , is defined to be the ratio of the aperture area to the receiver area, a ratio which was first used in the model of Duffie and Beckman [12] for concentrating solar collectors. The T^{*4} term in (6.2.4) arises from integration of the radial diffusion term: this requires a value for $T_{r^*}^*$ at $r^* = R$, which is given by the boundary condition, equation (6.2.2). Physically this implies that any energy added (or removed) at the boundary is immediately distributed through the fluid due to turbulence; hence, this energy enters the governing equation as a source (or sink) term.

6.2.5 Dimensional analysis

We define the dimensionless variables:

$$x^* = Lx, \quad \bar{T}^* = T_I^* + \Delta T T, \quad (6.2.6)$$

where the temperature scale

$$\Delta T = \frac{2\Pi C_A \Upsilon_T^2 \Upsilon_R G_s^* L}{\bar{u}^* \rho_{nf} c_{p,nf} R}, \quad (6.2.7)$$

is chosen since the source term drives the temperature variation. The dimensionless heat equation is now

$$T_x = \frac{T_{xx}}{\text{Pe}} + \gamma - (\tau + \varphi T)^4 + 1, \quad (6.2.8)$$

where

$$\text{Pe} = \frac{\rho_{nf} c_{p,nf} L \bar{u}^*}{k_{nf}}, \quad \gamma = \frac{\sigma \epsilon T_A^{*4}}{\Pi C_A \Upsilon_T^2 \Upsilon_R G_s^*}, \quad \varphi = \frac{\Delta T \gamma^{\frac{1}{4}}}{T_A^*}, \quad \tau = \frac{T_I^* \gamma^{\frac{1}{4}}}{T_A^*}. \quad (6.2.9)$$

We recall, the Peclet number (Pe) is a well-known dimensionless number describing the ratio of advection to thermal diffusion, γ is the ratio of absorbed background radiation to absorbed solar radiation, τ^4 is the ratio of emitted Black-body radiation to absorbed solar radiation where $T_{Bb}^* = T_I^*$, and φ^4 is the ratio of emit-

ted Black-body to absorbed solar radiation where $T_{Bb}^* = \Delta T$. The dimensionless inlet and outlet boundary conditions are $T(x = 0) = 0$, $T_x|_{x=1} = 0$.

6.2.6 Case study

As a case study for exploring our model further, we consider an Aluminum and Therminol[®] VP-1 nanofluid and, unless otherwise stated, use the parameter values given in Tables 6.1 and 6.2 which are largely taken from Khullar et al. [29]. The thermophysical properties of the aluminium nanoparticles are taken from [51]. Since the nanoparticles are added at very low concentrations, these properties will not significantly alter the thermophysical properties of the overall base-fluid and so for simplicity we assume them to be temperature-independent. We calculate the temperature-dependent thermophysical properties of Therminol[®] VP-1, (ρ_{bf} , k_{bf} , and $c_{p,nf}$,) using the formulas defined in [54] and the inlet temperature. The spectral-dependent refractive indexes n_{np} and n_{bf} and the nanoparticle absorption index κ_{np}^a are taken from [47, 51].

Symbol	Value	Units
R, L	0.035, 8	m
C_A	22.7364	–
T_A^*	20	°C
σ	5.67×10^{-8}	kg s ⁻¹ K ⁻⁴
ϵ	0.92	–
G_s^*	1000	W m ⁻²
Q	9.12×10^{-4}	m ³ s ⁻¹
ρ_{bf}	$1083 - 0.91T_I^* + 7.8 \times 10^{-4}T_I^{*2} - 2.37 \times 10^{-6}T_I^{*3}$	kg m ⁻³
ρ_{np}	2700	kg m ⁻³
k_{bf}	$0.14 - 8.2 \times 10^{-5}T_I^* - 1.9 \times 10^{-7}T_I^{*2} + 2.5 \times 10^{-11}T_I^{*3} - 7.3 \times 10^{-15}T_I^{*4}$	W m ⁻¹ K ⁻¹
k_{np}	247	W m ⁻¹ K ⁻¹
$c_{p,bf}$	$1498 + 2.41T_I^* + 6 \times 10^{-3}T_I^{*2} - 3 \times 10^{-5}T_I^{*3} + 4.4 \times 10^{-8}T_I^{*4}$	J kg K ⁻¹
$c_{p,np}$	900	J kg K ⁻¹

Table 6.1: Physical parameters used in case study [29, 51, 54].

Most nanofluids are expected to have radiation losses nearing those of a Black-body at long wavelengths [59] i.e., $\epsilon \approx 1$. A receiver coated with a heat-mirror will have significantly smaller thermal losses. In this section we compare the optical properties of two different heat-mirrors to determine the more suitable one for the NDAPSC in this case study. Heat-mirror 1 is Sn-doped In₂O₃ deposited on Corning 7059 glass—at 121 °C this heat-mirror reduces the effective emissivity to

$\epsilon_{eff} = 0.081$, but also reduces the effective transmission rate of the receiver by a factor of $\tau_{eff} = 0.90$ [16]. Heat-mirror 2 is ITO coated on borosilicate glass—this heat-mirror has an effective emissivity of $\epsilon_{eff} \approx 0.345$, and an effective solar transmission rate of $\tau_{eff} = 0.82$ [38]. At 121°C , Heat-mirror 1 has a superior solar transmission factor and a superior effective emissivity. Figure 5.2 shows that the effective emissivity of Heat-mirror 2 is approximately constant when $50^\circ\text{C} \leq T_{Bb}^* \leq 250^\circ\text{C}$; however, we do not have the equivalent experimental data for Heat-mirror 1. We acknowledge that ϵ_{eff} for Heat-mirror 1 is likely to have some temperature-dependence, i.e., $\epsilon_{eff} = \epsilon_{eff}(T^*)$; however, we assume that Heat-mirror 1 behaves like Heat-mirror 2 due to lack of experimental data i.e., its infra-red emissivity is approximately constant when $50^\circ\text{C} \leq T_{Bb}^* \leq 250^\circ\text{C}$.

	Parabolic mirror	Tube/envelope	Heat-mirror 1	Heat-mirror 2
Material	Low-iron glass	Pyrex glass	Sn-doped In_2O_3 & Corning 7059 glass	ITO on borosilicate glass
Reflectivity	0.93	-	0.912 (Radiative heat loss)	0.655 (Radiative heat loss)
Transmittance	-	0.95	0.90 (Incoming solar radiation)	0.82 (Incoming solar radiation)
Width (m)	5	-	-	-

Table 6.2: Concentrating NDASC parameter values [16, 29, 38].

	$T_I = 0^\circ\text{C}$	$T_I = 100^\circ\text{C}$	$T_I = 200^\circ\text{C}$
1/Pe	$(0.435, 0.426, 0.44) \times 10^{-7}$	$(0.4, 0.391, 0.405) \times 10^{-7}$	$(0.366, 0.358, 0.37) \times 10^{-7}$
γ	(1.075, 1.028, 1.02)	(1.075, 1.028, 1.02)	(1.075, 1.028, 1.02)
φ	(0.011, 0.022, 0.029)	(0.01, 0.021, 0.027)	(0.01, 0.02, 0.026)
τ^4	(0.057, 0.021, 0.015)	(0.198, 0.075, 0.053)	(0.511, 0.193, 0.137)

Table 6.3: Dimensionless parameter values for an uncoated solar collector for varying input temperatures for three different particle volume fractions ($f_v = 0$, $f_v = 0.0005$, $f_v = 0.006$).

6.2.7 Solution method

To simplify (6.2.8) we consider the magnitude of the dimensionless parameters, $1/\text{Pe}$, γ , φ , and τ . A parameter space study, shown in Table 6.3, indicates that both γ and τ^4 are $\text{O}(0.1)$, with $\tau^4 > \gamma$ when the inlet temperature is greater than the ambient temperature while both $1/\text{Pe}$ and φ are $\ll 1$. Typical values for $1/\text{Pe}$ are in the range $3 \times 10^{-8} - 5 \times 10^{-8}$ while φ is $\text{O}(10^{-2})$. Consequently we may neglect terms including $1/\text{Pe}$ and φ and reduce (6.2.8) to

$$T_x = 1 + \gamma - \tau^4. \quad (6.2.10)$$

We note that since the $1/\text{Pe}T_{xx}$ term does not appear in (6.2.10), the outlet boundary condition cannot be satisfied and so the thin boundary layer at $x^* = L$ is ignored in this model. Equation (6.2.10) only contains $O(1)$ and $O(0.1)$ terms; neglecting $1/\text{Pe}$ results in errors $\sim 10^{-6}\%$ and neglecting φ introduces errors $\sim 1\%$. While previous authors also neglect $1/\text{Pe}$ [66], our treatment of φ is new in the context of NDAPSC modelling. Solving (6.2.10), and applying the boundary condition $T(x = 0) = 0$, shows that the temperature in the system is approximated by

$$T(x) = (1 + \gamma - \tau^4) x. \quad (6.2.11)$$

Alternatively this can be expressed in full dimensional form as

$$T^*(x^*) = T_I^* + 2 \frac{\sigma \epsilon (T_A^{*4} - T_I^{*4}) + C C_A \Upsilon_T^2 \Upsilon_R G_s^*}{\bar{w} \rho_{nf} c_{p,nf} R} x^*. \quad (6.2.12)$$

When the receiver is covered with Heat-mirror 1, heat loss to the surroundings is very small; also, we replace $C_A G_s^*$ with $\tau_{eff} C_A G_s^*$ to account for a reduction of the solar intensity at the top of the receiver due to the transmittance of the heat-mirror. This results in a change to the dimensionless quantities in (6.2.9) such that $\gamma \approx 0$; therefore, $\varphi \approx 0$ and $\tau \approx 0$. In the case of Heat-mirror 1, (6.2.11) reduces to

$$T(x) = x, \quad (6.2.13)$$

or in full dimensional form

$$T^*(x^*) = T_I^* + 2 \frac{C \tau_{eff} C_A \Upsilon_T^2 \Upsilon_R G_s^*}{\bar{w} \rho_{nf} c_{p,nf} R} x^*. \quad (6.2.14)$$

We note that (6.2.11) and (6.2.13) indicate the temperature rise is linear as the nanofluid flows through the receiver. This qualitative behavior was previously observed experimentally and numerically in an NDAPSC by Menabari et al. [42].

6.2.8 Efficiency

The overall efficiency, η , is found by dividing the energy absorbed in the nanofluid as it flows through the length of the collector by the total solar energy over the aperture area [12]

$$\eta = \frac{\rho_{nf} c_{p,nf} \bar{w} \pi R^2 (T_O^* - T_I^*)}{C_A G_s^* L 2 \pi R}, \quad (6.2.15)$$

which may be expressed in dimensionless terms for the uncoated receiver as

$$\eta_u = C\Upsilon_T^2 \Upsilon_R (1 + \gamma - \tau^4), \quad (6.2.16)$$

or for the receiver coated with a heat-mirror as

$$\eta_c = \tau_{eff} C\Upsilon_T^2 \Upsilon_R. \quad (6.2.17)$$

Equations (6.2.16) and (6.2.17) are useful because they indicate exactly how to improve efficiency. Furthermore, they enable us to derive an inequality that compares an NDAPSC with a heat-mirror to an NDAPSC without a heat-mirror.

When $\eta_u > \eta_c$, i.e.,

$$\Pi\Upsilon_T^2 \Upsilon_R (1 + \gamma - \tau^4) > \tau_{eff} \Pi\Upsilon_T^2 \Upsilon_R, \quad (6.2.18)$$

an uncoated NDAPSC is more efficient than a coated NDAPSC. This expression may be reduced to obtain

$$\frac{1 + \gamma - \tau^4}{\tau_{eff}} > 1, \quad (6.2.19)$$

or in its equivalent dimensional form

$$\frac{\sigma\epsilon(T_A^{*4} - T_I^{*4}) + \Pi\Upsilon_T^2 \Upsilon_R C_A G_s^*}{\tau_{eff} \Pi\Upsilon_T^2 \Upsilon_R C_A G_s^*} > 1. \quad (6.2.20)$$

6.2.9 Results

Collector 5 is very similar to the solar collector proposed in Khullar et al., [29] and as expected, the efficiency values reported in this section match those reported in that study. A direct comparison is also made between the results in this chapter and the results from a similar system proposed by Menbari et al., who also observe the linear rise in temperature as the nanofluid flows through the collector [42]. We use the solutions for the temperature given by (6.2.12) and (6.2.14) to investigate various aspects of the system. Since different industrial processes operate at different temperatures and collector efficiency is of vital importance, we explore both outlet temperature and efficiency. Initially, we examine the net temperature change in the working fluid, where the temperature change is calculated from

(6.2.12) and (6.2.14) as

$$T_O^* - T_I^* = 2L \frac{\sigma \epsilon (T_A^{*4} - T_I^{*4}) + \Pi C_A \Upsilon_T^2 \Upsilon_R G_s^*}{\bar{w} \rho_{nf} c_{p,nf} R}, \quad (6.2.21)$$

for an uncoated collector, and

$$T_O^* - T_I^* = \frac{2L \Pi \tau_{eff} \Upsilon_T^2 \Upsilon_R C_A G_s^*}{\bar{w} \rho_{nf} c_{p,nf} R}, \quad (6.2.22)$$

for a coated collector. The above expressions clearly indicate how the system parameters affect the temperature rise. For example, increasing the length leads to a linear increase in temperature, whilst increasing average velocity, density, specific heat and radius lead to a linear decrease. The affect of T_I^* is not so obvious since density and specific heat vary with T_I^* . Whilst the heat-mirror reduces the amount of radiative heat loss, (6.2.22) still decreases as T_I^* increases, due to the temperature-dependent thermophysical properties of Therminol[®] VP-1. For example, in Figure 6.3 the heat capacity of this base-fluid rises from $1.6 \times 10^6 \text{ J kg K}^{-1}$ at 30°C , to $2.1 \times 10^6 \text{ J kg K}^{-1}$ at 220°C , while the density of Therminol[®] VP-1 decreases from 1057 kg m^{-3} to 895 kg m^{-3} in the same interval. Since the heat capacity of Therminol[®] VP-1 rises by 40% and the density decreases by $\sim 17\%$, the change in heat capacity is more significant, so it takes more energy to raise the temperature of the nanofluid by one degree at 220°C than at 30°C .

The results of (6.2.21) and (6.2.22) are plotted in Figures 6.3a and 6.3b for the parameter values given in Tables 6.3 and 6.2. From these we see that with this set-up the uncoated NDAPSC (solid line) provides a greater increase when T_I^* is small enough such that

$$\epsilon (T_A^{*4} - T_I^{*4}) + \Pi \Upsilon_T^2 \Upsilon_R C_A G_s^* > \tau_{eff} \Pi \Upsilon_T^2 \Upsilon_R C_A G_s^*, \quad (6.2.23)$$

this inequality is given by (6.2.20). When the inlet temperature increases,

$$\sigma \epsilon (T_A^{*4} - T_I^{*4}) + \Pi \Upsilon_T^2 \Upsilon_R C_A G_s^* < \tau_{eff} \Upsilon_T^2 \Upsilon_R C_A \Pi G_s^*, \quad (6.2.24)$$

and so the coated NDAPSC works better. The critical inlet temperature required

for both the uncoated and coated collectors to perform equally, i.e.

$$\sigma\epsilon(T_A^{*4} - T_I^{*4}) + \Pi\Upsilon_T^2\Upsilon_R C_A G_s^* = \tau_{eff}\Pi\Upsilon_T^2\Upsilon_R C_A G_s^* \quad (6.2.25)$$

relies on f_v . More specifically, as f_v increases, so does the critical value for T_I^* ; when $f_v = 0$ the required inlet temperature is 88.9°C, and when $f_v = 0.006$ the required inlet temperature is 184.7°C. We also note from the magnitude of values on the y -axes of Figures 6.3a and 6.3b that the nanofluid based solar collector has a much larger temperature increase than the pure base-fluid based collector. Figure 6.3c plots the outlet temperature versus the inlet temperature for an uncoated NDAPSC (solid lines) and an NDAPSC coated with a heat-mirror (dashed lines) and with $f_v = 0$. We note from (6.2.14) that the outlet temperature scales linearly with the inlet temperature for the coated receiver and this behaviour is also observed in Figure 6.3c. Meanwhile, the relationship between the uncoated receiver's outlet temperature and inlet temperature is given by (6.2.12), a fourth degree polynomial. Like Figure 6.3b, in Figure 6.3c when $f_v = 0$ both collectors perform the same at an inlet temperature of 88.9°C.

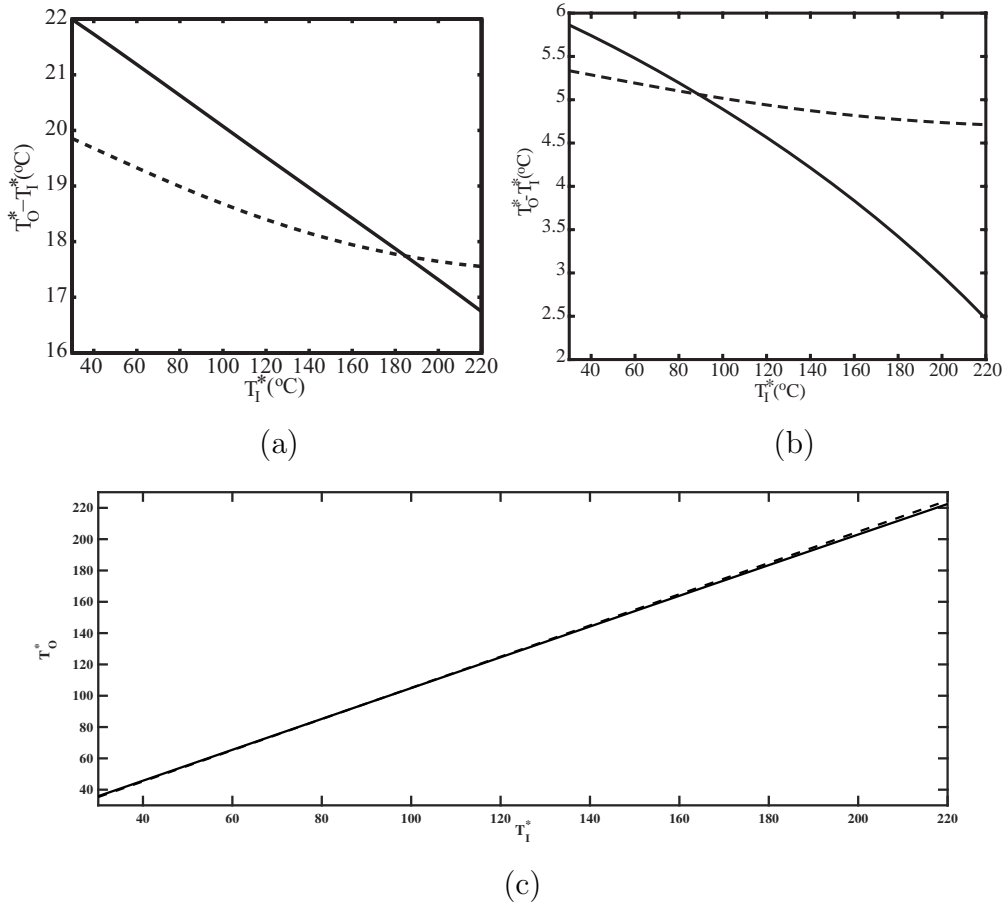


Figure 6.3: Net change in nanofluid temperature ($T_O^* - T_I^*$) versus inlet temperature for an uncoated NDAPSC (solid lines) and an NDAPSC coated with a heat-mirror (dashed lines), (a) $f_v = 0.006$, and (b) $f_v = 0$. (c) Outlet temperature versus inlet temperature for $f_v = 0$.

Expressions (6.2.16) and (6.2.17) allow us to vary different parameters to see how they affect NDAPSC efficiency. The coated receiver performs well at higher temperatures, but at lower temperatures the uncoated receiver is superior. Figure 6.4 shows that η , much like the net temperature rise, depends strongly on f_v . An initial rise in the nanoparticle concentration results in a large increase in η but these initial efficiency enhancements subside shortly thereafter. Our results show that an increase in f_v does not correspond to an increase in η after the nanofluid has absorbed all of the available solar radiation (i.e., $\Pi = 1$). Also, the inlet temperature does not affect η_c ; an NDAPSC coated with a heat-mirror performs the same across all of the inlet temperatures in this case study, so the efficiency of coated NSAPSC shown in Figure 6.4 is representative of η_c at all three operating temperatures. We note that at much higher operating temperatures

φ and τ become too large to neglect, and so we would observe some significant temperature dependence to η_c —although, we do not consider such high operating temperatures in this case study. Also, γ and τ^4 , increase linearly with ϵ , making them too large to neglect when the emissivity is sufficiently large. In reality, the emissivity of a heat-mirror is not constant across all temperatures and so it is likely that η_c varies across different operating temperatures. Whilst the spectral distribution of Black-body radiation shifts towards shorter wavelengths at higher operating temperatures, we do not have data on the spectral-dependence of Heat-mirror 1’s optical properties; therefore, we cannot reasonably determine a temperature-dependence for ϵ_{eff} in this case study. However, a temperature-dependent effective emissivity can be added to the current model by assuming $T_{Bb}^* = T_I^*$, i.e., $\epsilon_{eff}(T_{Bb}^*) = \epsilon_{eff}(T_I^*)$ —recall, we apply a similar method when calculating the thermophysical properties of the base-fluid.

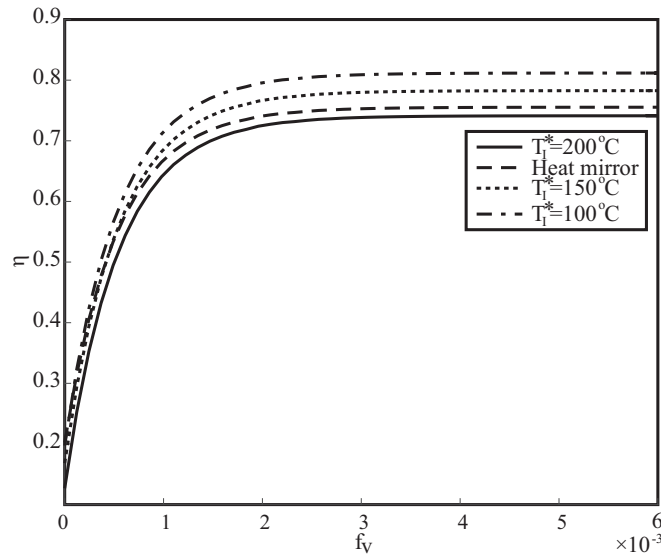


Figure 6.4: Overall efficiency versus particle volume fraction for different inlet temperatures.

The concentration ratio, C_A , is inversely proportional to the radius of the cylindrical receiver and directly proportional to the aperture width. In Figures 6.5a and 6.5b we alter the aperture width to present the relationship between C_A and η . The concentration ratio is an important factor in η_u ; however, it does not have any affect on η_c . The efficiency of the uncoated collector initially increases rapidly with C_A before this rate of increase decreases. At higher concentration ratios the uncoated collector becomes more efficient than the coated collector, but

the concentration ratio at which it becomes more efficient gets larger at higher operating temperatures. Efficiency is defined as the ratio of net energy increase across the system to incident solar energy. At leading order the energy leaving the system due to thermal heat loss is constant, depending on the inlet temperature rather than the net temperature rise. Thus, at leading order, heat leaves the system at the same rate regardless of C_A so one would expect the efficiency to increase with C_A , as the energy entering the system becomes much larger than the energy out of the system. A receiver coated with a heat-mirror has no thermal heat losses at leading order and so we would not expect its efficiency to vary with C_A .

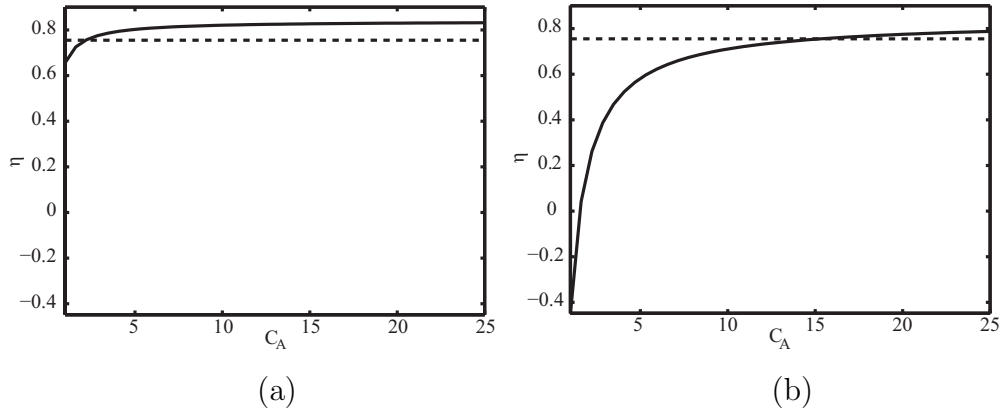


Figure 6.5: Overall efficiency versus concentration ratio for an uncoated receiver (solid lines) and a coated receiver (dashed lines). We alter the aperture width and fix the pipe diameter to vary C_A for (a) $T_I^* = 50^\circ\text{C}$ and (b) $T_I^* = 150^\circ\text{C}$, $f_v = 0.006$.

In Figures 6.6a and 6.6b, we examine the relationship between C_A , f_v and $(1 + \gamma - \tau^4)/\tau_{eff}$, the left-hand side of the inequality given by (6.2.19). We note that an increase in f_v shifts the curves such that they initially grow faster in both Figures 6.6a and 6.6b. As f_v gets larger, $\Pi \rightarrow 1$ (where Π is defined in (6.2.5)); when all of the incoming solar radiation at $r^* = R$ gets attenuated into the nanofluid, $\Pi = 1$. An uncoated NDAPSC is a better design option at a lower C_A and as f_v (or Π) increases because the $\sigma\epsilon(T_A^{*4} - T_I^{*4})$ term becomes less dominant in (6.2.20). Furthermore, an uncoated NDAPSC is more efficient than a coated NDAPSC at lower concentration ratios when the inlet temperature is lower. The fraction rises quicker with C_A in Figure 6.6a than it does in Figure 6.6b, and so they cross the crucial threshold where $(1 + \gamma - \tau^4)/\tau_{eff} = 1$ at lower concentration ratios.

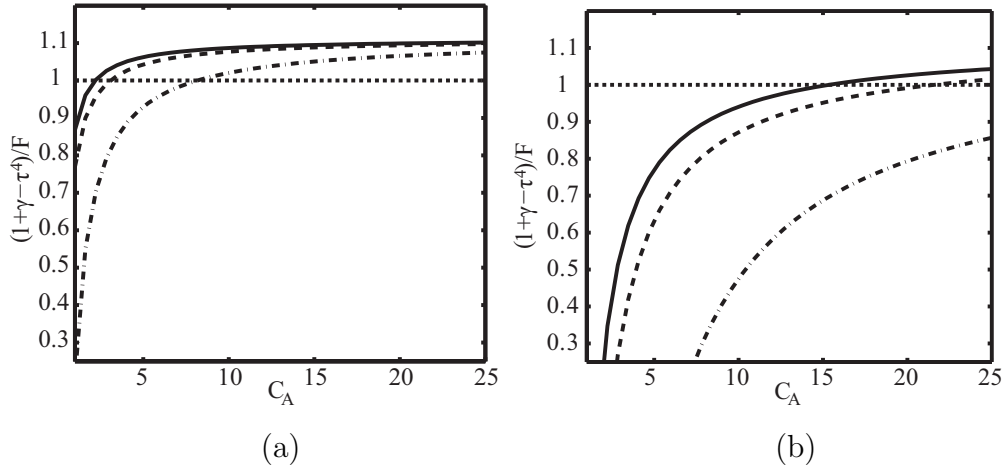


Figure 6.6: The expression $(1 + \gamma - \tau^4) / \tau_{eff}$ versus concentration ratio for $f_v = 0.0006$ (solid lines), $f_v = 0.0005$ (dashed lines), and $f_v = 0$ (dot dashed lines). (a) $T_I^* = 50^\circ\text{C}$ and (b) $T_I^* = 50^\circ\text{C}$.

6.3 Summary and discussion

In this chapter we develop an approximate analytic solution to a three-dimensional model for the efficiency of an NDAPSC. The model consists of a system of partial differential equations describing the conservation of mass, momentum, and energy. We obtain a heat source term via the radial flux integral. The model is written in nondimensional form to show that there are four controlling nondimensional groups. We use a specific case study described in [29], to evaluate the relative importance of these nondimensional subgroups under realistic physical conditions. The model is then reduced using asymptotic arguments, and solved analytically to investigate the efficiency of the collector subject to variation in model parameters. Further analysis of the collector efficiency leads to an inequality which determines the viability of including a heat-mirror in the collector.

In this chapter, we developed a model to determine the temperature variation in a concentrating nanofluid-based direct absorption parabolic trough solar collector under a turbulent flow regime. The model includes radiative transport and energy equations. We obtain a leading order approximate analytic solution to the model via a power law approximation for the solution to the radiative transport equation. In contrast to previous studies on NDAPSCs which require a numerical solution [29, 38, 42], we found an approximate analytical solution.

This has the distinct advantage that we can clearly see exactly how the system parameters affect the efficiency.

We expressed the system in nondimensional form to show that there are four controlling nondimensional numbers, specifically two describing the heat source, one describing the relative importance of conduction and advection and three representing the heat loss to the surroundings. Following an asymptotic analysis, we showed that two of the nondimensional numbers have a much lesser impact on the performance of the solar collector and we ignored their effects to obtain a leading order approximation of the system. One of these small dimensionless parameters, $1/Pe$, represents the ratio between thermal diffusion and advection in the downstream direction. Neglecting the second small dimensionless parameter, φ , allowed us to approximate the radiative heat loss in the solar collector with a Black-body radiation calculation of a body at the inlet temperature—at leading order, an NDAPSC loses heat at a constant rate of $\sigma\epsilon T_I^4$. By examining the non-dimensional system we were able to eliminate negligible terms and so determine that the temperature increases almost linearly along the pipe. This has previously been observed both numerically and via experiments [42].

Previous research has suggested that coating improves efficiency [28, 38, 59]. Our results show that this is not always the case: for lower temperatures an uncoated system is more efficient. We provided an equality to determine when coating is appropriate. We used this inequality to show that as the solar concentration ratio increases, an uncoated NDAPSC becomes more efficient than an NDAPSC coated with a heat-mirror; at higher inlet temperatures, the concentration ratio required for an uncoated NDAPSC to be more efficient than a coated NDAPSC increases. Whilst there are existing frameworks for assessing a heat-mirror’s performance, this inequality does not appear anywhere else in the literature and should be considered extremely informative for NDAPSC design.

In reality, the emissivity of a heat-mirror is not constant across all temperatures; however, existing research around the temperature-sensitivity of an Sn-doped In_2O_3 heat-mirrors’ optical properties is limited. As our understanding of heat-mirrors grows, the accuracy of this model can be improved further by adding an appropriate temperature-dependence to the heat-mirrors’ emissivity. A temperature-dependent effective emissivity could be easily added to the current model by assuming $T_{Bb}^* = T_I^*$; we already adapt a similar method to this when we calculate the thermophysical properties of the base-fluid. However, if $\epsilon_{eff}(T_I^*)$

6. COLLECTOR 5: A LARGE CONCENTRATING NDAPSC

is a bad approximation for $\epsilon_{eff}(T_{Bb}^*)$ this method would fail to accurately predict the true efficiency of an NDAPSC, and a different modelling approach would be required.

CHAPTER 7

COLLECTOR 6: TIME-DEPENDENCE IN A LARGE CONCENTRATING NDAPSC

7.1 Introduction

In previous chapters we assumed that the heat source was constant across time; however, in reality, the solar intensity at a fixed position on Earth is constantly changing due to the rotation of the Earth, i.e., the time of day, the orbit of the Earth around the sun, i.e., the season, and dynamic cloud cover [30]. Two of these effects are depicted in Figure 7.1. When the sun is lower in the sky incoming radiation must pass through more of the atmosphere before it gets to the solar collector, and so the radiative intensity at the surface of the receiver is reduced. On Earth, clouds (which are usually an aerosol of water vapour and air) are much better at absorbing solar radiation than pure air; as a result, when clouds pass between a solar collector and the sun, the solar intensity at the surface of the collector is reduced. Cloud cover and the rotation of the Earth operate at different time-scales. In this chapter we explore the effect that both of these phenomenon have on collector performance.

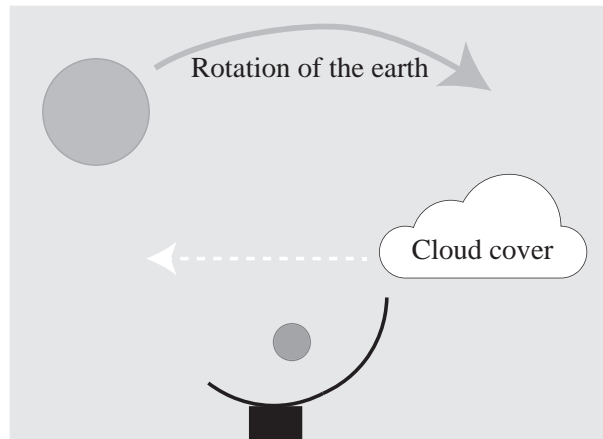


Figure 7.1: Rotation of the Earth and cloud cover affect solar intensity.

Surface-based parabolic trough solar collectors usually consist of a working fluid flowing through metallic pipes. These pipes expand as they are heated, and this expansion process produces mechanical strains. Kolb [31] notes how a solar collector must, by its nature, operate cyclically, i.e., the receiver is heated to operating temperature when it is initiated, and allowed to relax to thermal equilibrium once it ceases operation; furthermore, rapidly varying cloud cover produces temperature fluctuations in the system. NDAPSCs also experience fluctuating operating temperatures; however, this effect has not been studied in the literature.

We begin modelling Collector 6 as a three-dimensional cylindrical pipe under turbulent flow. In Section 7.2.2 we model the time-dependent conservation of energy in the system. Time-dependence is introduced into this model via the source term; we give two possible examples of source terms operating on different time-scales in Section 7.2.3. The first time-dependent source term represents dynamic cloud cover, and the second represents a variation of solar intensity over the course of a day. We rescale and non-dimensionalise the model in Section 7.2.4 before applying sensible parameter values to the model in Section 7.2.5. In Section 7.2.6 we obtain an analytic expression for the temperature in the system by solving for the temperature in the conservation of energy. We use this analytic temperature profile to discuss the performance of Collector 6 in Sections 7.2.8 and 7.3.

7.2 Model

7.2.1 Introduction

In this chapter we apply the same cylindrical coordinate system that was used in Chapters 5 and 6 to model an NDAPSC. Figure 7.2b shows the system geometry in more detail; we recall, (x^*, r^*, ϕ) define a three-dimensional cylindrical coordinate system such that x^* is the axial coordinate, r^* is the radial coordinate and ϕ is the angle highlighted (where $*$ denotes a dimensional variable). Again, like in previous chapters, the nanofluid enters the receiver at the inlet ($x^* = 0$), it is heated as it absorbs solar radiation and exits the receiver at the outlet ($x^* = L$).

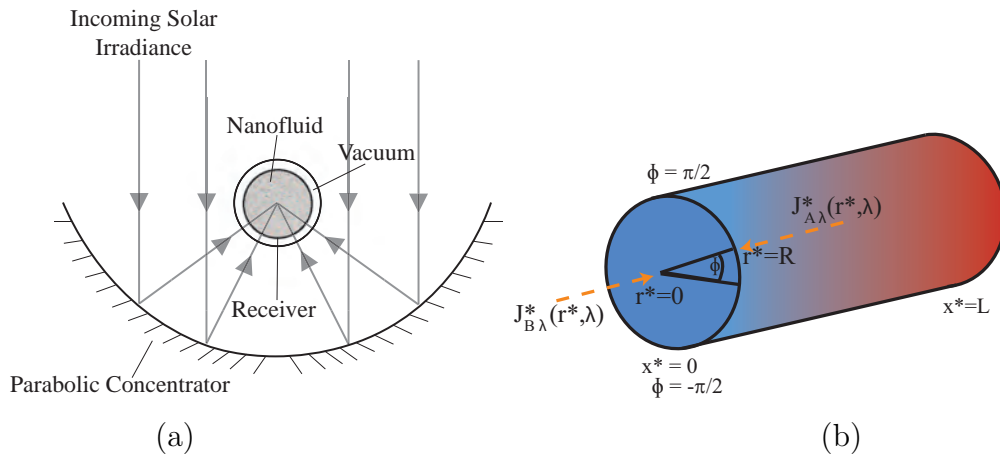


Figure 7.2: (a) Cross section of NDAPSC with length L and receiver with radius R , and (b) receiver geometry.

7.2.2 Conservation of energy

The equation describing the conservation of heat energy is similar to (6.2.1) except the source term is time-dependent and so we no longer only consider the steady state:

$$\rho_{nf} c_{p,nf} [T_{t^*}^* + \mathbf{u} \cdot \nabla T^*] = k_{nf} \nabla^2 T^* + q, \quad (7.2.1)$$

where we recall, ρ_{nf} is the nanofluid density, $c_{p,nf}$ is the nanofluid heat capacity, k_{nf} is the nanofluid thermal conductivity, $\mathbf{u} = (u^*, w^*, v^*)$, $T^*(x^*, r^*, \phi, t^*)$ is the fluid temperature, and $q = q^*(r^*, \phi, t^*)$. The nanofluid's temperature has an initial condition of $T^*|_{t^*=0} = g^*(x^*)$, where $g^*(x^*)$ is some known function of x^* , and an inlet condition of $T^*|_{x^*=0} = f^*(t^*)$ where $f^*(t^*)$ is some known function of t^* . At the surface of the receiver there is no slip, and thus $\mathbf{u} = 0$ when $r^* = R$.

The radiative boundary condition at the surface of the receiver is

$$T_{r^*}^*|_{r^*=R} = \frac{\sigma\epsilon}{k_{nf}} (T_A^{*4} - T^{*4}|_{r^*=R}), \quad (7.2.2)$$

where we recall from previous chapters, σ is Stefan's constant, ϵ the emissivity constant, and T_A^* the ambient temperature. The outlet condition is

$$\left. \frac{\partial T^*}{\partial x^*} \right|_{x^*=L} = 0. \quad (7.2.3)$$

In Chapter 6 we noted that since the flow is turbulent, the temperature in the receiver's cross section is approximately constant, i.e., $T^*(x^*, r^*, \phi, t^*) \simeq T^*(x^*, t^*)$. We reduce (7.2.1) following the simplification method outlined in Chapter 6: the terms in (7.2.1) are integrated over the cross section to obtain the one-dimensional model

$$\begin{aligned} \frac{R^2}{2} T_{t^*}^* + \frac{R^2}{2} \bar{u}^* T_{x^*}^* &= \frac{k_{nf}}{\rho_{nf} c_{p,nf}} \left(\frac{R^2}{2} T_{x^* x^*}^* + R T_{r^*}^*|_{r^*=R} \right) \\ &+ \frac{1}{\rho_{nf} c_{p,nf}} \int_0^R \int_{-\pi/2}^{\pi/2} r^* q^*(r^*, \phi, t^*) dr^* d\phi. \end{aligned} \quad (7.2.4)$$

We use the source term proposed in Chapter 5, however, here we include time-dependence and so

$$q(r^*, \phi, t^*) = \frac{\beta_0 \beta_1}{2r^*} \left(\frac{G_{s,1}^*(\phi, t^*)}{\left(1 + \frac{\beta_0}{2R} (R - r^*)\right)^{\beta_1+1}} + \frac{G_{s,2}^*(\phi, t^*)}{\left(1 + \frac{\beta_0}{2R} (R + r^*)\right)^{\beta_1+1}} \right), \quad (7.2.5)$$

where we recall that β_0 and β_1 are the dimensionless fitting parameters which were first introduced by Cregan and Myers [10] to approximate the source term in a parallel-plate nanofluid-based direct absorption solar collector. The $1/r^*$ term in (7.2.5) describes the concentration of incoming solar radiation as it gets closer to the parabolic reflector's focal line, the power-law terms are a result of the incoming and outgoing solar radiative intensity decaying as it gets absorbed into the nanofluid, while the ϕ -dependent functions are given by

$$G_{s,1}^*(\phi, t^*) = \begin{cases} 0 & \text{if } \phi > \phi_{\text{crit}} \\ \frac{G_s^*(t^*) 2f}{R} \frac{1}{1 - \sin \phi} & \text{if } \phi \leq \phi_{\text{crit}}, \end{cases} \quad (7.2.6)$$

and

$$G_{s,2}^*(\phi, t^*) = \begin{cases} 0 & \text{if } \phi < -\phi_{\text{crit}} \\ \frac{G_s(t^*)2f}{R} \frac{1}{1-\sin(-\phi)} & \text{if } \phi \geq -\phi_{\text{crit}}, \end{cases} \quad (7.2.7)$$

where $G_s^*(t^*)$ is the solar intensity at the aperture, ϕ_{crit} is the maximum angle of incoming reflected solar radiation, and f is the focal length of the parabolic reflector. The critical angle, ϕ_{crit} , is limited by the width of the reflector, W , and is defined by

$$\phi_{\text{crit}} = \arctan \left[\frac{(W/2)^2 - 4f^2}{2fW} \right]. \quad (7.2.8)$$

Thus, we rewrite (7.2.4) yielding

$$\frac{R^2}{2} (T_{t^*}^* + \bar{u}^* T_{x^*}^*) = \frac{k_{nf}}{\rho_{nf} c_{p,nf}} \left(\frac{R^2}{2} T_{x^* x^*}^* + \frac{R\sigma\epsilon}{k_{nf}} (T_A^{*4} - T^{*4}) \right) + \frac{\Pi R \Upsilon_T^2 \Upsilon_R C_A G_s^*(t^*)}{\rho_{nf} c_{p,nf}}, \quad (7.2.9)$$

where we recall that Π is the overall fraction of absorbed radiation as it passes through the cross section.

7.2.3 Heat source terms

In this section we propose two realistic time-dependent examples of the solar intensity at the aperture, $G_s^*(t^*)$. Scenario 1 models when a cloud passes over the receiver leading to a sharp decrease in solar intensity, while Scenario 2 models the slower variation of solar intensity over the course of a day. Even though this paper primarily discusses these two scenarios, we emphasise that the solution method in Section 7.2.6 is independent of $G_s^*(t^*)$, and so the model is easily extended to incorporate alternative time-dependent representations of solar intensity.

In Scenario 1, when a cloud covers the receiver, we presume an instantaneous drop in solar intensity. This is modelled as

$$G_s^*(t^*) = G_m^* (1 - 0.5H(t^* - t_c^*)), \quad (7.2.10)$$

where G_m^* is the maximum solar intensity at the aperture, $H(\cdot)$ is the Heaviside step function, and t_c^* is the time when the cloud shades the collector. In the case of Scenario 2 we use three weeks of minute by minute data on incoming solar radiation beginning on 1st June 2015 from the University of Oregon's Solar

Radiation Monitoring Laboratory [64]. The mean solar irradiation at each time of the day is obtained by averaging across all 21 days in the database (dot-dashed grey line in Figure 7.3). The data is approximated via

$$G_s^*(t^*) = G_m^* e^{-A\left(\frac{\bar{u}}{L}t^* - B\right)^2}, \quad (7.2.11)$$

where the parameters: $G_m^* = 849.4 \text{ W m}^{-2}$, $A = 2.595 \times 10^{-5}$, and $B = 492.49$ are obtained via a least-squares fitting routine in Matlab. The associated standard error score is 34.96 W m^{-2} . Figure 7.3 compares the fitted function (black line) to the data (dot-dashed grey line). In general, the experimental data and the fitted function match well: as expected, the solar intensity gradually increases in the morning until midday before gradually decreasing for the rest of the day.

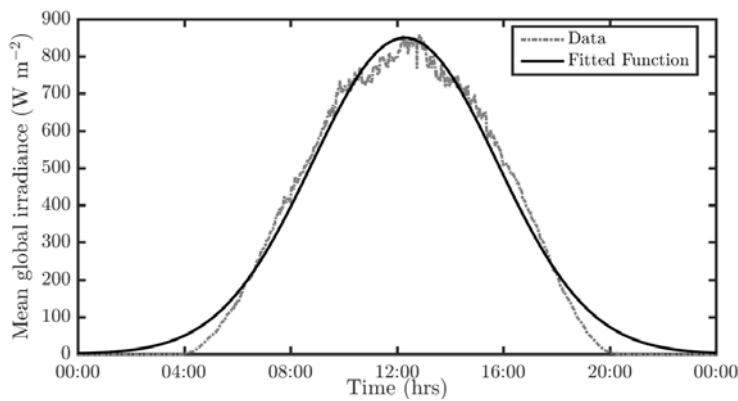


Figure 7.3: Experimentally observed incoming radiative intensity [64] (dot-dashed grey line) and approximated incoming radiative intensity (black line) over the course of a day.

7.2.4 Dimensional analysis

We define the dimensionless variables

$$x^* = lx, \quad t^* = \frac{l}{\bar{u}^*}t, \quad f^*(t^*) = T_I^* + \Delta T f(t), \quad (7.2.12)$$

$$g^*(x^*) = T_I^* + \Delta T g(x), \quad T^* = T_I^* + \Delta T T, \quad G_s^*(t^*) = G_m^* G_s(t),$$

where T_I^* is the average inlet temperature and

$$\Delta T = \frac{2\Pi\Upsilon_T^2\Upsilon_R C_A G_m^* L}{\bar{u}^* \rho_n f c_{p,nf} R}, \quad (7.2.13)$$

is chosen since the source term is driving the temperature variation. Non-dimensionalising (7.2.9) yields

$$T_t + T_x = \frac{1}{\text{Pe}} T_{xx} + \gamma + G_s(t) - (\tau + \varphi T)^4, \quad (7.2.14)$$

where the dimensionless parameters are

$$\text{Pe} = \frac{\rho_{nf} c_{p,nf} l \bar{u}^*}{k_{nf}}, \quad \gamma = \frac{\sigma \epsilon T_A^{*4}}{\Pi \Upsilon_T^2 \Upsilon_R C_A G_m^*}, \quad \tau = \frac{\gamma^{1/4} T_I^*}{T_A^*}, \quad \varphi = \frac{\gamma^{1/4} \Delta T}{T_A^*}. \quad (7.2.15)$$

These dimensionless parameters are equivalent to those obtained in Chapter 6, i.e., the Peclet number, Pe , is a well-known dimensionless number describing the ratio of advection to thermal diffusion, while γ , τ^4 , and φ^4 describe the relative magnitude of black-body emissions. The dimensionless initial, inlet and outlet conditions are: $T|_{t=0} = g(x)$, $T|_{x=0} = f(t)$, and $T_x|_{x=1} = 0$.

7.2.5 Case study

As a case study for exploring our model further, we consider an Aluminum and Therminol[®] VP-1 nanofluid and, unless otherwise stated, we use the parameter values given in the case study described in Chapter 6. We remind the reader that in the last chapter we compared the performance of an NDAPSC coated with a heat-mirror to an NDAPSC not coated with a heat-mirror using a steady-state model. In Section 7.2.8 we use the time-dependent model to similarly compare the performance of these two NDAPSC design variations.

7.2.6 Solution method

This section explores the relative magnitudes of the dimensionless parameter values, $1/\text{Pe}$, γ , φ , and τ , with a view towards simplifying the dimensionless conservation of energy equation, (7.2.14). Table 7.1 provides values for these dimensionless parameters when T_I^* and f_v are varied in the case study from Section 7.2.5. From this table, we see that $1/\text{Pe}$ ranges between 3×10^{-8} and 5×10^{-8} while φ is $O(10^{-2})$. Consequently, we may neglect terms including $1/\text{Pe}$, and φ , and approximate (7.2.14) via

$$T_t + T_x = G_s(t) + \gamma - \tau^4. \quad (7.2.16)$$

7. COLLECTOR 6: TIME-DEPENDENCE IN A LARGE CONCENTRATING NDAPSC

Recall, this model has the generic initial and inlet conditions $T|_{t=0} = g(x)$, and $T|_{x=0} = f(t)$. We note that neglecting $1/\text{Pe}$ and φ results in errors $\sim 10^{-6}\%$ and $\sim 1\%$ respectively. Furthermore, we recall from previous chapters that neglecting the $1/\text{Pe} T_{xx}$ term results in the boundary layer at $x^* = L$ being ignored, therefore in this approximated model, the boundary condition at $x^* = L$ cannot be satisfied.

	$T_I^* = 25\text{ }^\circ\text{C}$	$T_I^* = 100\text{ }^\circ\text{C}$	$T_I^* = 200\text{ }^\circ\text{C}$
$1/\text{Pe}$	$(0.4316, 0.4215, 0.4366) \times 10^{-7}$	$(0.3804, 0.3716, 0.3848) \times 10^{-7}$	$(0.3204, 0.3129, 0.3241) \times 10^{-7}$
γ	$(0.0738, 0.0278, 0.0198)$	$(0.0738, 0.0278, 0.0198)$	$(0.0738, 0.0278, 0.0198)$
φ	$(0.0108, 0.0225, 0.0289)$	$(0.0109, 0.0227, 0.0293)$	$(0.0103, 0.0215, 0.0277)$
τ^4	$(0.0789, 0.0297, 0.0212)$	$(0.1747, 0.0658, 0.0468)$	$(0.4517, 0.1701, 0.1210)$

Table 7.1: Dimensionless parameter values for an uncoated solar collector for varying input temperatures for three different particle volume fractions ($f_v = 0$, $f_v = 0.0005$, $f_v = 0.006$).

Since (7.2.16) is a first-order linear partial differential equation, one can apply the inlet and initial conditions to obtain an analytic solution to (7.2.16) via the method of characteristics:

$$T(x, t) = \begin{cases} \int_0^t G_s(s) ds + (\gamma - \tau^4)t + g(x - t) & \text{if } 0 < x - t \leq 1 \\ \int_{t-x}^t G_s(s) ds + (\gamma - \tau^4)x + f(t - x) & \text{if } t > x. \end{cases} \quad (7.2.17)$$

This generalised model is valuable as it can be applied to any time-dependent source term, and any initial and inlet conditions. However, in the specific context of Scenario 1, $G_s(\cdot)$ is obtained after nondimensionalising (7.2.10), the inlet condition is given by $T(x = 0) = 0$ (following the case-studies from previous chapters), and the initial condition is given by $g(x) = (1 + \gamma - \tau^4)x$ (note that this initial condition is chosen on an arbitrary basis so that the solar collector is at an approximate steady state when $t = 0$). Therefore, in this scenario (7.2.17) has a particular solution of the form

$$T(x, t) = \begin{cases} (1 + \gamma - \tau^4)x & \text{if } t < t_c \\ (1 + \gamma - \tau^4)x - 1/2(t - t_c) & \text{if } t_c \leq t \leq x + t_c \\ (1/2 + \gamma - \tau^4)x & \text{if } t > x + t_c. \end{cases} \quad (7.2.18)$$

Meanwhile, in the specific context of Scenario 2, $G_s(\cdot)$ is obtained after nondimensionalising (7.2.11), the inlet boundary condition is again given by $T(x = 0) = 0$, and the initial condition is given by:

$$g(x) = \frac{\sqrt{\pi}}{2\sqrt{A}} \left[\operatorname{erf}(\sqrt{AB}) + \operatorname{erf}(\sqrt{A}(B+x)) \right] + (\gamma - \tau^4)x, \quad (7.2.19)$$

where $\operatorname{erf}(\cdot)$ is the error function. Again, this initial condition is chosen on an arbitrary basis, in fact further asymptotic analysis (see Appendix D) shows that the initial condition has a negligible impact on our analysis since the time-scales of interest in this Scenario are much longer than the time it takes for the initial nanofluid to flow out of the system. So, (7.2.17) has an exact solution of the form

$$T(x, t) = \frac{\sqrt{\pi}}{2\sqrt{A}} \left[\operatorname{erf}(\sqrt{A}(B-t)) + \operatorname{erf}(\sqrt{A}(B+x-t)) \right] + (\gamma - \tau^4)x \quad (7.2.20)$$

for Scenario 2, but the supplementary asymptotic analysis in Appendix D shows that (7.2.20) is approximately equivalent to the simpler analytic expression:

$$T(x, t) = (G_s(t) + \gamma - \tau^4)x. \quad (7.2.21)$$

Note that in Section 7.2.8 we sometimes refer to (7.2.21) rather than (7.2.20) because (7.2.21) is simpler and easier to interpret—for example, when $G_s(t) > \gamma - \tau^4$, $T_O^* > T_I^*$, and when $G_s(t) < \gamma - \tau^4$, $T_O^* < T_I^*$.

7.2.7 Efficiency

Duffie and Beckman [12] define the instantaneous collector efficiency, $\eta_t(t^*)$, as the ratio of usable thermal energy to incident solar energy, i.e.,

$$\eta_t(t^*) = \frac{\rho_{nf} c_{p,nf} \bar{u}^* \pi R^2 (T^*(L, t) - T_I^*)}{G_s^*(t^*) LC_A 2\pi R}. \quad (7.2.22)$$

However, this definition is not appropriate in the case of a time-dependent model because (7.2.22) merely offers a snapshot of the efficiency at one particular point in time and so it does not necessarily reflect a collector's overall operating efficiency. We define the overall efficiency of this solar collector during a specific time interval, as the ratio of the net amount of energy that exits the system to

the overall amount of incoming radiation entering the system during that period, i.e.,

$$\eta = \frac{E_o^*}{LC_A 2\pi R \int_0^{t_m^*} G_s^*(t^*) dt^*}, \quad (7.2.23)$$

where E_o^* is the overall amount of energy that exits the system during the time interval $0 \leq t^* \leq t_m^*$, i.e.,

$$E_o^* = \int_0^{t_m^*} \rho_{nf} c_{p,nf} \bar{u}^* \pi R^2 (T^*(L, t) - T_I^*) dt^*. \quad (7.2.24)$$

We arbitrarily choose t_m^* such that in Scenario 1, $t_m^* = 135$ s (i.e., $4\bar{u}^*/L$), and in Scenario 2 $t_m^* = 86\,400$ s (i.e., one day). Also, in Scenario 1 we arbitrarily choose $t_c^* = t_m^*/2$.

7.2.8 Results

This section uses a parameter space exploration based around the values from Tables 6.1 and 6.2 to compare various aspects of a collector's performance. No previous study has sought to question how time-dependence in the incoming radiative intensity would affect the performance of an industrial-scale NDAPSC. Therefore, in this section we are unable to make direct comparisons to previous literature, however, we do make indirect comparisons where possible. Figure 7.4 shows the piecewise temperature profile for Scenario 1 (i.e., cloud cover), as calculated by (7.2.18). Initially, when $t^* < t_c^*$, the temperature of the nanofluid is in steady-state. In this region, T^* increases linearly as the nanofluid flows through the collector. At t_c^* , the incoming solar intensity decreases instantaneously due to cloud cover and the nanofluid's temperature profile enters into a period of rapid transition where $\partial T^*/\partial t^* \neq 0$ (i.e., when $t_c^* \leq t^* \leq x^*/\bar{u}^* + t_c^*$) and the nanofluid's temperature decreases linearly with time. Even though time-dependent event is instantaneous, the nanofluid's temperature at the outlet does not reach a steady-state until 34 s after t_c^* . We note that a steady-state model would not capture the nanofluid's temperature accurately in this region, thus emphasising the value of the time-dependent model for real-world applications where the solar intensity is constantly changing. After this transitional period, (i.e., when $t^* > x^*/\bar{u}^* + t_c^*$) the temperature profile enters a new linear steady-state regime.

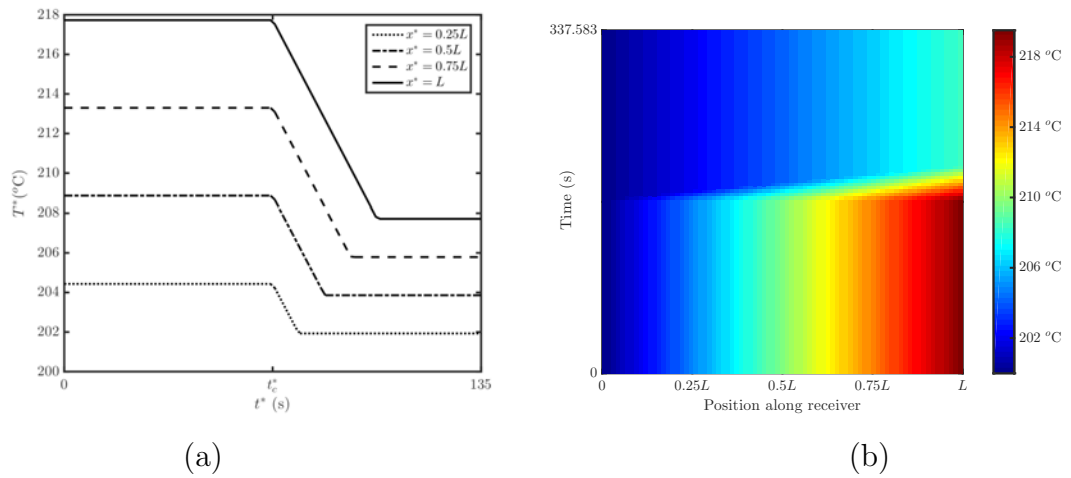


Figure 7.4: Temperature along the receiver over time in Scenario 1 for $f_v = 0.006$ and $T_I = 200$ °C.

Figure 7.5 shows the temperature versus time of day at five different positions along the collector for Scenario 2, when $f_v = 0.006$ and $T_I = 200$ °C. The nanofluid's temperature falls/rises approximately linearly as it flows through the receiver, however, the gradient of this temperature decrease/increase varies throughout the day. As expected, the solar collector's outlet temperature, $T^*(x^* = L)$, increases with increasing radiative intensity and decreases with decreasing radiative intensity. From 06:40 pm to 05:20 am the solar collector loses heat because incoming radiation is too small to overcome thermal losses, i.e., $G_s(t) + \gamma < \tau^4$. This inequality (which comes from (7.2.21)), is extremely useful as it allows an NDAPSC's daily operation cycle to be informed by weather forecasts. When $G_s(t) + \gamma > \tau^4$ (i.e., from 05:20 am to 06:40 pm), incoming radiation overcomes thermal losses and the nanofluid heats up as it flows through the receiver; an NDAPSC should only be operational during such circumstances.

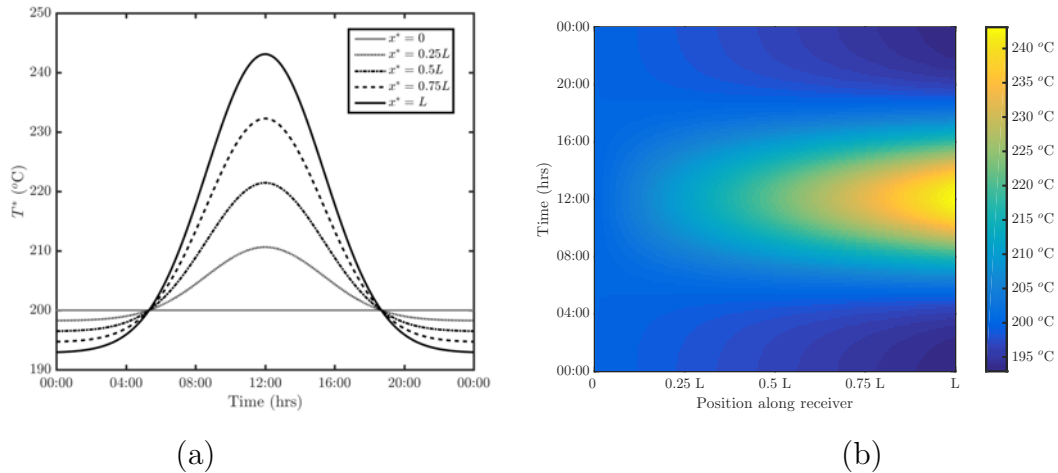


Figure 7.5: Scenario 2: Temperature along the receiver across the day for $f_v = 0.006$ and $T_I = 200$ °C.

Figure 7.6 shows the instantaneous efficiency $\eta_t(t^*)$ versus time for $T_I^* = 200$ °C (solid lines), $T_I^* = 150$ °C (dotted lines), $T_I^* = 100$ °C (dot dashed lines), and a heat-mirror coated NDAPSC when $T_I^* = 150$ °C (dashed lines) for (a) Scenario 1 and (b) Scenario 2. This figure demonstrates why an instantaneous measure of efficiency may be misleading. In Scenario 1, the instantaneous efficiency is initially at a steady-state, however, it spikes at $t^* = t_c^*$ reaching values greater than 1. This non-physical result ($\eta > 1$) occurs because the instantaneous efficiency is ill-defined for time-dependent incoming solar intensity. We remind the reader that Duffie and Beckman [12] define $\eta_t(t^*)$ as the ratio of usable thermal energy to incident solar energy. At $t^* = t_c^*$, the incident solar energy decreases instantaneously, however the nanofluid at the collector’s outlet was heated by the previous elevated solar intensity value. After $t^* = t_c^*$, the efficiency values decrease before reaching a new steady-state when all of the nanofluid that had been heated by the larger solar intensity has flown out of the system. The initial steady-state efficiency (when $G_s^*(t^*) = G_m^*$) is larger than the new steady-state efficiency (when $G_s^*(t^*) = G_m^*/2$) across all inlet temperatures—the collector is less efficient when the intensity of incoming solar radiation is reduced. Although we note in both scenarios that the NDAPSC coated by the heat-mirror emits much less black-body radiation and hence its steady-state instantaneous efficiency is not very sensitive to the changes in $G_s^*(t^*)$. In Scenario 2 we note that the uncoated collectors have negative instantaneous efficiency scores when the intensity

of the incoming solar radiation is too low and $\tau^4 > \gamma + G_s(t)$. Of course, these collectors would be switched off under such operating conditions.

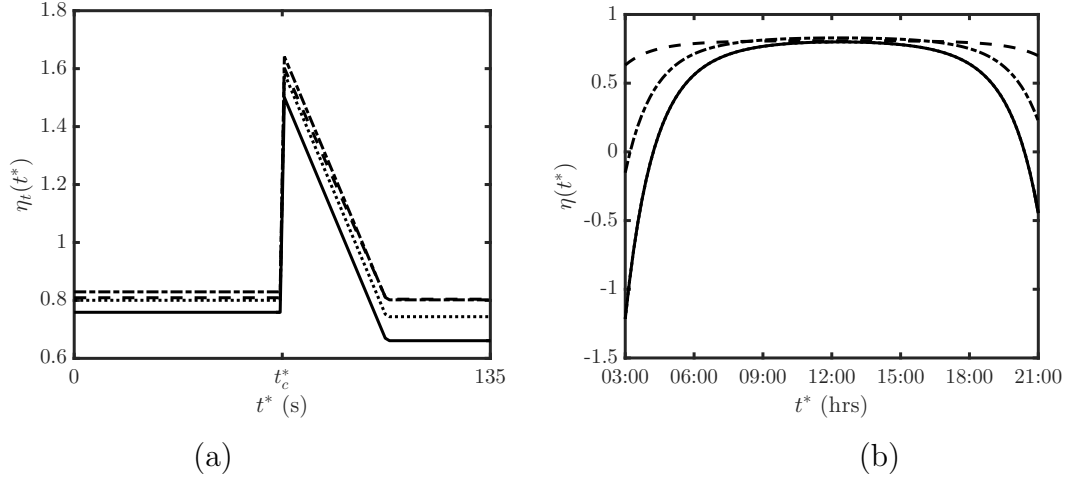


Figure 7.6: Instantaneous efficiency versus time for $T_I^* = 200^\circ\text{C}$ (solid lines), $T_I^* = 150^\circ\text{C}$ (dotted lines), $T_I^* = 100^\circ\text{C}$ (dot dashed lines), and a heat-mirror coated NDAPCS (dashed lines) for (a) Scenario 1 and (b) Scenario 2.

Figure 7.6 shows the instantaneous efficiency $\eta_t(t^*)$ versus time for $T_I^* = 200^\circ\text{C}$ (solid lines), $T_I^* = 150^\circ\text{C}$ (dotted lines), $T_I^* = 100^\circ\text{C}$ (dot dashed lines), and a heat-mirror coated NDAPCS when $T_I^* = 150^\circ\text{C}$ (dashed lines) for (a) Scenario 1 and (b) Scenario 2. This figure demonstrates why an instantaneous measure of efficiency may be misleading. In Scenario 1, the instantaneous efficiency is initially at a steady-state, however, it spikes at $t^* = t_c^*$ reaching values greater than 1. This non-physical result ($\eta > 1$) occurs because the instantaneous efficiency is ill-defined for time-dependent incoming solar intensity. We remind the reader that Duffie and Beckman [12] define $\eta_t(t^*)$ as the ratio of usable thermal energy to incident solar energy. At $t^* = t_c^*$, the incident solar energy decreases instantaneously, however the nanofluid at the collector's outlet was heated by the previous elevated solar intensity value. After $t^* = t_c^*$, the efficiency values decrease before reaching a new steady-state when all of the nanofluid that had been heated by the larger solar intensity has flowed out of the system. The initial steady-state efficiency (when $G_s^*(t^*) = G_m^*$) is larger than the new steady-state efficiency (when $G_s^*(t^*) = G_m^*/2$) across all inlet temperatures—the collector is less efficient when the intensity of incoming solar radiation is reduced. Although we note in both scenarios that the NDAPSC coated by the heat-mirror emits much

7. COLLECTOR 6: TIME-DEPENDENCE IN A LARGE CONCENTRATING NDAPSC

less black-body radiation and hence its steady-state instantaneous efficiency is not very sensitive to the changes in $G_s^*(t^*)$. In Scenario 2 we note that the uncoated collectors have negative instantaneous efficiency scores when the intensity of the incoming solar radiation is too low and $\tau^4 > \gamma + G_s(t)$. Of course, these collectors would be switched off under such operating conditions.

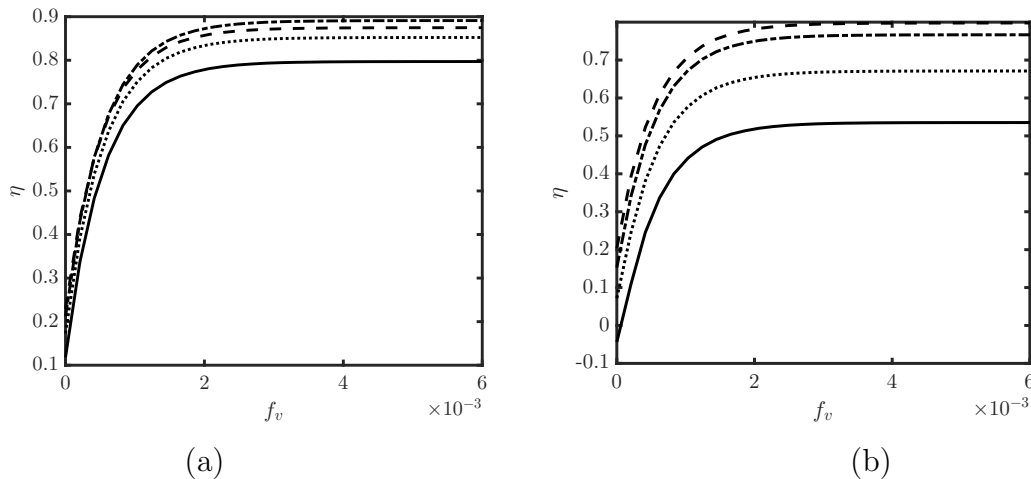


Figure 7.7: Overall efficiency versus particle volume fraction when $T_I^* = 200^\circ\text{C}$ (solid lines), $T_I^* = 150^\circ\text{C}$ (dotted lines), $T_I^* = 100^\circ\text{C}$ (dot dashed lines), and a heat-mirror coated NDAPSC (dashed lines) for (a) Scenario 1 and (b) Scenario 2.

Figure 7.8 shows the overall collector efficiency versus inlet temperature of an uncoated NDAPSC (solid lines), and a heat-mirror coated NDAPSC (dashed lines) for (a) Scenario 1 and (b) Scenario 2. As expected, the solar collector efficiency decreases with increasing inlet temperature; although, the efficiency of the uncoated collector decreases more rapidly than the coated collector. At lower operating temperatures (when optical efficiency is desirable) the uncoated NDAPSC is more efficient than the heat-mirror coated NDAPSC, and at higher operating temperatures (when thermal efficiency is desirable) the coated NDAPSC is more efficient—this result holds across both scenarios. In Scenario 1, the efficiency of both collectors is equivalent at $T_I^* = 120^\circ\text{C}$, while in Scenario 2 these efficiencies are equal at $T_I^* = 68.5^\circ\text{C}$. Efficiency values are lower and the difference between the uncoated and coated collectors is more pronounced in Scenario 2, which is due to the radiative intensity being lower, on average. If the collector in Scenario two was only operational when $\eta_t(t^*) > 0$ its overall efficiency would be larger.

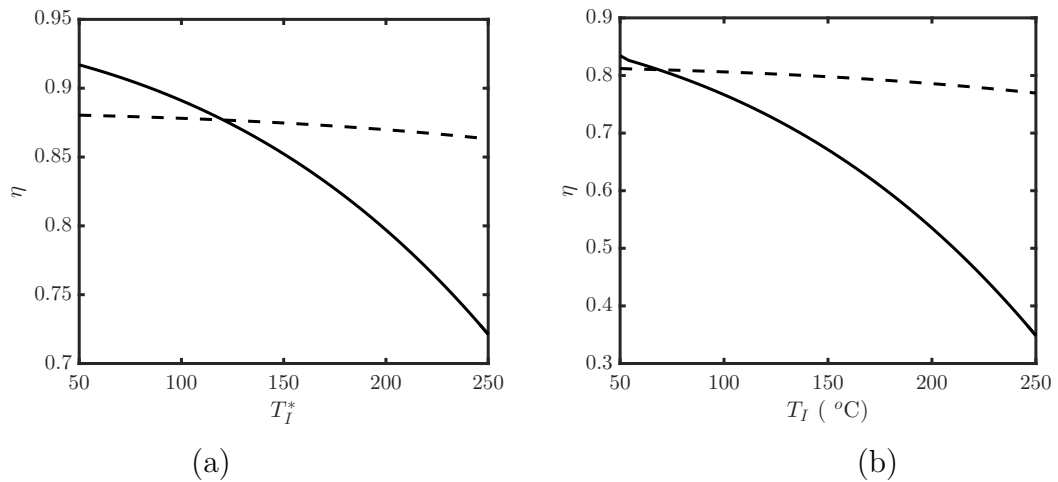


Figure 7.8: Overall efficiency versus inlet temperature for an uncoated NDAPSC (solid lines), and a heat-mirror coated NDAPSC (dashed lines). (a) Scenario 1 and (b) Scenario 2.

Figure 7.9 shows daily energy output of the solar collector versus receiver radius for an uncoated collector (solid line), and a heat-mirror coated collector (dashed line) when (a) $T_I^* = 100$ °C and (b) $T_I^* = 200$ °C. The volume flow rate is kept constant at $3.42 \times 10^{-4} \text{m}^3 \text{s}^{-1}$, and so \bar{u}^* decreases with R^2 . Also, the aperture width is fixed, so C_A decreases linearly with R . Therefore, the dimensionless quantities γ and τ^4 increase linearly with R which implies that as R increases, radiative heat losses become more significant. Physically, this is due to the receiver's surface area (the boundary where thermal emissions occur) being directly proportional to R . As expected, Figure 7.9 demonstrates that as R increases, collector efficiency decreases. The uncoated collector is more efficient than the coated collector (except when $T_I^* = 100$ °C and $R < 0.018$ m), and the uncoated collector's efficiency is much more sensitive to changes in R since its surface has a higher emissivity. To put these figures in perspective, it is estimated that a US household uses on average 10,932 kWh of electricity every year [15], this is approximately equivalent to 1.08×10^8 Joules per day. Figures 7.9 and 7.10 show that the optimum daily energy output from Scenario 2 is roughly equivalent to the daily energy consumption of eight households.

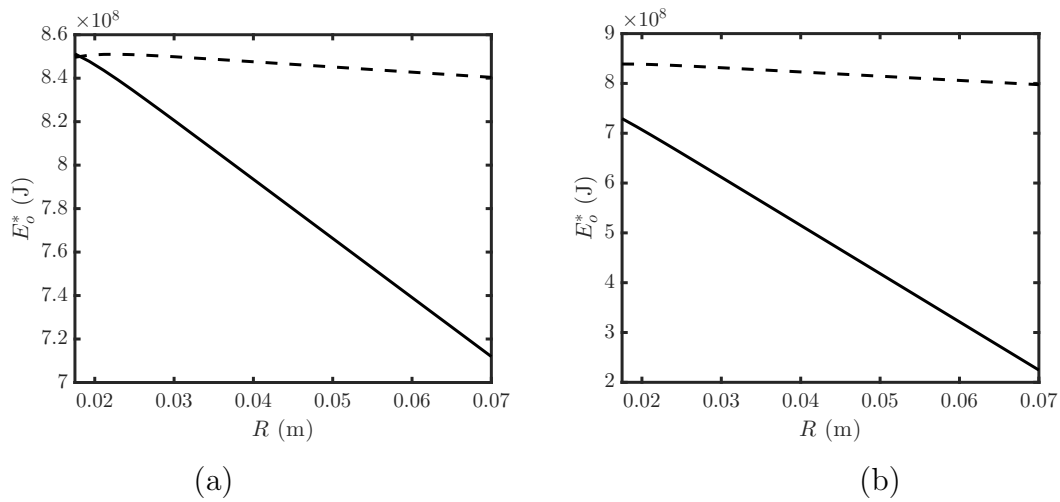


Figure 7.9: Daily energy output of the solar collector versus receiver radius for an uncoated collector (solid line), and a heat-mirror coated collector (dashed line) when (a) $T_I^* = 100^\circ\text{C}$ and (b) $T_I^* = 200^\circ\text{C}$. The volume flow rate is kept at a constant value of $3.42 \times 10^{-4} \text{m}^3 \text{s}^{-1}$, and the aperture width was also fixed.

Figure 7.10 shows the daily energy output of the solar collector versus nanofluid particle volume fraction for an uncoated collector (solid line), and a heat-mirror coated collector (dashed line) when (a) $T_I^* = 100^\circ\text{C}$ and (b) $T_I^* = 200^\circ\text{C}$. This figure shows results which are qualitatively similar to the efficiency results reported in Figure 7.7: as nanoparticles are added to the base-fluid, we observe a large increase in E_o^* ; however, these initial performance enhancements plateau as the nanoparticle concentration continues to increase. As $\Pi \rightarrow 1$, all of the available incoming radiation has already been absorbed and so additional nanoparticles do not improve collector performance. Daily energy output is larger in Figure 7.10(a) when $T_I^* = 100^\circ\text{C}$, than in Figure 7.10(b) when $T_I^* = 200^\circ\text{C}$ —since thermal losses are larger at higher operating temperatures, E_o^* decreases as T_I^* increases. However, the coated collector’s daily energy output is less sensitive to changes in T_I^* than the uncoated collector’s daily energy output since the coated collector is more thermally efficient.

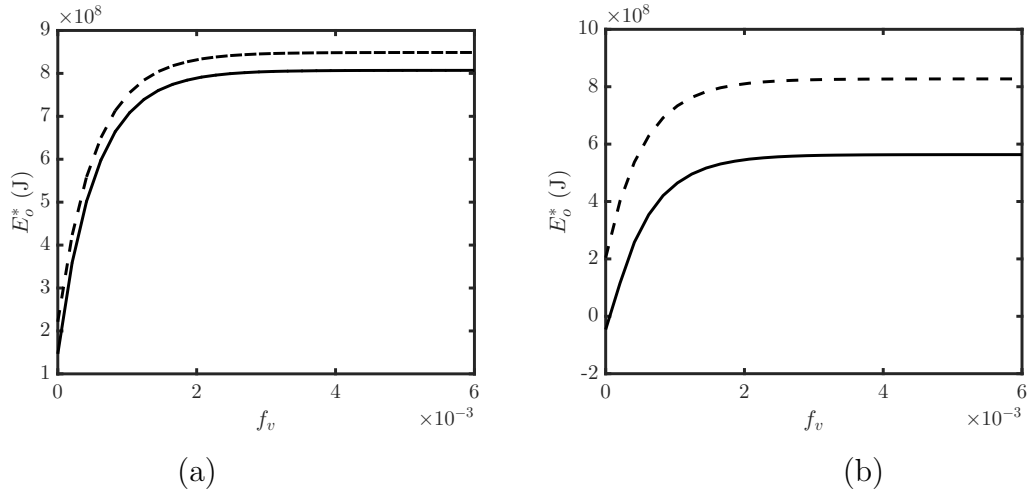


Figure 7.10: Daily energy output of the solar collector versus nanofluid particle volume fraction for uncoated collector (solid line), and heat-mirror coated collector (dashed line) when (a) $T_I^* = 100^\circ\text{C}$ and (b) $T_I^* = 200^\circ\text{C}$.

7.3 Summary and discussion

Collector 6 is similar to Collector 5, but with a time-dependent source term; as such, the two models used to describe these two collectors contain some overlap. For example, the coordinate system used in this chapter was previously used in Chapters 5 and 6, however, since we also restated it in Section 7.2.1 for completeness. In Section 7.2.2 we outlined the time-dependent conservation of energy in this system; this time-dependence is driven by the source term. We demonstrated two potential time-dependent source terms in Section 7.2.3, the first source term models cloud cover, and the second models the variation of solar intensity at different times of the day. The conservation of energy equation was nondimensionalised in Section 7.2.4, and in Section 7.2.5 a realistic case study was applied to investigate the relative sizes of the resulting dimensionless parameters. We obtained an analytical expression for the temperature in the collector in Section 7.2.6 by solving the dimensionless conservation of energy equation via the method of characteristics. This expression of temperature was then used to obtain collector efficiency and assess the collector performance under various operating conditions in Section 7.2.8.

Although the model is presented in a generalised time-dependent form, for demonstration purposes we presented two realistic time-dependent scenarios. Sce-

nario 1 demonstrated dynamic cloud cover, and Scenario 2 demonstrated the variation of solar intensity at different times of the day. We used Scenario 1 to highlight how an instantaneous measure of efficiency may be misleading and lead to non-physical results ($\eta > 1$), and we used Scenario 2 to illustrate how weather forecasting can be used to decide when to begin and end an NDAPSCs daily operation cycle. We also varied several of the system's physical parameters to assess their effect on collector performance. The NDAPSC model showed that the overall energy output decreased as R increased, and furthermore, the parameter space exploration showed qualitative agreement with existing NDAPSC models [28, 38, 42]: efficiency increased with increasing nanoparticle volume fraction, and decreased with decreasing flow rates or increasing inlet temperature; heat-mirrors sometimes (but not always) enhance collector efficiency.

Scenario 1 highlighted the superiority of a time-dependent model over a steady state model. The system's temperature entered a period of rapid transition immediately after a cloud passed over the receiver—none of the existing steady-state models can accurately predict an NDAPSC's temperature profile while the solar intensity is rapidly changing, thus emphasising the value of the model proposed in this chapter.

CHAPTER 8

FURTHER DISCUSSION

This chapter restates and discusses the research in this study. In Section 8.1 we remind the reader of the main findings from each model, and in Section 8.2 we discuss these results through the lens of the three primary research objectives which were stated back in Section 1.3.

8.1 Summary of work

Collector 1

In Chapter 2 we developed a two-dimensional model for the efficiency of Collector 1 (which was an inclined, parallel-plate nanofluid-based direct absorption solar collector). This type of collector had been modelled previously [10, 36, 62, 63], and all of the components of the model used in this chapter had been proposed in previous research, however, we were the first to combine them. Cregan and Myers [10] modelled the collector via the less accurate plug flow approximation and obtained an analytic expression for the radiative flux integral, while Lee and Jang [36] modelled the collector using a depth-dependent flow, but, they numerically evaluated the term describing the source of heat. We defined the system geometry in Section 2.2.1 and expressed the conservation of energy in Section 2.2.2. The conservation of energy required us to obtain the thermophysical properties of the nanofluid (which we described in Section 2.2.3), a fluid velocity term (which was obtained via a conservation of momentum argument in Section 2.2.4), and a heat

source term (which we obtained via an approximation method in Section 2.2.5). We non-dimensionalised the conservation of energy PDE in Section 2.2.6, and the system was defined in terms of five dimensionless parameters.

We obtained a solution for the temperature in the system via a separation of variables method applied to the conservation of energy PDE (recall that alternative expressions for this temperature profile were also provided in Appendix A). In Section 2.2.9, we defined solar collector efficiency, in doing so we also redefined the standard efficiency definition such that it now extends to a collector with an isothermal base panel. We plotted and discussed various parameter configurations and how they affect collector efficiency in Section 2.2.10. Figure 2.8 showed how the collector's temperature in the cross section varied at different positions along the receiver. Figure 2.9 highlighted the difference between Cregan and Myers' [10] plug flow model, and the depth-dependent model; the plug flow method overestimated collector efficiency by roughly 1% across all of the channel depths explored. Figure 2.10 showed how the efficiency of the collector increases with increasing nanofluid particle volume fraction before plateauing at 81.2%. While this collector was quite efficient, it did not produce a substantial temperature increase between the inlet and the outlet, and so its utility in real-world applications would be rather limited. In the succeeding chapters, we explored and discussed alternative collector designs more suitable to real-world applications.

Collector 2

In Chapter 3 we modelled the efficiency of Collector 2, a parallel-plate NDASC on an inclined plane with a reflective base panel. This type of collector had previously been studied experimentally and modelled numerically, however, this particular system configuration had not been studied analytically. The modelling approach taken in this chapter closely followed the modelling methodology outlined in Chapter 2. The two models had many similarities: the system geometries were defined using the same coordinate system, conservation of momentum took the same form, the thermophysical properties of the nanofluid were calculated using the same method, and there were various other system parallels. However, there were also some fundamental differences between Collectors 1 and 2. One major difference was the heat source term: in Section 3.2.4 we showed how the reflective base panel alters the form of the radiative flux integral and thus the PDE describing the conservation of energy. Other significant differences between

the two collectors were highlighted in Table 3.2, where we detailed the parameter values used in this chapter's case study. Following dimensionless analysis, we observed that $\gamma \sim O(10)$ and so diffusion had much more importance in Collector 2 than in Collector 1. The dimensionless conservation of energy PDE describing this collector was solved via separation of variables; the homogeneous component of this solution was equivalent to the homogeneous solution from Chapter 2. However, the inhomogeneous part of the solution was new, and we outlined its solution method in Section 3.2.7.

We plotted and discussed various parameter values and how they affect collector efficiency in Section 3.2.8. Figure 3.4 showed that the reflective base panel did indeed improve collector efficiency, as did nanoparticle volume fraction. The efficiency in this figure reached 54% and did not plateau like the efficiency in Figure 2.10 from Chapter 2 because the channel was much more shallow. We compared the efficiencies of Collectors 1 and 2 in Figure 3.8, showing that Collector 2 can reach efficiency values of up to 81.3% when its channel height was comparable to the channel height which produced Collector 1's optimal performance. At lower channel heights the distinction between the efficiencies of Collectors 1 and 2 became more pronounced, Collector 2 was universally more efficient. In Figure 3.5 we highlighted the difference that a reflective base panel makes to the temperature at the outlet, we also noted that even though this collector had lower efficiencies than Collector 1, it had a higher temperature at the outlet due to its decreased cross-sectional area—although Collector 2 did not absorb as much of the incoming radiation, there was a lower volume of nanofluid to heat and so the overall temperature rise across the system was greater. While NDASCs are designed to absorb sunlight, sometimes they are tested using heat lamps that generate incoming black-body radiation. Heat lamps can produce a constant and predictable source of radiation making them ideal for testing solar collectors in controlled environments. Therefore, it was important for us to better understand how the optical properties of nanofluids changed with different sources of radiation. In this chapter we considered two alternative sources of black-body radiation: the first was a heat lamp at 3158 K, and the second was the Sun at 5800 K. Figure 3.7 showed how the temperature of the heat source significantly affects collector efficiency, this was important to note as it suggested that NDASCs perform differently when they are in certain testing environments than they do in exposure to real sunlight.

The reflective base panel certainly improved collector performance over the non-reflective base panel, and the temperature at the outlet improved with decreasing channel height; however, at higher operating temperatures this solar collector became less efficient, and the temperature rise across the system was still too low for most real-world applications. These results triggered us to explore alternative solar collector designs with an aim to increase the viability of NDASCs in real-world settings.

Collector 3

In Chapter 4 we modelled the efficiency of Collector 3, a novel NDASC design. In this collector, nanofluid flowed through a series of optically transparent pipes rather than between parallel plates like in Collectors 1 and 2; therefore, we defined the solar collector in a three-dimensional cylindrical coordinate system in Section 4.2.1. We modelled the conservation of energy in the system in Section 4.2.2; this model included a term describing the nanofluid flow (discussed in Section 4.2.3) and an expression describing the absorption of incoming solar radiation (discussed in Section 4.2.4). We nondimensionalised the model and applied realistic parameter values in order to investigate the relative importance of the dimensionless parameters in Section 4.2.6. Unlike previous chapters, in this chapter the temperature of the nanofluid in the collector was obtained numerically rather than analytically. This temperature was used to calculate the efficiency of the collector. We presented and discussed our results in Section 4.2.8. This NDASC design has two fundamental flaws. Firstly, cooling takes place over a large surface area in this design; the ratio between the aperture area and receiver area was $\pi/2$, i.e., the surface where heat loss takes place was $\pi/2$ times larger in Collector 3 than in Collectors 1 and 2. This ratio can be reduced by concentrating the incoming solar radiation or by simply adopting a parallel plate NDASC design used in Collectors 1 and 2. Secondly, much of the incoming radiation was not normal to the receiver surface. In a volumetric receiver, one must also consider the angle that the incoming radiation makes to the normal of the receiver. Figure 4.9 showed how the fraction of incoming radiation that gets absorbed into the system varies with this angle; as the angle increases, less of the incoming radiation was absorbed by the nanofluid. This result was used to inform our design of Collector 4.

Collector 4

In Chapter 5 we modelled the efficiency of Collector 4, which was another novel NDASC design—a low-profile nanofluid-based direct absorption parabolic trough solar collector. This collector design concentrates incoming solar radiation and can result in higher system temperatures; so, in Section 5.2.1 we discussed heat-mirrors since they offer a potential solution negating the increased thermal losses. While discussing heat-mirrors we discovered mathematical expressions for the optical properties of an ideal heat-mirror. We identified three possible configurations for Collector 4’s design in Section 5.2: Collector 4 (a) has no vacuum annulus, Collector 4 (b) has a vacuum annulus, and Collector 4 (c) has a vacuum annulus and a heat-mirror. In Section 5.3.1 we described the coordinate geometry system in which the collector was defined. The conservation of energy for this collector was discussed in Section 5.3.2, and a conservation of momentum argument was applied to obtain a depth-dependent velocity profile in the system in Section 5.3.3. An expression for the source term was identified via a combined coordinate geometry and calculus method in Section 5.3.4. In Section 5.3.6 we nondimensionalised the conservation of energy model. The model was governed by seven dimensionless parameters: two describe the rates of thermal diffusion to advection, two describe Newton cooling, and three describe radiative heat loss. We applied realistic parameter values from a case study to investigate the relative magnitudes of the dimensionless parameters in Section 5.3.5. This analysis revealed that one of the diffusive terms could be neglected and that the radiative heat-loss term could be linearised, resulting in a simplified system. The system of governing equations required a numerical method to obtain an expression for the outlet temperature. In Appendix C we introduced a modification to the standard Crank-Nicolson finite difference method which led to more accurate results, due to non-linearities in the source term.

We varied several of the system’s physical parameters to assess their affect on collector performance. The NDAPSC model shows qualitative performance agreement with existing NDAPSC models [28, 38, 42]: efficiency increased with increasing nanoparticle volume fraction, efficiency decreased with decreasing flow rates, and efficiency decreased with increasing inlet temperature. More specifically, Collector 4 (a) was the most efficient design at higher particle volume fractions while Collector 4 (c) was the most efficient design in the case of a pure

base-fluid. Even though Collector 4 (a) had the highest radiative and convective thermal losses, it was still more efficient than the other designs when $f_v > 0.001$ because it was more optically efficient. Also, Collector 4 (a) was the most efficient design when $\bar{u}^* > 0.0025 \text{ ms}^{-1}$; however, at lower velocities (i.e., hotter operating conditions) Collector 4 (c) was the most efficient design.

This chapter also explored the performance implications of design choices such as focal length, aperture width, and receiver radius. The focal length and aperture width determine ϕ_{crit} , and we found that collector efficiency declines approximately linearly as ϕ_{crit} decreases. We also found that at smaller aperture widths Collector 4 (c) was the most efficient design, however, when $W > 0.07 \text{ m}$ Collector 4 (a) demonstrated superior levels of efficiency. Meanwhile, when either $R < 0.0038 \text{ m}$ or $R > 0.01 \text{ m}$, Collector 4 (c) outperformed the other two collectors.

The parameter space exploration conducted in this chapter suggested that the optimal collector design largely depends on the operating conditions. Since Collector 4 (a) was the most optically efficient design, and Collector 4 (c) was the most thermally efficient design; in general, when greater thermal efficiency was desirable (i.e., when radiative heat losses are large), Collector 4 (c) outperformed the other designs. Meanwhile, at lower operating temperatures, greater optical efficiency was desirable and so Collector 4 (a) outperformed the other designs.

Collector 5

Chapter 6 also modelled a parabolic trough solar collectors, however, this time we considered Collector 5, a larger, industrial-scale collector. In this chapter we developed an approximate analytic solution to a three-dimensional model for the efficiency of a large NDAPSC. The model consisted of a system of partial differential equations describing the conservation of mass, momentum, and energy. We obtained a heat source term via the radial flux integral. We expressed the system in nondimensional form to show that there were four controlling nondimensional numbers, specifically two describing the heat source, one describing the relative importance of conduction and advection and three representing the heat loss to the surroundings. We used a specific case study described in Khullar et al. [29], to evaluate the relative importance of these nondimensional subgroups under realistic physical conditions. This study showed that two of the nondimensional numbers have a much lower impact on the performance of the solar collector and

we ignored their effects to obtain a leading order approximation of the system. One of these small dimensionless parameters, $1/Pe$, represents the ratio between thermal diffusion and advection in the downstream direction. Neglecting the second small dimensionless parameter, φ , allowed us to approximate the radiative heat loss in the solar collector with a black-body radiation calculation of a body at the inlet temperature—at leading order, an NDAPSC loses heat at a constant rate of $\sigma\epsilon T_I^4$. By examining the non-dimensional system we were able to eliminate negligible terms and so determine that the temperature increases almost linearly along the pipe. This has previously been observed both numerically and via experiments [42].

Previous research has suggested that coating improves efficiency [28, 38, 59]. Our results showed that this was not always the case: for lower temperatures an uncoated system was more efficient. We provided an equality to determine when coating was appropriate. We used this inequality to show that as the solar concentration ratio increases, an uncoated NDAPSC becomes more efficient than an NDAPSC coated with a heat-mirror; at higher inlet temperatures, the concentration ratio required for an uncoated NDAPSC to be more efficient than a coated NDAPSC increases. Whilst there were existing frameworks for assessing a heat-mirror’s performance, this inequality did not appear anywhere else in the literature and should be considered extremely informative for NDAPSC design.

Collector 6

In Chapter 7 we proposed a time-dependent, three-dimensional model for the efficiency of Collector 6 (which was an NDAPSC under a turbulent flow regime). The model consisted of a system of equations: a partial differential equation describing the conservation of energy, and a time-dependent radiative transport equation describing the propagation of solar radiation through the nanofluid. Writing the model in dimensionless form revealed four controlling dimensionless numbers: one describing the relative importance of conduction and advection and three describing the heat loss to the surroundings. Realistic parameter values were applied to reduce the model further and this indicated that two of the dimensionless groups had a much lesser impact on the performance of the solar collector. In Section 7.2.6 we obtained an analytic expression for the temperature in the collector by solving the dimensionless conservation of energy equation via the method of characteristics. This expression for the temperature was then used

to obtain collector efficiency and assess the collector performance under various operating conditions in Section 7.2.8.

Although the model is presented in a generalised time-dependent form, for demonstration purposes presented two realistic time-dependent scenarios. Scenario 1 demonstrates dynamic cloud cover, and Scenario 2 demonstrates the variation of solar intensity at different times of the day. We used Scenario 1 to highlight how an instantaneous measure of efficiency may be misleading and lead to non-physical results ($\eta > 1$), and we used Scenario 2 to illustrate how weather forecasting can be used to decide when to begin and end an NDAPSCs daily operation cycle. We also varied several of the system's physical parameters to assess their affect on collector performance. The NDAPSC model showed that the overall energy output decreased as R increased, and furthermore, the parameter space exploration showed qualitative performance agreement with existing NDAPSC models [28, 38, 42]: efficiency increased with increasing nanoparticle volume fraction, efficiency decreased with decreasing flow rates, efficiency decreased with increasing inlet temperature, and heat-mirrors sometimes (but not always) enhanced collector efficiency.

Scenario 1 highlighted the superiority of a time-dependent model over a steady state model. The system's temperature entered a period of rapid transition immediately after a cloud passed over the receiver—none of the existing steady-state models could accurately predict an NDAPSC's temperature profile while the solar intensity is rapidly changing, thus emphasising the value of the model proposed in this chapter.

8.2 Objective review

Recall from Chapter 1 where we defined the following research objectives:

1. Complete a literature review of nanofluids and NDASCs,
2. Identify opportunities for future research in this field,
3. Formulate useful mathematical models for NDASCs.

In this section we critically evaluate our thesis through the lens of these three objectives.

Nanofluid-based direct absorption solar collectors are a relatively new technology, and the scientific literature surrounding them is evolving at a rapid pace. As a result, Objective 1 has been an ongoing pursuit throughout the entire project; over 20% of the literature cited in this thesis was published since we began our initial research.

When we started modelling Collector 1, there were no existing analytic models for a parallel-plate NDASC that included a depth-dependent velocity profile. We modelled Collector 1 with a view towards filling this significant gap in the literature. However, while we were working on this model, Lee and Jang [36] published a paper that included a similar modelling approach to ours, thus reducing the novelty of our model for Collector 1. Initially, this was a discouraging revelation; however, we took some encouragement from knowing our intuition about the direction of future research was correct.

We began Chapter 3, by outlining the existing literature surrounding a parallel plate NDASC with a reflective base panel. This literature review highlighted the potential for an analytic model to bolster existing experimental and numerical modelling efforts; we felt that such a model would fill a relevant gap in the literature and be a valuable asset for future researchers. The analytic model proposed for Collector 2 showed: how Collector 2 was a superior NDASC design to Collector 1, how the temperature of the source of incoming radiation affected collector performance, and how the reflected radiation could be approximated using the method outlined in Cregan and Myers [10]. Moreover, this analytic model allowed for an extensive exploration of the parameter space—a process which would have been cost prohibitive to achieve experimentally. These are useful results, and we aim to publish them in some form over the coming months.

Collector 3 was a new NDASC design; while this collector did not appear in previous literature, it was connected to past research in that it was an unfruitful attempt to improve on some of the shortcomings of Collectors 1 and 2. In retrospect, this collector’s design flaws seem obvious. If one increases the surface area across which heat loss takes place, one would expect greater levels of heat loss; furthermore, if one decreases the incoming radiation’s path-length, one would expect less of the incoming radiation to get attenuated. However, these phenomena did not become apparent to us until we modelled this collector; thus, the modelling exercise was a valuable learning experience. The model for Collector 3 was useful in the sense that it informed our design for Collector 4—a much-improved solar collector over Collector 3.

While Collector 4 was another new NDASC design, previous nanofluid-based direct absorption parabolic trough solar collectors had been studied in the literature, and so the model used to describe this was mostly informed by existing research. Although, we had to make assumptions or adjust our aims where there was no existing research. The model proposed for Collector 4 was recently submitted for publication and is currently under review. We also achieved two secondary research outcomes while modelling Collector 4. Heat-mirrors were clearly under-served by the literature, and so, although it was not the primary focus of this thesis, we introduced a mathematical method for describing the optical properties an ideal heat-mirror; this result will undoubtedly be useful to future scientists in that ‘up-and-coming’ area of research. We discuss this further in Appendix B. Also, Collector 4’s source term was highly non-linear, and this led to computational inaccuracies. We proposed a novel alternative to the standard Crank-Nicolson method which anticipates (and corrects) errors arising from a discretisation of the non-linear source term. This result is discussed further in Appendix C.

We decided to model Collector 5 while we were reading about NDAPSCs for Collector 4’s model. Larger NDAPSCs appear more often in the recent literature than low-profile NDAPSCs—industrial-scale NDAPSCs are a more active area of research. However, the research in this field was mostly experimental (with some numerical treatments). The model we proposed for Collector 5 was the first entirely analytic treatment an industrial-scale NDAPSC. Since this is such an active area of research, we felt that the model for Collector 5 would be beneficial

for both, existing, and future scientists, and accordingly, it was featured in an article that was published in *Solar Energy*.

The model describing Collector 6, built upon the model describing Collector 5 by introducing a time-dependent source of heat. We noted from Kolb [31] how a solar collector must, by its nature, operate cyclically. NDASCs experience fluctuating operating temperatures; however, this effect had not been studied in the literature. The model used to describe and assess Collector 6 was recently submitted for publication and is currently under review. We anticipate that this time-dependent model will be an important contribution to the literature.

Although the research in this thesis has addressed several significant gaps in the literature, future complimentary work could be extremely valuable to the field of NDASC design. We note that even though one-dimensional parameter studies are conducted on each model in this thesis, the results of these studies are somewhat limited since they only focus on optimising receiver efficiency and outlet temperature. We anticipate that the mathematical models proposed in this thesis could be used within formal multi-objective optimisation processes which seek to identify optimal collector designs. (Multi-objective design optimisation has previously been implemented in the design of solar-powered irrigation systems, see Ganesan et al., [17].) Before looking for optimal collector designs, one would need to identify the characteristics which contribute the most to the overall value of the design. For example, a good design may involve multiple criteria/objectives such as manufacturing cost, operating cost, expected life-cycle, receiver efficiency, outlet temperature, etc. Also, we note that some of these objectives are conflicting: as an NDASC's operating temperature increases, its receiver efficiency typically decreases. Furthermore, if an NDASC was to be used in conjunction with a Carnot heat engine to generate electricity, its Carnot efficiency would increase and its receiver efficiency would decrease, as its operating temperatures increases (see Figure 9 from veeraragavan et al. [66] for an illustration of the relationship between receiver efficiency and Carnot efficiency). Therefore, optimisation search algorithms such as conjugate gradients or combinations of design of experiments and meta-modelling approaches may be needed to find optimal NDASC designs. This thesis solely focuses, on calculating receiver efficiency and outlet temperature, therefore, in order to find optimal collector designs, further work would be needed to define and calculate: manufacturing cost, operating cost, expected life-cycle, etc.

8. FURTHER DISCUSSION

So far, research in this thesis has been the subject of: one published journal article, one published conference paper, two journal articles (currently under review), one chapter of a book (to be submitted for publication in late 2018), six conference presentations, and three informal talks. Looking forwards, we identify the following as opportunities for further research output:

- Improved solar collector designs,
- Experimental validation/invalidation of existing models,
- Time-dependent modelling of NDASCs under laminar flow,
- Further improvements to numerical solution methods,
- Better heat-mirrors.

Appendices

APPENDIX A

ALTERNATIVE EXPRESSION OF HYPER-GEOMETRIC FUNCTION

While the $D_\nu(x)$ notation can be used to express the analytic solution for (2.2.41), using this notation in Matlab is made difficult due to the lack of inbuilt functions. Abramowitz and Stegun [1] introduce an alternative notation whereby solutions to $g''(x) - (\frac{1}{4}z^2 + a)g(x) = 0$, can be expressed in the form $g(x) = K_1U(a, x) + K_2V(a, x)$ where

$$U(a, x) = D_{-a-\frac{1}{2}}(x),$$

$$V(a, x) = \frac{1}{\pi}\Gamma\left(\frac{1}{2} + a\right) \left\{ \sin \pi a \cdot D_{-a-\frac{1}{2}}(x) + D_{-a-\frac{1}{2}}(-x) \right\}.$$

Using this notation,

$$T(x, z) = w(z) + \sum_{n=1}^{\infty} \left[C_n \exp(-\lambda p_n^2 x) \left[U\left(\frac{-p_n}{8}, \sqrt{2p_n} \left[z - \frac{1}{2}\right]\right) + K_3 V\left(\frac{-p_n}{8}, \sqrt{2p_n} \left[z - \frac{1}{2}\right]\right) \right] \right].$$

The weight function in this Sturm-Liouville problem which is defined by $g''(x) - (\frac{1}{4}z^2 + a)g(x) = 0$, is $(\frac{1}{4}z^2 + a)$ and so orthogonality requires

$$\int_0^1 \left(\frac{1}{4}z^2 + a\right) g_n g_m dz = 0 \tag{A.0.1}$$

for $n \neq m$. The series coefficient C_n is determined, after imposing the initial condition and the constants, K_3 is obtained by applying the boundary conditions:

$$K_3 = \frac{U' \left(\frac{-p_n}{8}, \sqrt{2p_n} \left[z - \frac{1}{2} \right] \right)}{V' \left(\frac{-p_n}{8}, \sqrt{2p_n} \left[z - \frac{1}{2} \right] \right)} \Big|_{z=0}, \quad (\text{A.0.2})$$

$$C_n = - \frac{\int_0^1 w(z) \left(\frac{1}{4}z^2 - \frac{p_n}{8} \right) \left[U \left(\frac{-p_n}{8}, \sqrt{2p_n} \left[z - \frac{1}{2} \right] \right) + K_3 V \left(\frac{-p_n}{8}, \sqrt{2p_n} \left[z - \frac{1}{2} \right] \right) \right] dz}{\int_0^1 \left(\frac{1}{4}z^2 + a \right) \left[U \left(\frac{-p_n}{8}, \sqrt{2p_n} \left[z - \frac{1}{2} \right] \right) + K_3 V \left(\frac{-p_n}{8}, \sqrt{2p_n} \left[z - \frac{1}{2} \right] \right) \right]^2 dz}, \quad (\text{A.0.3})$$

where the eigenvalues, p_n satisfy

$$\begin{aligned} & \left[U' \left(\frac{-p_n}{8}, \sqrt{2p_n} \left[z - \frac{1}{2} \right] \right) + K_3 V' \left(\frac{-p_n}{8}, \sqrt{2p_n} \left[z - \frac{1}{2} \right] \right) \right] \Big|_{z=0} \\ & = Nu \left[U \left(\frac{-p_n}{8}, -\sqrt{\frac{p_n}{2}} \right) + K_3 V \left(\frac{-p_n}{8}, -\sqrt{\frac{p_n}{2}} \right) \right]. \end{aligned} \quad (\text{A.0.4})$$

Luckily, we can obtain Matlab functions for $U(a, x)$, $V(a, x)$, $U'(a, x)$, and $V'(a, x)$ thanks to Cojocaru [7], so we use this formulation of the analytic solution in Section 2.2.10.

Alternatively one might solve (2.2.41) via a series solution—the method applied by Lee and Jang [36]. We assume that $g(z)$ can be expressed with the power series

$$g(z) = \sum_{n=0}^{\infty} A_n z^n. \quad (\text{A.0.5})$$

Therefore, (2.2.41) can be written as

$$\sum_{n=0}^{\infty} (n+2)(n+1)A_{n+2}z^n + p_n^2 \sum_{n=1}^{\infty} A_{n-1}z^n - p_n^2 \sum_{n=2}^{\infty} A_{n-2}z^n, \quad (\text{A.0.6})$$

and so $g(z)$ can be represented with a linear combination of $g_0(z)$ and $g_1(z)$ where

$$g_0(z) = 1 - \frac{p_n^2}{3!}z^3 + \frac{2p_n^2}{4!}z^4 + \frac{4p_n^4}{6!}z^6 - \frac{30p_n^4}{7!}z^7 + \frac{60p_n^4}{8!}z^8 - \frac{28p_n^6}{9!}z^9 + \dots, \quad (\text{A.0.7})$$

$$g_1(z) = z - \frac{2p_n^2}{4!}z^4 + \frac{6p_n^2}{5!}z^5 + \frac{10p_n^4}{7!}z^7 - \frac{96p_n^4}{8!}z^8 + \frac{252p_n^4}{9!}z^9 + \dots. \quad (\text{A.0.8})$$

Overall, the temperature of the nanofluid is given by

$$\bar{T}(x, z) = \sum_{n=0}^{\infty} \left[C_n e^{-p_n^2 \gamma x} (g_0(z) + K_3 g_1(z)) \right] + w(z). \quad (\text{A.0.9})$$

The constant $K_3 = -g'_0(1)/g'_1(1)$ is obtained via the boundary condition at $z = 1$. The eigenvalues (p_n^2) satisfy the boundary condition at $z = 0$ i.e.,

$$K_3 = \text{Nu} \left(g_0(0) + K_3 g'_1(0) \right). \quad (\text{A.0.10})$$

The series coefficients are then determined, after imposing the initial condition and so

$$C_n = - \frac{\int_0^1 w(z)(z - z^2) (g_0(z) + K_3 g_1(z)) dz}{\int_0^1 (z - z^2) (g_0(z) + K_3 g_1(z))^2 dz}. \quad (\text{A.0.11})$$

APPENDIX B

IDEAL HEAT-MIRRORS

Assuming that the spectral intensity of incoming solar radiation at a heat-mirror's surface, J_s^* , is known and is normal to the receiver, this spectral irradiance is approximated via Planck's black-body relation and can be expressed as

$$J_s^* = \frac{2hc^2\Omega_S S_{Att} C_A}{\lambda^5 \left(\exp\left(\frac{hc}{\lambda k_B T_s^*}\right) - 1 \right)}. \quad (\text{B.0.1})$$

The spectral irradiance of outgoing black-body radiation, J_{Bb}^* , and incoming ambient black-body radiation, J_A^* , are also approximated in the same manner, i.e.,

$$J_{Bb}^* = \frac{2\pi hc^2}{\lambda^5 \left(\exp\left(\frac{hc}{\lambda k_B T_{Bb}^*}\right) - 1 \right)}, \quad J_A^* = \frac{2\pi hc^2}{\lambda^5 \left(\exp\left(\frac{hc}{\lambda k_B T_A^*}\right) - 1 \right)}, \quad (\text{B.0.2})$$

where T_{Bb}^* is the temperature of the black-body, and T_A^* is the ambient temperature.

A heat-mirror must maximise its transparency for incoming radiation while maximising its reflectivity for outgoing black-body emissions. Therefore, an ideal heat-mirror has 100% transmissivity ($\tau = 1$), across wavelengths where the incoming radiation has a greater spectral intensity than the outgoing black-body radiation, i.e., $J_s^*(\lambda) + J_A^*(\lambda) > J_{Bb}^*(\lambda)$; it also has 100% reflectivity ($\epsilon = 0$), across the wavelengths where black-body radiative emissions exceed incoming radiation, i.e., $J_s^*(\lambda) + J_A^*(\lambda) < J_{Bb}^*(\lambda)$. (Figure B.1(b) demonstrates how an ideal heat-mirror selectively transmits and reflects incoming radiation depending on its

B. IDEAL HEAT-MIRRORS

wavelength.) More specifically, the spectral dependent optical properties of an ideal heat-mirror are

$$\tau(\lambda) = \begin{cases} 0 & \text{if } \lambda > \lambda_{\text{crit}} \\ 1 & \text{if } \lambda \leq \lambda_{\text{crit}}, \end{cases} \quad (\text{B.0.3})$$

and

$$\epsilon(\lambda) = \begin{cases} 1 & \text{if } \lambda > \lambda_{\text{crit}} \\ 0 & \text{if } \lambda \leq \lambda_{\text{crit}}, \end{cases} \quad (\text{B.0.4})$$

where λ_{crit} satisfies

$$\begin{aligned} & \frac{2hc^2\Omega_S S_{Att} C_A}{\lambda_{\text{crit}}^5 \left(\exp\left(\frac{hc}{\lambda_{\text{crit}} k_B T_{Sun}^*}\right) - 1 \right)} + \frac{2\pi hc^2}{\lambda_{\text{crit}}^5 \left(\exp\left(\frac{hc}{\lambda_{\text{crit}} k_B T_A^*}\right) - 1 \right)} \\ &= \frac{2\pi hc^2}{\lambda_{\text{crit}}^5 \left(\exp\left(\frac{hc}{\lambda_{\text{crit}} k_B T_{Bb}^*}\right) - 1 \right)}. \end{aligned} \quad (\text{B.0.5})$$

We illustrate an example of the two potential spectral intensities, $J_s^*(\lambda) + J_A^*(\lambda)$, and $J_{Bb}^*(\lambda)$, in Figure B.1(a). In Region I, $\lambda \leq \lambda_{\text{crit}}$, and the transmissivity is maximised, while in Region II the reflectivity is maximised.

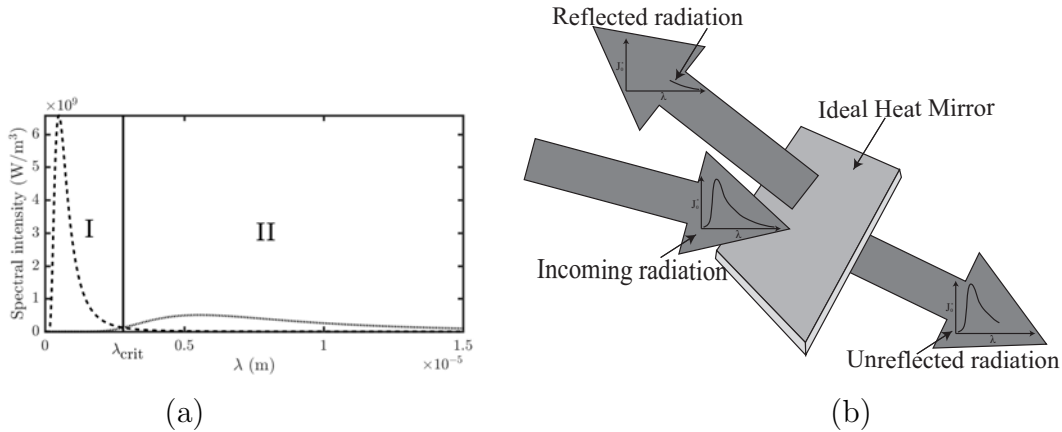


Figure B.1: (a) Spectral intensity of $J_s^*(\lambda) + J_A^*(\lambda)$ (dashed line) and $J_{Bb}^*(\lambda)$ (dotted line) versus wavelength where $T_S = 5505^\circ\text{C}$, $T_{Bb}^* = 250^\circ\text{C}$, and $T_A^* = 30^\circ\text{C}$ the total solar intensity at the surface of the receiver is 5000 W/m^2 , and $\lambda_{\text{crit}} = 2.81 \times 10^{-6} \text{ m}$, and (b) Illustration of the selective reflectivity and transmittance of an ideal heat-mirror.

The EFS framework enables us to easily compare two different heat-mirrors against each other; however, since the optical properties of an ideal heat-mirror are not explicitly defined in the literature, the maximum possible EFS score is unknown—this value would be a useful tool for evaluating heat-mirrors further and understanding the scope for future performance improvements. Even an ideal heat-mirror can not reflect all of the outgoing black-body radiation while simultaneously letting all of the incoming solar radiation through. We note from Figure B.1(a) that the spectral radiance of G_s^* in Region I is non-zero and so some of the incoming solar radiation will be reflected. Similarly, the spectral radiance of G_{Bb}^* is non-zero in Region I and so some of the emitted black-body radiation exits the receiver. In the case of an ideal heat-mirror, the effective solar transparency and the effective infra-red emissivity of a heat-mirror, as defined by Fan and Bachner [16], are simplified to

$$\tau_{\text{eff}} = \frac{\int_0^{\lambda_{\text{crit}}} G_s^*(\lambda) d\lambda}{\int_0^{\infty} G_s^*(\lambda) d\lambda}, \quad \epsilon_{\text{eff}} = \frac{\int_0^{\lambda_{\text{crit}}} G_{Bb}^*(\lambda) d\lambda}{\int_0^{\infty} G_{Bb}^*(\lambda) d\lambda}, \quad (\text{B.0.6})$$

with analytic solutions

$$\tau_{\text{eff}} = \frac{15}{\pi^4} \sum_{n=1}^{\infty} \exp(-nx_s) \left(\frac{x_s^3}{n} + 3\frac{x_s^2}{n^2} + 6\frac{x_s}{n^3} + \frac{6}{n^4} \right), \quad (\text{B.0.7})$$

for $x_s = hc/(\lambda_{\text{crit}} k_B T_s)$ and

$$\epsilon_{\text{eff}} = \frac{15}{\pi^4} \sum_{n=1}^{\infty} \exp(-nx_{Bb}) \left(\frac{x_{Bb}^3}{n} + 3\frac{x_{Bb}^2}{n^2} + 6\frac{x_{Bb}}{n^3} + \frac{6}{n^4} \right), \quad (\text{B.0.8})$$

for $x_{Bb} = hc/(\lambda_{\text{crit}} k_B T_{Bb}^*)$. An ideal heat-mirror for the example shown in Figure B.1(a) has an effective solar transparency of $\tau_{\text{eff}} = 0.9711$ and effective infra-red emissivity $\epsilon_{\text{eff}} = 0.0077$.

Both the incoming solar radiation intensity and the temperature of the black-body affect λ_{crit} , and this relationship is not necessarily intuitive from first glance of (B.0.5) (which must be solved numerically). Figure B.2 shows the spectral radiance versus wavelength for incoming solar energy at 500 W/m² (dot-dashed grey lines), 1000 W/m² (dashed grey lines), 2000 W/m² (solid grey lines), and outgoing black-body radiation (solid black lines), (a) $T_{Bb}^* = 250$ °C, and (b) $T_{Bb}^* = 50$ °C. As the intensity of the incoming solar radiation increases, λ_{crit} also

B. IDEAL HEAT-MIRRORS

increases; in Figure B.2a when $G_s^* = 500 \text{ W/m}^2$, $\lambda_{\text{crit}} = 2.2 \times 10^{-6} \text{ m}$; meanwhile, when $G_s^* = 2000 \text{ W/m}^2$, $\lambda_{\text{crit}} = 2.53 \times 10^{-6} \text{ m}$, an 15% increase. Similarly in Figure B.2b when G_s^* is increased from 500 W/m^2 to 2000 W/m^2 , λ_{crit} increases from $4.08 \times 10^{-6} \text{ m}$ to 4.85×10^{-6} , an 15.7% increase. Meanwhile, the temperature of the black-body has the opposite affect on λ_{crit} , as T_{Bb}^* decreases, λ_{crit} increases. For example, in Figure B.2 (a) when $G_s^* = 500 \text{ W/m}^2$ and $T_{Bb}^* = 250 \text{ }^\circ\text{C}$, $\lambda_{\text{crit}} = 2.2 \times 10^{-6} \text{ m}$; meanwhile, in Figure B.2 (b), when $G_s^* = 500 \text{ W/m}^2$ and $T_{Bb}^* = 50 \text{ }^\circ\text{C}$, $\lambda_{\text{crit}} = 4.08 \times 10^{-6} \text{ m}$, an increase of 85.5%.

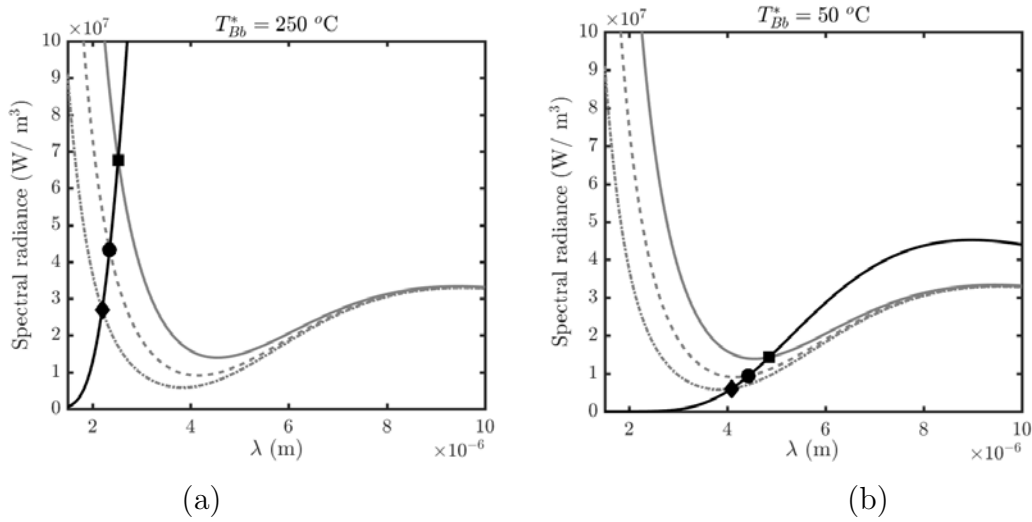


Figure B.2: Spectral radiance versus wavelength for incoming solar radiation at intensities of 500 W/m^2 (dot-dashed grey lines), 1000 W/m^2 (dashed grey lines), 2000 W/m^2 (solid grey lines), and outgoing black-body radiation (solid black lines), (a) $T_{Bb}^* = 250 \text{ }^\circ\text{C}$, and (b) $T_{Bb}^* = 50 \text{ }^\circ\text{C}$.

The results shown in Figure B.2 are generalised in Figure B.3, which offers a more comprehensive illustration of how λ_{crit} varies across incoming radiative intensity for $T_{Bb}^* = 250 \text{ }^\circ\text{C}$ (solid black line), $T_{Bb}^* = 200 \text{ }^\circ\text{C}$ (dot-dashed black line), $T_{Bb}^* = 150 \text{ }^\circ\text{C}$ (dashed black line), $T_{Bb}^* = 100 \text{ }^\circ\text{C}$ (dotted black line), and $T_{Bb}^* = 50 \text{ }^\circ\text{C}$ (solid grey line). We note that λ_{crit} clearly increases both as the temperature decreases and the intensity of incoming radiation increases.

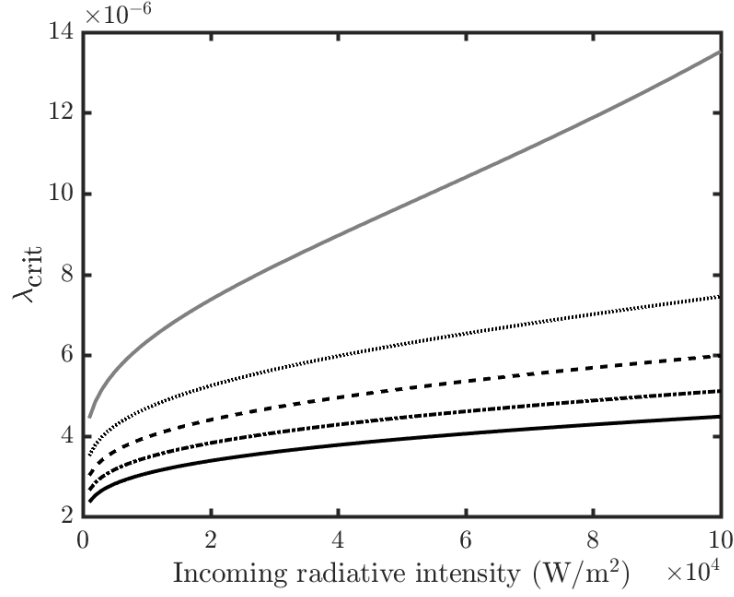


Figure B.3: Critical wavelength for an ideal heat-mirror versus incoming radiative intensity for $T_{Bb}^* = 250$ °C (solid black line), $T_{Bb}^* = 200$ °C (dot-dashed black line), $T_{Bb}^* = 150$ °C (dashed black line), $T_{Bb}^* = 100$ °C (dotted black line), and $T_{Bb}^* = 50$ °C (solid grey line).

The effective solar transparency and effective infra-red emissivity depend on the critical wavelength; it follows that τ_{crit} and ϵ_{crit} also vary across different incoming radiative intensities and different black-body temperatures. Figure B.4 illustrates how τ_{eff} varies across incoming radiative intensity when $T_{Bb}^* = 250$ °C (solid black line), $T_{Bb}^* = 200$ °C (dot-dashed black line), $T_{Bb}^* = 150$ °C (dashed black line), $T_{Bb}^* = 100$ °C (dotted black line), and $T_{Bb}^* = 50$ °C (solid grey line). Initially the effective solar transparency rises rapidly as the incoming radiative intensity increases before plateauing as $\tau_{\text{eff}} \rightarrow 1$. The effective transparency decreases as T_{Bb}^* increases; as the black-body's temperature increases, its spectral radiance is shifted towards shorter wavelengths and overlaps more with the spectral radiance of solar radiation. Thus, as T_{Bb}^* increases, λ_{crit} is shorter and so more of the incoming solar energy is reflected.

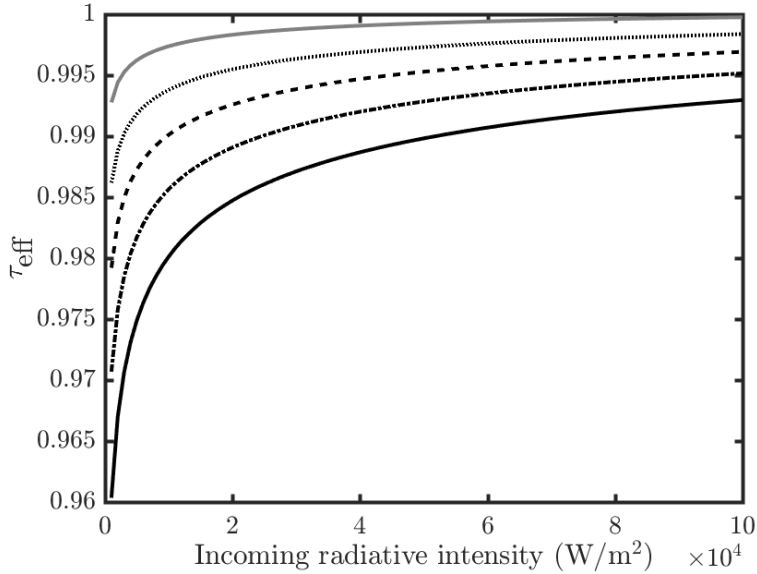


Figure B.4: Effective solar transparency of an ideal heat-mirror versus incoming radiative intensity for $T_{Bb}^* = 250$ °C (solid black line), $T_{Bb}^* = 200$ °C (dot-dashed black line), $T_{Bb}^* = 150$ °C (dashed black line), $T_{Bb}^* = 100$ °C (dotted black line), and $T_{Bb}^* = 50$ °C (solid grey line).

Figure B.5 illustrates how ϵ_{eff} varies across incoming radiative intensity for $T_{Bb}^* = 250$ °C (solid black line), $T_{Bb}^* = 200$ °C (dot-dashed black line), $T_{Bb}^* = 150$ °C (dashed black line), $T_{Bb}^* = 100$ °C (dotted black line), and $T_{Bb}^* = 50$ °C (solid grey line). The effective infra-red emissivity of an ideal heat-mirror is very small across all temperatures and when the intensity of incoming radiation is 1000 W/m^2 , it decreases from $\epsilon_{\text{eff}} = 0.0225$ at $T_{Bb}^* = 50$ °C to $\epsilon_{\text{eff}} = 0.003$ at $T_{Bb}^* = 250$ °C. Interestingly, ϵ_{eff} increases as the intensity of incoming solar radiation increases, however this increase is faster when T_{Bb}^* is lower. At $G_s^* = 100,000 \text{ W/m}^2$, ϵ_{eff} decreases from $0.75 \rightarrow 0.147$ as T_{Bb}^* decreases from $250 \rightarrow 50$ °C. We note that a black-body emits less overall electromagnetic radiation as its temperature decreases; so, although the emissivity of an ideal heat-mirror is larger at lower temperatures, the overall radiation emitted is still lower as T_{Bb}^* decreases.

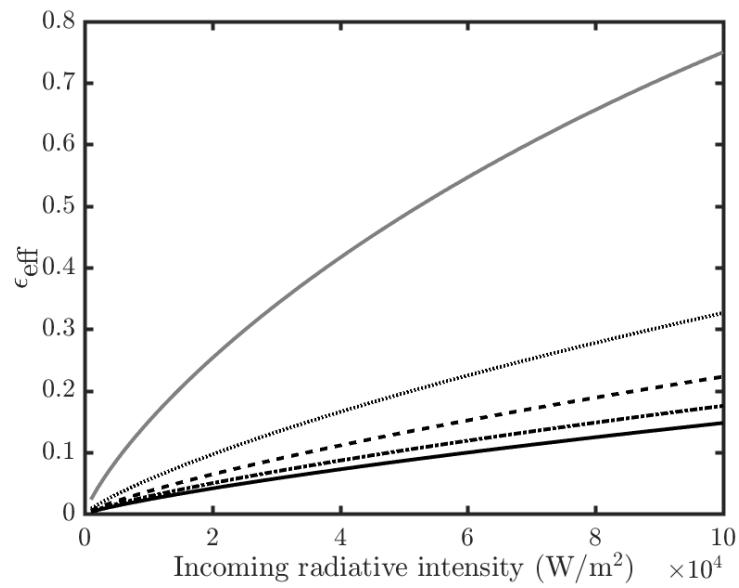


Figure B.5: Effective infra-red emissivity of an ideal heat-mirror versus incoming radiative intensity for $T_{Bb}^* = 250 \text{ }^\circ\text{C}$ (solid black line), $T_{Bb}^* = 200 \text{ }^\circ\text{C}$ (dot-dashed black line), $T_{Bb}^* = 150 \text{ }^\circ\text{C}$ (dashed black line), $T_{Bb}^* = 100 \text{ }^\circ\text{C}$ (dotted black line), and $T_{Bb}^* = 50 \text{ }^\circ\text{C}$ (solid grey line).

APPENDIX C

IMPROVED NUMERICAL SCHEME FOR MODELLING COLLECTOR 4

This section discusses the finite difference scheme used to obtain a numerical expression for the temperature of the nanofluid as it flows through the collector. We discretise the partial differential equation which describes conservation of energy in the system, (5.3.32), to obtain

$$\begin{aligned}
\frac{1}{\Delta x} (r_i^2 - r_i^4) (T_{i,j}^{n+1} - T_{i,j}^n) &= \frac{\gamma}{2\Delta r^2} r_i^2 (T_{i+1,j}^{n+1} - 2T_{i,j}^{n+1} + T_{i-1,j}^{n+1} + T_{i+1,j}^n - 2T_{i,j}^n + T_{i-1,j}^n) \\
&+ \frac{\gamma}{4\Delta r} r_i (T^{n+1} - T_{i-1,j}^{n+1} + T_{i+1,j}^n - T_{i-1,j}^n) \\
&+ \frac{\gamma}{2\Delta\phi^2} (T_{i,j+1}^{n+1} - 2T_{i,j}^{n+1} + T_{i,j-1}^{n+1} + T_{i,j+1}^n - 2T_{i,j}^n \\
&\quad + T_{i,j-1}^n) + r_i^2 q_{i,j},
\end{aligned} \tag{C.0.1}$$

which holds for $i = 1, \dots, I - 1$, $j = 1, \dots, J - 1$, and $n = 1, \dots, N$. The continuous functions $G_{s,1}(\phi)$ and $G_{s,2}(\phi)$ are similarly discretised to obtain

$$G_{s,1,j} = \begin{cases} 0 & \text{if } \phi_j > \phi_{\text{crit}} \\ \frac{1}{\sin \phi_j - 1} & \text{if } \phi_j \leq \phi_{\text{crit}}, \end{cases} \tag{C.0.2}$$

$$G_{s,2,j} = \begin{cases} 0 & \text{if } \phi_j < -\phi_{\text{crit}} \\ \frac{1}{\sin(-\phi_j)-1} & \text{if } \phi_j \geq -\phi_{\text{crit}}, \end{cases} \quad (\text{C.0.3})$$

which appear in the discretised source term

$$q_{i,j} = \frac{1}{r_i} \left(\frac{G_{s,1,j}}{\left(1 + \frac{\beta_0}{2} (1 - r_i)\right)^{\beta_1+1}} + \frac{G_{s,2,j}}{\left(1 + \frac{\beta_0}{2} (1 + r_j)\right)^{\beta_1+1}} \right). \quad (\text{C.0.4})$$

The boundary condition at $i = I$, (5.3.34), is

$$\begin{aligned} \frac{1}{2\Delta x} (T_{I,j}^{n+1} - T_{I-1,j}^{n+1} + T_{I,j}^n - T_{I-1,j}^n) &= -\frac{\text{Nu}}{2} (T_{I,j}^{n+1} + T_{I,j}^n) - \text{Nu}\hat{T} \\ &+ \hat{\gamma} \left(1 - (\lambda + \varphi T_{I,j}^n)^4\right), \end{aligned} \quad (\text{C.0.5})$$

which holds for $j = 1, \dots, J-1$, and $n = 1, \dots, N$. This expression includes a slight modification of the Crank-Nicolson method in order to approximate $(\lambda + \varphi T)^4$ (the nonlinear term from (5.3.34)), with $(\lambda + \varphi T_{I,j}^n)^4$. We note that this nonlinear term can also be approximated using a linearisation, which allows an unmodified Crank-Nicolson method.

Due to the singular nature of (5.3.32) at $r = 0$, we approximate the boundary condition at $i = 0$ with

$$\frac{1}{2} (T_{0,j}^{n+1} + T_{0,j}^n) = \frac{1}{2I} \sum_{i=0}^I (T_{1,j}^{n+1} + T_{1,j}^n). \quad (\text{C.0.6})$$

Also, symmetry of the system at $j = 0$, J is expressed with the boundary conditions

$$\frac{1}{2\Delta\phi} (T_{i,1}^{n+1} - T_{i,0}^{n+1} + T_{i,1}^n - T_{i,0}^n) = 0, \quad (\text{C.0.7})$$

and

$$\frac{1}{2\Delta\phi} (T_{i,J}^{n+1} - T_{i,J-1}^{n+1} + T_{i,J}^n - T_{i,J-1}^n) = 0 \quad (\text{C.0.8})$$

respectively.

The heat source term $q(\phi, r)$ in the governing temperature equation (5.3.43) is highly nonlinear in ϕ and r ; as such, careful consideration must be taken when choosing $\Delta\phi$ and Δr so that this source term is appropriately discretised. One way to accurately discretise $q(\phi, r)$ is to increase I, J , and N , thus, making the

mesh finer. However, as we do this the problem becomes more difficult to solve due to its increasing computational intensity. So, rather than increase the mesh resolution, we alter the Crank-Nicholson method to make it more accurate for coarser meshes. We do this by anticipating, and correcting for, the errors which emerge as a result of discretising the source term. More specifically, we use the Trapezoidal rule to ensure that the overall amount of energy entering the system is accurate. Let $\{x_k\}$ be a partition of $[a, b]$ such that $a = x_0 < x_1 < \dots < x_{N-1} < x_N = b$ and Δx_k be the length of the k -th subinterval, then the Trapezoidal rule states that

$$\int_a^b f(x) dx \approx \sum_{k=1}^N \frac{f(x_{k-1}) + f(x_k)}{2} \Delta x_k. \quad (\text{C.0.9})$$

Therefore, we introduce a new term called the fraction error, F_e , which is defined such that F_e is the exact integral of a function divided by the numerical integral of its discretisation (which is calculated via the Trapezoidal rule), i.e.,

$$F_e = \frac{\int_a^b f(x) dx}{\sum_{k=1}^N \frac{f(x_{k-1}) + f(x_k)}{2} \Delta x_k}, \quad (\text{C.0.10})$$

or equivalently

$$F_e \sum_{k=1}^N \frac{f(x_{k-1}) + f(x_k)}{2} \Delta x_k = \int_a^b f(x) dx. \quad (\text{C.0.11})$$

We recall how $G_{s,1}$ is discretised by (C.0.2); since $G_{s,1}$ is a piecewise function with a discontinuity at ϕ_{crit} , the associated fraction error, $F_{e,1}$, is very sensitive to changes in $\Delta\phi$ (for example, when $\phi_{\text{crit}} = -0.6435$, and $J = 18$, $F_{e,1} = 0.8998$). To overcome this issue, we discretise $G_{s,1}(\phi)$ with

$$G_{s,1,j} = \begin{cases} 0 & \text{if } \phi_j > \phi_{\text{crit}} \\ \frac{F_{e,1}}{\sin \phi_j - 1} & \text{if } \phi_j \leq \phi_{\text{crit}}. \end{cases} \quad (\text{C.0.12})$$

This discretisation ensures that the numerical approximation of $\int_{-\pi/2}^{\pi/2} G_{s,1}(\phi) d\phi$ does not vary much across different values of J . Therefore, (C.0.12) is a better approximation of $G_{s,1}(\phi)$ than (C.0.2) for smaller values of J because it does not overestimate/underestimate the overall amount of solar energy entering the

system. Figure C.1 compares the two different discretisations of $G_{s,1}(\phi)$ when $J = 18$. The standard method gives a more accurate approximation of $G_{s,1}(\phi)$ than the fraction error method; however, the standard method does not provide an accurate approximation of the total amount of energy entering the system due to the discontinuity at $\phi = \phi_{\text{crit}}$. As a result, if one was to evaluate $\int_{-\pi/2}^{\pi/2} G_{s,1}(\phi) d\phi$ using (C.0.2), they would overestimate the overall amount of solar radiation entering the system by 11%. On the other hand, (C.0.12) approximates the integral $\int_{-\pi/2}^{\pi/2} G_{s,1}(\phi) d\phi$ quite well even though, when $\phi < \phi_{\text{crit}}$, $G_{s,1}(\phi)$ is underestimated. We note that in this figure, the exact analytic function for $G_{s,1}(\phi)$ is approximated by a discretisation when $J = 1000$ (as $J \rightarrow \infty$, $F_e \rightarrow 1$).

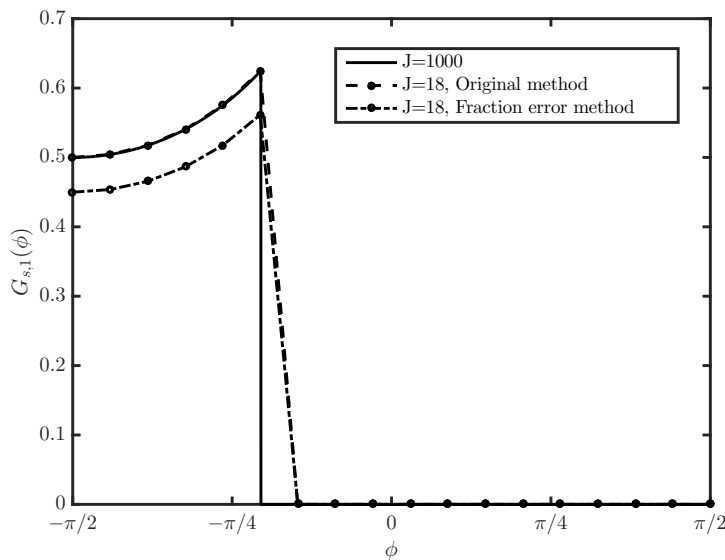
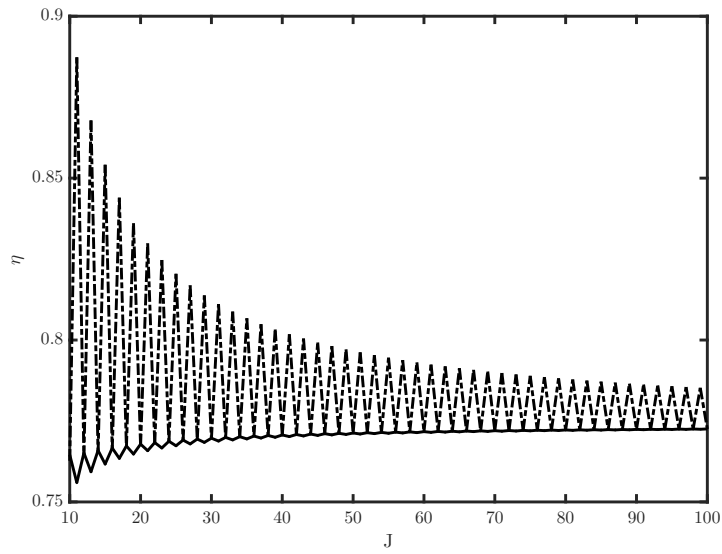


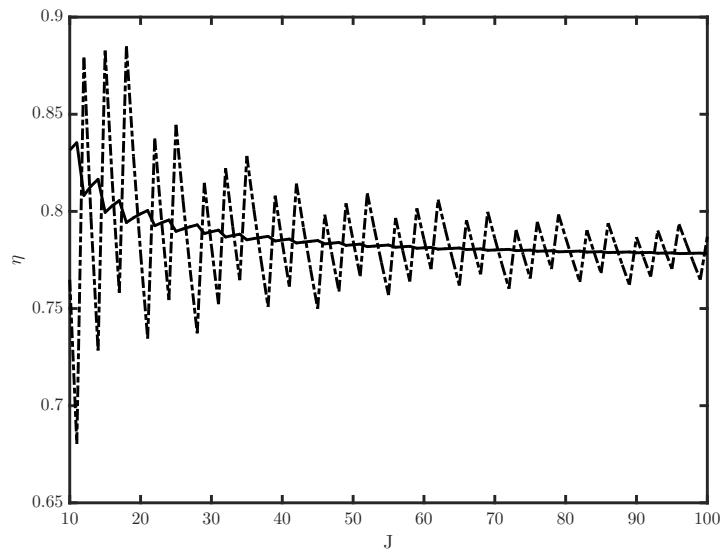
Figure C.1: Discretisation of $G_{s,1}(\phi)$ versus ϕ for $\phi_{\text{crit}} = -0.6435$. $G_{s,1}(\phi)$ is discretised with (C.0.2) and $J = 1000$ (solid line), (C.0.2) and $J = 18$ (dashed line), and (C.0.12) and $J = 18$ (dot-dashed line).

Note that we also use the ‘fraction error method’ to discretise $G_{s,2}(\phi)$. The fraction error method is extremely useful for improving the standard Crank-Nicolson approach as it is applied to this model. Figure C.2 compares the fraction error method to the standard method across two different values for ϕ_{crit} . Figure C.2(ii) has the same ϕ_{crit} as Figure C.1, and in Figure C.2(i) $\phi_{\text{crit}} = 0$. We note that in the standard method, collector efficiency is very sensitive to changes

in J . Although, this sensitivity decreases as J increases and $F_e \rightarrow 1$, the standard method does not converge to a solution before $J = 100$. In contrast, the fraction error method converges to an accurate solution at much lower values of J . Interestingly, the example depicted Figure C.2(i) has a standard solution which is very accurate when J is even and very inaccurate when J is odd. In this example $\phi_{\text{crit}} = 0$ and lies exactly halfway between $-\pi/2$ and $\pi/2$; therefore, when J is even, $\phi_{\text{crit}} = 0$ lies exactly halfway between $\phi_{J/2}$ and $\phi_{J/2+1}$, and so the trapezoidal rule gives a good approximation of $\int_{-\pi/2}^{\pi/2} G_{s,1}(\phi) d\phi$ and $\int_{-\pi/2}^{\pi/2} G_{s,2}(\phi) d\phi$. Meanwhile, when J is odd, $\phi_{\text{crit}} = 0$ lies exactly on $\phi_{(J+1)/2}$, and so the trapezoidal rule gives a rather erroneous approximation of $\int_{-\pi/2}^{\pi/2} G_{s,1}(\phi) d\phi$ and $\int_{-\pi/2}^{\pi/2} G_{s,2}(\phi) d\phi$.



(i)



(ii)

Figure C.2: Efficiency of Solar Collector I versus J for the original Crank-Nicholson method (dot-dashed lines), and the modified Crank-Nicholson method (solid lines); (i) focal length = 0.0375, and (ii) focal length = 0.075.

APPENDIX D

ALTERNATIVE ANALYTIC EXPRESSION FOR TIME-DEPENDENT TEMPERATURE IN SCENARIO 2

In Scenario 2, since the nanofluid flows through the collector at a velocity of 0.237 m s^{-1} , it is only in the receiver for 33.76 seconds, which is a relatively short duration compared to the overall length of a day. The solar intensity given by (7.2.20) changes on a time-scale of hours rather than seconds, i.e., it is approximately constant over any period of 33.76 seconds. Thus, we assume that the system is approximately steady-state, i.e.,

$$\frac{\partial T}{\partial t} \approx 0. \quad (\text{D.0.1})$$

Using this assumption conservation of energy in the system given by (7.2.16) reduces to

$$T_x = G_s(t) + \gamma - \tau^4. \quad (\text{D.0.2})$$

Integrating both sides of (D.0.2) and applying the initial condition, $T(x=0) = 0$, yields

$$T(x, t) = (G_s(t) + \gamma - \tau^4) x. \quad (\text{D.0.3})$$

D. ALTERNATIVE ANALYTIC EXPRESSION FOR TIME-DEPENDENT TEMPERATURE IN SCENARIO 2

The error associated with using this expression of temperature rather than the full expression, (7.2.20), is given by

$$\text{Error (\%)} = 100 \left(\frac{T_1 - T}{T_1} \right), \quad (\text{D.0.4})$$

where T_1 is the temperature given by (7.2.20), and T is the approximation given by (D.0.3). Figure D.1 shows that (D.0.3) works well over the course of a day— $\max(|\text{Error}|) < 0.05\%$.

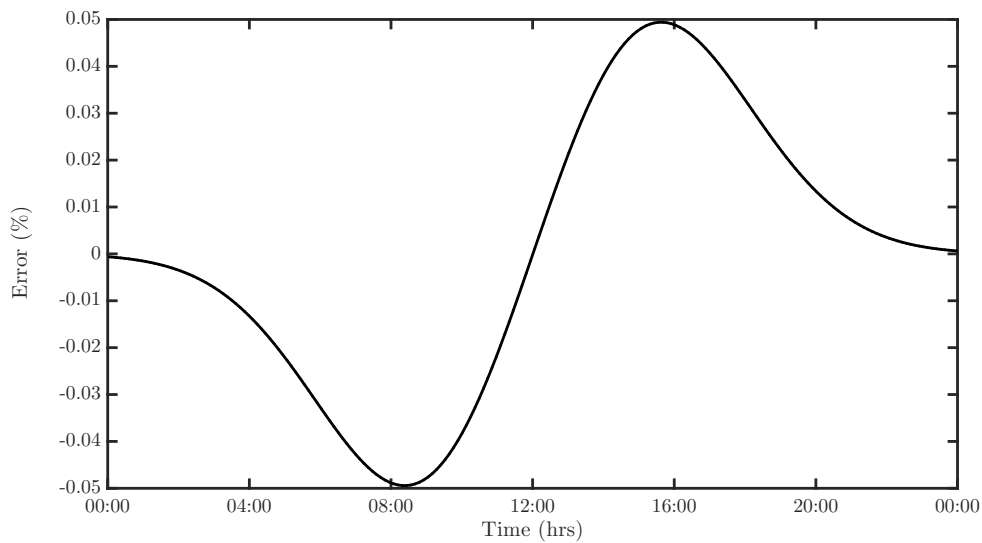


Figure D.1: Error arising from the assumption that the pipe is running at a steady-state where $f_v=0.006$, $R = 0.035\text{m}$, $L = 8\text{m}$, and $C_A = 71.43$.

BIBLIOGRAPHY

- [1] M. Abramowitz and I. A. Stegun. *Handbook of mathematical functions: with formulas, graphs, and mathematical tables*. Number 55. Courier Corporation, 1964. 153
- [2] D. J. Acheson. *Elementary fluid dynamics*. Oxford University Press, 1990. 20
- [3] L. Ayompe, A. Duffy, M. Mc Keever, M. Conlon, and S. McCormack. Comparative field performance study of flat plate and heat pipe evacuated tube collectors (etcs) for domestic water heating systems in a temperate climate. *Energy*, 36(5):3370–3378, 2011. 4, 5
- [4] C. F. Bohren and D. R. Huffman. *Absorption and scattering of light by small particles*. John Wiley & Sons, 2008. 19
- [5] British Petroleum. BP Energy Outlook 2017 edition. *Outlook to 2035*, 2017. 1, 2, 3
- [6] C. Burroughs and L. Hecker. Sandia, stirling energy systems set new world record for solar-to-grid conversion efficiency. *Sandia News Release*, 2008. 9
- [7] E. Cojocar. Parabolic cylinder functions implemented in matlab. *arXiv preprint arXiv:0901.2220*, 2009. 154
- [8] G. Colangelo, E. Favale, A. de Risi, and D. Laforgia. A new solution for reduced sedimentation flat panel solar thermal collector using nanofluids. *Applied Energy*, 111:80–93, 2013. 10

- [9] W. Comerford. Dispelling the solar myth - evacuated tube versus flat plate panels, 2011. 5
- [10] V. Cregan and T. G. Myers. Modelling the efficiency of a nanofluid direct absorption solar collector. *International Journal of Heat and Mass Transfer*, 90:505–514, 2015. 14, 15, 19, 20, 22, 28, 29, 32, 34, 35, 38, 39, 42, 45, 48, 59, 63, 66, 87, 91, 97, 124, 139, 140, 147
- [11] E. Crooks. Coal hits a plateau. *Financial Times*, 2017. [Online: posted 19/09/2017]. 1, 2
- [12] J. A. Duffie and W. A. Beckman. *Solar Engineering of Thermal Processes*. John Wiley & Sons, 2013. 92, 108, 111, 129, 132, 133
- [13] J. Eastman, U. Choi, S. Li, L. Thompson, and S. Lee. Enhanced thermal conductivity through the development of nanofluids. *MRS Online Proceedings Library Archive*, 457, 1996. 10
- [14] T. Elperin, N. Kleorin, and I. Rogachevskii. Turbulent thermal diffusion of small inertial particles. *Physical Review Letters*, 76(2):224, 1996. 103
- [15] Energy Information Administration. How much electricity does an American home use?, 2015. 135
- [16] J. C. C. Fan and F. J. Bachner. Transparent heat mirrors for solar-energy applications. *Applied Optics*, 15(4):1012–1017, 1976. 77, 78, 79, 80, 91, 92, 110, 159
- [17] T. Ganesan, I. Elamvazuthi, K. Z. K. Shaari, and P. Vasant. Hypervolume-driven analytical programming for solar-powered irrigation system optimization. In *Nostradamus 2013: Prediction, Modeling and Analysis of Complex Systems*, pages 147–154. Springer, 2013. 149
- [18] F. Giovannetti, S. Föste, N. Ehrmann, and G. Rockendorf. High transmittance, low emissivity glass covers for flat plate collectors: applications and performance. *Solar Energy*, 104:52–59, 2014. 91, 92
- [19] T. B. Gorji and A. Ranjbar. A review on optical properties and application of nanofluids in direct absorption solar collectors (dascs). *Renewable and Sustainable Energy Reviews*, 72:10–32, 2017. 14, 104, 105

- [20] U. Herrmann, B. Kelly, and H. Price. Two-tank molten salt storage for parabolic trough solar power plants. *Energy*, 29(5):883–893, 2004. 6
- [21] C. K. Ho and B. D. Iverson. Review of high-temperature central receiver designs for concentrating solar power. *Renewable and Sustainable Energy Reviews*, 29:835–846, 2014. 8
- [22] F. P. Incropera, D. P. DeWitt, and A. S. L. Theodore L. Bergman. *Introduction to Heat Transfer*. John Wiley & Sons, fifth edition, 2007. 35
- [23] M. Janecek. Reflectivity spectra for commonly used reflectors. *IEEE Transactions on Nuclear Science*, 59(3):490–497, 2012. 46, 48
- [24] S. M. Jeter. Calculation of the concentrated flux density distribution in parabolic trough collectors by a semifinite formulation. *Solar Energy*, 37(5):335–345, 1986. 85
- [25] S. Kalogirou. The potential of solar industrial process heat applications. *Applied Energy*, 76(4):337–361, 2003. 5, 7
- [26] S. A. Kalogirou. Solar thermal collectors and applications. *Progress in Energy and Combustion Science*, 30(3):231–295, 2004. 4
- [27] C. Kerschner and I. Capellán-Pérez. Peak-oil and ecological economics. *Handbook of Ecological Economics*, 2017. 2
- [28] V. Khullar, H. Tyagi, N. Hordy, T. P. Otanicar, Y. Hewakuruppu, P. Modi, and R. A. Taylor. Harvesting solar thermal energy through nanofluid-based volumetric absorption systems. *International Journal of Heat and Mass Transfer*, 77:377–384, 2014. 77, 100, 105, 119, 138, 143, 145, 146
- [29] V. Khullar, H. Tyagi, P. E. Phelan, T. P. Otanicar, H. Singh, and R. A. Taylor. Solar energy harvesting using nanofluids-based concentrating solar collector. *Journal of Nanotechnology in Engineering and Medicine*, 3(3):031003, 2012. 86, 91, 92, 97, 104, 106, 109, 110, 112, 118, 144
- [30] H. H. Kimball. Intensity of solar radiation at the surface of the earth, and its variations with latitude, altitude, season, and time of day. *Monthly Weather Review*, 63(1):1–4, 1935. 121

- [31] G. J. Kolb. An evaluation of possible next-generation high-temperature molten-salt power towers. *Sandia National Laboratories, Albuquerque, NM, Report No. SAND2011-9320*, 2011. 122, 149
- [32] S. Kuravi, J. Trahan, D. Y. Goswami, M. M. Rahman, and E. K. Stefanakos. Thermal energy storage technologies and systems for concentrating solar power plants. *Progress in Energy and Combustion Science*, 39(4):285–319, 2013. 6
- [33] S. Ladjevardi, A. Asnaghi, P. Izadkhast, and A. Kashani. Applicability of graphite nanofluids in direct solar energy absorption. *Solar Energy*, 94:327 – 334, 2013. 19
- [34] C. Lamnatou, C. Cristofari, D. Chemisana, and J. Canaletti. Building-integrated solar thermal systems based on vacuum-tube technology: Critical factors focusing on life-cycle environmental profile. *Renewable and Sustainable Energy Reviews*, 65:1199–1215, 2016. 4
- [35] B. J. Lee, K. Park, T. Walsh, and L. Xu. Radiative heat transfer analysis in plasmonic nanofluids for direct solar thermal absorption. *Journal of solar Energy Engineering*, 134(2):021009, 2012. 20
- [36] S. H. Lee and S. P. Jang. Efficiency of a volumetric receiver using aqueous suspensions of multi-walled carbon nanotubes for absorbing solar thermal energy. *International Journal of Heat and Mass Transfer*, 80:58 – 71, 2015. 14, 15, 28, 33, 34, 35, 38, 59, 139, 147, 154
- [37] A. Lenert and E. N. Wang. Optimization of nanofluid volumetric receivers for solar thermal energy conversion. *Solar Energy*, 86(1):253–265, 2012. 11, 16
- [38] Q. Li, C. Zheng, S. Mesgari, Y. L. Hewkuruppu, N. Hjerrild, F. Crisostomo, G. Rosengarten, J. A. Scott, and R. A. Taylor. Experimental and numerical investigation of volumetric versus surface solar absorbers for a concentrated solar thermal collector. *Solar Energy*, 136:349–364, 2016. 3, 9, 13, 14, 75, 77, 78, 79, 81, 91, 100, 105, 110, 118, 119, 138, 143, 145, 146

- [39] F. Mahjouri. Vacuum tube liquid-vapor (heat-pipe) collectors. In *Proceedings of the solar conference*, pages 341–346. American Solar Energy Society; American Institute of Architects, 2004. 5
- [40] C. L. Martin and D. Y. Goswami. *Solar energy pocket reference*. Earthscan/James & James, 2005. 8
- [41] A. Menbari and A. A. Alemrajabi. Analytical modeling and experimental investigation on optical properties of new class of nanofluids (al₂o₃-cuo binary nanofluids) for direct absorption solar thermal energy. *Optical Materials*, 52:116–125, 2016. 20
- [42] A. Menbari, A. A. Alemrajabi, and A. Rezaei. Heat transfer analysis and the effect of cuo/water nanofluid on direct absorption concentrating solar collector. *Applied Thermal Engineering*, 104:176–183, 2016. 96, 97, 100, 104, 106, 111, 112, 118, 119, 138, 143, 145, 146
- [43] T. G. Myers, M. M. MacDevette, and H. Ribera. A time-dependent model to determine the thermal conductivity of a nanofluid. *Journal of Nanoparticle Research*, 15(7):1–11, 2013. 18
- [44] National Renewable Energy Laboratory. Solar energy basics. 4
- [45] A. Omri. Co₂ emissions, energy consumption and economic growth nexus in mena countries: evidence from simultaneous equations models. *Energy Economics*, 40:657–664, 2013. 1
- [46] T. Otanicar, J. Hoyt, M. Fahar, X. Jiang, and R. A. Taylor. Experimental and numerical study on the optical properties and agglomeration of nanoparticle suspensions. *Journal of Nanoparticle Research*, 15(11):2039, 2013. 20
- [47] T. P. Otanicar, P. E. Phelan, and J. S. Golden. Optical properties of liquids for direct absorption solar thermal energy systems. *Solar Energy*, 83(7):969–977, 2009. 10, 29, 66, 109
- [48] T. P. Otanicar, P. E. Phelan, R. S. Prasher, G. Rosengarten, and R. A. Taylor. Nanofluid-based direct absorption solar collector. *Journal of Renewable and Sustainable Energy*, 2(3):033102, 2010. 11, 32, 42, 44, 48, 50, 53, 59, 66

- [49] S. Parvin, R. Nasrin, and M. A. Alim. Forced convection through nanofluid-based direct absorption solar collector. *Proceedings of the 15th Annual Paper Meet*, 7:08, 2014. 10
- [50] M. M. Probst and C. Roecker. Towards an improved architectural quality of building integrated solar thermal systems (bist). *Solar Energy*, 81(9):1104–1116, 2007. 14
- [51] A. D. Rakić. Algorithm for the determination of intrinsic optical constants of metal films: application to aluminum. *Applied Optics*, 34(22):4755–4767, 1995. 29, 66, 109
- [52] REN21. Renewables 2016 global status report. Technical report, Paris: REN21 Secretariat, 2016. ISBN: 978-3-9818107-0-7. 3
- [53] R. Saidur, T. Meng, Z. Said, M. Hasanuzzaman, and A. Kamyar. Evaluation of the effect of nanofluid-based absorbers on direct solar collector. *International Journal of Heat and Mass Transfer*, 55(21):5899–5907, 2012. 20
- [54] Solutia. Therminol vp-1. <http://twt.mpei.ac.ru/tthb/hedh/htf-vp1.pdf>. Accessed: 28/02/2017. 109
- [55] R. Tamme, T. Bauer, J. Buschle, D. Laing, H. Müller-Steinhagen, and W.-D. Steinmann. Latent heat storage above 120 c for applications in the industrial process heat sector and solar power generation. *International Journal of Energy Research*, 32(3):264–271, 2008. 5, 6
- [56] R. Tamme, D. Laing, and W.-D. Steinmann. Advanced thermal energy storage technology for parabolic trough. In *ASME 2003 International Solar Energy Conference*, pages 563–571. American Society of Mechanical Engineers, 2003. 6
- [57] R. A. Taylor, Y. Hewakuruppu, D. DeJarnette, and T. P. Otanicar. Fabrication and comparison of selective, transparent optics for concentrating solar systems. In *SPIE Optics & Photonics for Sustainable Energy*, pages 955905–955905. International Society for Optics and Photonics, 2015. 79, 80

- [58] R. A. Taylor, Y. Hewakuruppu, D. DeJarnette, and T. P. Otanicar. Comparison of selective transmitters for solar thermal applications. *Applied Optics*, 55(14):3829–3839, 2016. 77, 79
- [59] R. A. Taylor, P. E. Phelan, T. P. Otanicar, R. Adrian, and R. Prasher. Nanofluid optical property characterization: towards efficient direct absorption solar collectors. *Nanoscale Research Letters*, 6(1):1–11, 2011. 4, 10, 19, 20, 24, 25, 77, 105, 109, 119, 145
- [60] C. L. Tien. Thermal radiation in packed and fluidized beds. *Journal of Heat Transfer*, 110(4b):1230–1242, 1988. 19
- [61] G. R. Timilsina, L. Kurdgelashvili, and P. A. Narbel. Solar energy: Markets, economics and policies. *Renewable and Sustainable Energy Reviews*, 16(1):449–465, 2012. 3
- [62] M. Turkyilmazoglu. Performance of direct absorption solar collector with nanofluid mixture. *Energy Conversion and Management*, 114:1–10, 2016. 15, 28, 33, 38, 59, 139
- [63] H. Tyagi, P. Phelan, and R. Prasher. Predicted efficiency of a low-temperature nanofluid-based direct absorption solar collector. *Journal of Solar Energy Engineering*, 131(4):041004, 2009. 14, 20, 28, 29, 32, 34, 35, 36, 38, 39, 59, 66, 97, 139
- [64] University of Oregon Solar Radiation Monitoring Laboratory. Archival solar data from Seattle, Wahington, June, 2015. 126
- [65] U.S. Energy Information Administration. *International Energy Outlook 2017*. 2017. 1, 2, 3
- [66] A. Veeraragavan, A. Lenert, B. Yilbas, S. Al-Dini, and E. N. Wang. Analytical model for the design of volumetric solar flow receivers. *International Journal of Heat and Mass Transfer*, 55(4):556–564, 2012. 14, 21, 86, 97, 104, 111, 149
- [67] X. D. Wang, L. Zhao, J. L. Wang, W. Z. Zhang, X. Z. Zhao, and W. Wu. Performance evaluation of a low-temperature solar rankine cycle system utilizing R245fa. *Solar Energy*, 84(3):353–364, 2010. 6

BIBLIOGRAPHY

- [68] E. Whittaker. On the functions associated with the parabolic cylinder in harmonic analysis. *Proceedings of the London Mathematical Society*, 1(1):417–427, 1902. 31
- [69] W. Yu and S. Choi. The role of interfacial layers in the enhanced thermal conductivity of nanofluids: a renovated Maxwell model. *Journal of Nanoparticle Research*, 5(1-2):167–171, 2003. 18